

# High-Resolution Velocimetry of a Dual-Mode Scramjet Flameholder

---

A Dissertation

Presented to

the Faculty of the School of Engineering and Applied Science

University of Virginia

---

In Partial Fulfillment

of the requirements for the Degree

Doctor of Philosophy (Mechanical and Aerospace Engineering)

by

Damien A. Lieber

December 2018



# Approval Sheet

This dissertation is submitted in partial fulfillment of the requirements for the degree of  
Doctor of Philosophy (Mechanical and Aerospace Engineering)

Damien A. Lieber

---

Damien A. Lieber

This dissertation has been read and approved by the Examining Committee:

Christopher Goyne

---

Christopher Goyne, Adviser

Harsha Chelliah

---

Harsha Chelliah, Committee Chair

Scott Acton

---

Scott Acton

Daniel Quinn

---

Daniel Quinn

Andrew Cutler

---

Andrew Cutler

Accepted for the School of Engineering and Applied Science:

Craig H. Benson

---

Craig H. Benson, Dean, School of Engineering and Applied Science

December 2018

*To everyone who believed in me and supported me in my success.*



# Acknowledgments

**Professor Christopher Goyne**

Thank you for your continued advice and support throughout the PhD program.

**Professor Harsha Chelliah, Andrew Cutler, Daniel Quinn, Scott Acton**

Thank you your advice and time serving on my PhD Advisory Committee.

**Dr. Bob Rockwell**

Thanks for always being available to operate the wind tunnel, help, and give me advice.

**Clayton Geipel, Walker Smith, Dr. Vladimir Mitkin, Dr. David Barnes, Dr. Brian Rice, Dr. Justin Kirik, Nathaniel Gibbons**

Thank you or your help in setting up experiments, running the tunnel, brainstorm ideas, and making the lab a friendly environment.

**The MAE department, the AFOSR, and the NSF**

Thank you for sponsoring my research and PhD education.

**Conner Lohens, Matthew Garrett, and Edwin Spenceley**

Thanks for helping me in the mechanical design of parts and custom-machining them, often on a tight schedule.

**Danielle and Marc Lieber, Armand and Jeanne Heitz, Julia Schrank, Jean-Marie Muller, Bernadette Etterlen**

Thanks for your support and encouragement throughout my education and for giving me the environment and opportunity to pursue an advanced degree.

**Professor Stuart Laurence at UMD, Professor Klaus Hannemann and the team at DLR Gottingen, Dr. Christopher Strand from Stanford University, Professor Friedrich Seiler from the KIT, and the CLES-FACIL rocketry club at the University of Lyon**

Thanks for believing in me early on and leading me on this path to a PhD in hypersonics.

*And thanks to everyone else who in some form or another helped me on this journey.*

# Contents

<b>Acknowledgments</b>	<b>iii</b>
<b>Contents</b>	<b>v</b>
List of Tables . . . . .	viii
List of Figures . . . . .	ix
<b>Symbols and Abbreviations</b>	<b>xiii</b>
<b>Abstract</b>	<b>1</b>
<b>Introduction</b>	<b>5</b>
<b>1 Design and Testing of an Additively Manufactured Flameholder for Scramjet Flows</b>	<b>9</b>
1.1 Introduction . . . . .	10
1.2 Design Requirements and Methodology . . . . .	14
1.2.1 Design Requirements . . . . .	14
1.2.2 Additive Manufacturing . . . . .	18
1.2.3 Transformation into a semi-free jet configuration flow path . . . . .	20
1.2.4 Modularity . . . . .	23
1.3 Design Iterations and Results . . . . .	25
1.3.1 First two prints . . . . .	25
1.3.2 Third print: modular insert assembly . . . . .	26
1.4 Discussion and Recommendations for Designs of Additive Manufactured Parts . . . . .	31
1.5 Conclusion . . . . .	34
<b>2 High-Resolution PIV Capability for High-Speed High-Enthalpy Flows</b>	<b>37</b>
2.1 Introduction . . . . .	38
2.1.1 Motivation and research question . . . . .	38
2.1.2 Flow velocimetry in high-speed flows . . . . .	39
2.1.3 Objectives and Contributions . . . . .	42
2.2 Experimental setup . . . . .	46
2.2.1 Summary and hardware specifications . . . . .	46
2.2.2 Tracer properties and seeding . . . . .	47
2.2.3 Laser timing and sheet characteristics . . . . .	48
2.2.4 Imaging setup optimization . . . . .	49
2.3 Signal enhancement . . . . .	55
2.3.1 Raw signal quality assessment . . . . .	55

2.3.2	Diagnosis with synthetic PIV . . . . .	57
2.3.3	Logarithmic Contrast Stretch filter design . . . . .	60
2.3.4	Cross-correlation and vectors post-processing . . . . .	62
2.4	Signal Uncertainties . . . . .	64
2.4.1	Sources of Uncertainties and Signal Noise . . . . .	64
2.4.2	RMS correction and uncertainties propagation . . . . .	67
2.5	Discussion and recommendations for high-resolution velocimetry in high-speed com- busting flows . . . . .	68
2.5.1	LCS results on synthetic PIV . . . . .	68
2.5.2	LCS results on real PIV measurements . . . . .	69
2.6	Conclusion . . . . .	72
<b>3</b>	<b>High-Resolution PIV for Characterization of the Inflow to a Cavity for High- Speed Flameholding</b>	<b>73</b>
3.1	Introduction . . . . .	74
3.2	Method and Setup . . . . .	76
3.3	PIV at the model leading edge . . . . .	77
3.3.1	Means . . . . .	77
3.3.2	Root-Mean-Square velocities . . . . .	78
3.3.3	Turbulent Kinetic Energy and Intensity . . . . .	79
3.4	PIV at the cavity inflow . . . . .	82
3.4.1	Mean velocities . . . . .	82
3.4.2	RMS velocities . . . . .	83
3.4.3	Turbulent Kinetic Energy and Intensity . . . . .	85
3.5	Comparison between flow conditions . . . . .	86
3.5.1	Variation in global fuel equivalence ratio $\Phi_g$ . . . . .	86
3.5.2	Variation in the shock train location . . . . .	87
3.5.3	With and without heat release . . . . .	90
3.5.4	Integral Length Scales . . . . .	91
3.6	Particle Flow Tracking Assumption . . . . .	92
3.6.1	Background on the graphite nanoflakes selection and flow tracking theory . . . . .	92
3.6.2	Comparison experiment between tracers . . . . .	94
3.6.3	Conclusion . . . . .	96
3.7	Conclusion . . . . .	98
<b>4</b>	<b>Combined PIV-PLIF of High-Speed Cavity-Stabilized Combustion</b>	<b>99</b>
4.1	Introduction . . . . .	100
4.2	Method and Setup . . . . .	105
4.2.1	Flow configuration and experimental setup . . . . .	105
4.2.2	Data processing . . . . .	107
4.3	Statistical results . . . . .	110
4.3.1	Mean velocities . . . . .	110
4.3.2	Fluctuations . . . . .	111
4.3.3	Conditional velocities . . . . .	114
4.4	Combustion dynamics . . . . .	118
4.5	Conclusion . . . . .	123
	<b>Conclusion</b>	<b>125</b>

Contents

vii

**Bibliography**

**131**

# List of Tables

1.1	Design iterations of the flameholder insert. . . . .	25
1.2	Test matrix. . . . .	29
1.3	Flow parameters computed by Robert Rockwell for the in-situ tests described in section 1.3.2. Plenum refers to conditions prior to the tunnel converging-diverging nozzle. Uncertainty includes instrumentation uncertainty and temporal variability of the facility and fuel system. . . . .	30
2.1	Key past 2D-2C PIV work in high-speed flows . . . . .	44
2.2	Key flow characteristics for the present measurements representing operation at the maximum fuel equivalence ratio $\Phi_g = 0.47 \pm 0.03$ . . . . .	45
2.3	Inputs for the theoretical model described in section 2.2.4 to identify enhanced setups. . . . .	51
2.4	Relevant setup characteristics for the present high-resolution PIV experiments. . . . .	54
3.1	Integral length scales measured from PIV data . . . . .	91

# List of Figures

1.1	Schematic of the facility flow path with small-scale cavity flameholder identifying important flow features. . . . .	15
1.2	Flameholder insert geometry with key dimensions. Cooling passages are in yellow, orange, red, magenta, and cyan; fuel lines in green; thermocouples in red; and pressure taps in dark grey. . . . .	15
1.3	Side view of the flow path showing the immersed flameholder. The previous configuration outline with the larger cavity is shown in dashed grey. CARS measurement planes are indicated in green. . . . .	16
1.4	Centerplane section with pressure taps in grey, thermocouples in red, and fuel line in green. The part is oriented at $45^\circ$ as during manufacturing. . . . .	17
1.5	Isometric view highlighting the cooling channels arrangement in yellow, orange, red, and purple. . . . .	21
1.6	FEA calculation of the Inconel 718 cavity flameholder by Robert Rockwell(Lieber et al., 2018a) . . . . .	22
1.7	Modular design and assembly into the UVaSCF flow path. . . . .	23
1.8	Visible light images acquired during test runs. . . . .	26
1.9	Modular design and assembly into the UVaSCF flow path. . . . .	27
1.10	CH chemiluminescence of a premixed ethylene-air flame stabilized over the scaled-down cavity of iteration 3 of table 1.1 with inflow conditions at $\mathbf{M} = 0.6$ , $\mathbf{T}_0 = 1200$ K, $\mathbf{p}_0 = 300$ kPa and an equivalence ratio $\Phi_g = 0.43$ . . . . .	29
1.11	Pressure traces with the flameholder insert. The X-axis is normalized by the cavity height ( $\mathbf{H} = 3$ mm). $\mathbf{p}_{ref}$ is the corresponding pressure immediately past the converging-diverging nozzle for each trace. $\mathbf{X}/\mathbf{H} = 1$ data taken below the insert. . . . .	29
2.1	Schematic of the facility flow path with the small-scale cavity flameholder identifying important flow features. . . . .	38
2.2	Fields of views of the present work up to scale relative to the model insert. . . . .	46
2.3	Laser sheets cross-sectional intensity profiles. . . . .	49
2.4	Solution space for PIV setups in the UVaSCF flow. The chosen solution is the highlighted vortex. . . . .	53
2.5	Signal of a common PIV pair of frames acquired in the flow of table 2.2 and in region L of figure 3.1. The correct displacement is $\Delta X = 13.5$ px and $\Delta Y = 1.5$ px. . . . .	55
2.6	Raw PIV frames. . . . .	56
2.7	Synthetic 14-bits PIV image pairs for the three simulation cases described in section 2.3.2. . . . .	58
2.8	Cross-correlation maps for one identical set of particles with three different combinations of signal disturbances. . . . .	59

2.9	Logarithm-contrast-stretch (LCS) filter transform. (*) Markers denote the intensities used in the example above. . . . .	62
2.10	Setup design and processing steps for high-resolution PIV in a high-speed flow. . . .	68
2.11	Performance comparison of pre-processing filters with a gradient $\frac{do}{di} \propto \frac{1}{i^\alpha}$ for conditions identical to figure 2.8c, where $o$ is the output pixel intensity, $i$ the input pixel intensity, and $\alpha$ a constant. . . . .	69
2.12	Cross-correlation map of the signal of a common PIV pair of frames (see figure 2.5) acquired from experiments in the flow of table 2.2 and in region L of figure 3.1. . . .	70
2.13	Velocimetry highlights for a flow Mach number of $M \sim 0.6$ and a global ethylene equivalence ratio of $\Phi_g \sim 0.48$ acquired immediately upstream of the model leading edge. . . . .	71
3.1	Insert close-up displaying the coordinate system and fields of views L and A. . . . .	76
3.2	Mean velocimetry for a flow Mach number of $M = 0.66$ and a global ethylene equivalence ratio of $\Phi_g = 0.47$ acquired upstream of the flameholder insert. . . . .	78
3.3	Corrected root-mean-square velocimetry for a flow Mach number of $M = 0.66$ and a global ethylene equivalence ratio of $\Phi_g = 0.47$ acquired upstream of the flameholder insert. . . . .	80
3.4	Turbulent Kinetic Energy (TKE) and Intensity (TI) for a flow Mach number of $M = 0.66$ and a global ethylene equivalence ratio of $\Phi_g = 0.47$ acquired upstream of the flameholder insert. . . . .	81
3.5	Mean velocity components for a flow Mach number of $M = 0.66$ and a global ethylene equivalence ratio of $\Phi_g = 0.47$ acquired upstream of the cavity. . . . .	83
3.6	Corrected RMS velocity components for a flow Mach number of $M = 0.66$ and a global ethylene equivalence ratio of $\Phi_g = 0.47$ acquired upstream of the cavity. . . .	84
3.7	TKE and TI for a flow Mach number of $M = 0.66$ and a global ethylene equivalence ratio of $\Phi_g = 0.47$ acquired upstream of the cavity at $X/H=-1.6$ . . . . .	85
3.8	F-test results on case 1 versus case 3. Increase in mean velocities are $o(1)$ m/s. . . .	87
3.9	F-test results. Increase in AVG $o(1)$ m/s. . . . .	89
3.10	F-test results on case 1 versus case 3. . . . .	89
3.11	Schematic of the flow path and PIV field of view up to scale relative to the tunnel. . .	95
3.12	Comparison of the average velocities between the graphite nanoflakes and the silicon dioxide nanospheres. $H$ is a reference dimension corresponding to the cavity height of 3 mm. . . . .	95
3.13	Comparison of RMS velocities between the graphite nanoflakes and the silicon dioxide nanospheres. . . . .	97
4.1	Field of view of the present work up to scale relative to the model insert. . . . .	105
4.2	Principle of the combined PIV-PLIF technique as described in section 4.2. AVG: average; RMS: Root-Mean-Square; TI: Turbulence Intensity; TKE: Turbulent Kinetic Energy. . . . .	106
4.3	Laser sheets cross-sectional intensity profiles. . . . .	106
4.4	Mean velocities and flame intermittency for a flow Mach number of $M = 0.66$ and a global ethylene equivalence ratio of $\Phi_g = 0.47$ . . . . .	112
4.5	RMS velocity components for a flow Mach number of $M = 0.66$ and a global ethylene equivalence ratio of $\Phi_g = 0.47$ . . . . .	113
4.6	Fluctuation energy indicators for a flow Mach number of $M = 0.66$ and a global ethylene equivalence ratio of $\Phi_g = 0.47$ . . . . .	114

4.7	Mean conditional velocity fields. . . . .	116
4.8	Mean transverse velocities through select boundaries (cavity interface or flamefront), indicative of mass flux. . . . .	117
4.9	Select instantaneous PIV-PLIF frames. . . . .	119
4.10	Diagram of the hypothetical combustion cycle. Time indices correspond to those of figures 4.9a-4.9e. . . . .	120
4.11	Select instantaneous swirling strength. . . . .	121



# Symbols and Abbreviations

## Latin symbols

SIGN	UNIT	DESCRIPTION
$d$	[mm]	Diameter
$d^*$	[px]	Diameter
$e$	[–]	Exponential constant
$f$	[mm]	Focal length
$H$	[mm]	Cavity height used in dimensionless coordinates. $H = 3$ mm
$i$	[pxcount]	Input pixel intensity
$k$	[mm <sup>-1</sup> ]	Wave number
$L_{Pixel}$	[m]	Pixel length
$L_{Streak}$	[m]	Image streak length
$m$	[kg]	Mass
$M$	[–]	Mach number
$N$	[–]	f-number
$o$	[pxcount]	Output pixel intensity
$p$	[Pa]	Pressure
$R$	[–]	Reproduction ratio
$t$	[s]	Time
$T$	[K]	Temperature

$u$	[m.s <sup>-1</sup> ]	Velocity component
$U$	[m.s <sup>-1</sup> ]	Velocity magnitude
$X$	[mm]	Streamwise coordinate
$Y$	[mm]	Coordinate normal to the cavity base
$W$	[mm]	Spanwise cavity dimension $W = 38$ mm.
$Z$	[mm]	Spanwise coordinate

### Greek symbols

SIGN	UNIT	DESCRIPTION
$\alpha$	[–]	Constant
$\beta$	[–]	Coordinate index
$\delta t$	[s]	Laser pulse duration
$\Delta t$	[s]	Laser inter-pulse time delay
$\Delta z$	[m]	Measurement volume depth
$\eta$	[m]	Length scale
$\lambda_{Laser}$	[m]	Laser light wavelength
$\mu$	[Pa · s]/[–]	Dynamic viscosity/Mean
$\phi$	[–]	Dimensionless similarity parameter
$\rho$	[kg.m <sup>-3</sup> ]	Mass density
$\sigma$		Standard deviation
$\tau$	[s]	Time scale
$\nu$	[Hz]	Frequency

### Subscripts

SUBSCRIPT	DESCRIPTION
-----------	-------------

---

0	Stagnation conditions
<i>AVG</i>	Average
<i>C</i>	Camera
<i>I</i>	Integral
<i>p</i>	particle
<i>ref</i>	Reference
<i>RMS</i>	Root Mean Square

## Abbreviations

ABBREVIATION	DESCRIPTION
AM	Additive Manufacturing
A.U.	Arbitrary Units
AVG	Average
B-L	Boundary-Layer
CAD	Computer Assisted Design
CARS	Coherent Anti-Stokes Raman Spectroscopy
CFD	Computational Fluid Dynamics
CI	Confidence Interval
CLE	Cavity Leading edge
DOMV	Depth Of Measurement Volume
DSR	Dynamic Spatial Range
DVR	Dynamic Velocity Range
FEA	Finite-Elements Analysis
FOV	Field Of View
FWHM	Full Width Half Maximum
ILE	Insert Leading edge
IW	Interrogation Window
K	Kolmogorov
LDA	Laser Doppler Anemometry
LSV	Laser Speckle Velocimetry
MTV	Molecular Tagging Velocimetry
PIV	Particle Image Velocimetry
PLIF	Planar Laser-Induced Fluorescence
PIV-PLIF	Combined PIV and OH-PLIF
PTV	Particle Tracking Velocimetry
RMS	Root Mean Square

TI	Turbulence Intensity
TKE	Turbulent Kinetic Energy
US	Upstream Surface
UV	Ultraviolet spectral domain
UVaSCF	University of Virginia Supersonic Combustion Facility



# Abstract

Cavity flameholders are a critical technology for hydrocarbon-fueled scramjets, lean premixed combustion in jet engines, and fundamental high-speed combustion studies. This dissertation aims to improve understanding of cavity flameholders by designing a small, immersed cavity flameholder for Direct Numerical Simulations (DNS), characterizing its inflow, and characterizing the turbulence-chemistry interactions at the cavity. This undertaking is part of a multi-disciplinary study on the effects of flow compressibility and heat release on turbulent flame structures and stabilization mechanisms. The collaborative effort notably includes DNS as well as fine-scale flame structure measurements with Hydroxyl (OH) Planar Laser-Induced Fluorescence (PLIF), and Coherent Anti-Stokes Raman Spectroscopy (CARS).

First, a small-scale cavity flameholder for high-speed, premixed ethylene combustion is designed, additively manufactured, and tested at a Mach 5 enthalpy. The cavity is sized to generate a reasonable computational domain while maintaining adequate residence time for flameholding. The flameholder is raised away from the facility wall to minimize boundary layer growth upstream of the cavity. Challenges related to transforming a direct-connect combustor flow path into a semi-free jet flow path for immersed models were encountered: primarily flow blockage and heat removal. The final design is demonstrated to sustain the ethylene flame for repeated cycles lasting up to an hour and can potentially sustain it indefinitely. The flameholder was additively manufactured out of Inconel 718 with internal cooling passages incorporated throughout and strategically designed to minimize residual stresses. This work presents the first published methodology for additively manufactured scramjet combustor components and the first conversion of a direct-connect, high-speed combustion wind tunnel to a semi-free jet configuration.

A critical element necessary for understanding the combustion physics of high-speed compressible

flames is accurate and precise velocimetry. A methodology to successfully implement high-resolution two-components two-dimensional Particle Image Velocimetry (PIV) in the particularly challenging environment of a high-speed, high-enthalpy flow with free stream seeding is presented and demonstrated. The objective is to resolve the finer scales for accurate boundary-conditions in direct numerical simulations. A three-pronged approach consists of predicting the particle image size for a range of setups, enhancing the noisy raw signal with the innovative use of a logarithmic transform, and quantifying uncertainties. The methodology effectiveness is demonstrated with synthetic PIV and experiments conducted in a dual-mode scramjet combustor for which a velocimetry resolution of  $355 \mu\text{m}$  is achieved.

The high-speed inflow to the immersed model and a scaled-down cavity flameholder is subsequently characterized with high-resolution PIV. The effects of varying the shock train location and heat release are analyzed. While varying heat release does not affect the velocimetry statistics, varying the shock train location increases the root-mean-square values between 10 and 35%. Key flow structures are identified, including stagnation points, boundary-layers, and pre-heat zones to inform numerical simulations. The new flowpath design is validated by the absence of flow spillage or separation at the cavity inflow plane. This represents the first velocimetry dataset for a DNS-friendly inflow to a cavity flameholder, and the first velocimetry for free stream-seeded dual-mode scramjet flows.

Finally, combined PIV-PLIF measurements in a dual-mode scramjet combustor are conducted and constitute the first experimental database of its kind on a DNS-friendly dual-mode cavity flameholder. The knowledge of both the instantaneous flow velocities and the flame products locations enables deeper insights into the turbulence-chemistry interactions. The duct flow above the cavity remains mostly unchanged relative to the inflow to the cavity. The shear layer originating at the cavity leading edge is unsteady, hosts the reaction front, and generates periodical vortical structures wrinkling the flame. Under the shear layer, an elliptical re-circulation zone hosts two large eddies promoting mixing of cavity-generated combustion products with the premixed flow at the shear layer. Combustion in the cavity is unsteady and a hypothesis on pulsed combustion is suggested based on instantaneous PIV-PLIF and previous work. The hypothetical combustion cycle at the cavity starts with a trapped re-circulation vortex in the cavity which accumulates mass and heat. This unsustainable configuration triggers the sudden detachment of the shear layer

from the cavity ramp. Combustion products and the downstream cavity eddy escape through a streamtube contained between the cavity ramp and the shear layer. Decreasing mass and heat levels in the cavity stretch the flame thin until local extinction. The loop is closed when the shear layer re-attaches and again traps the re-circulation zone. The described oscillations, coupled with the shock train, are of critical importance to accurately prescribe DNS boundary conditions and reliably operate scramjet engines.



# Introduction

## Problem statement

As high-speed air-breathing propulsion generates growing interest for high-speed military flight, fast civil transportation, and low-cost access to space, understanding of fundamental physics governing cavity flameholders becomes ever more critical. Much of this interest is focused on flight in the Mach number range of 4 to 8. This range is associated with a decrease in gas turbine and ramjet efficiency, which calls for a particular type of scramjet known as a dual-mode scramjet. Dual-mode scramjets allow the combustion process to be either subsonic, supersonic, or a combination of the two. The engine consists of an inlet, an isolator, a combustor, and an exhaust nozzle. These engines have the ability to operate with a subsonic combustor — with a precombustion shock train located in the isolator — or with supersonic combustion predominantly without a shock train.

Cavity flameholders are a commonly-considered solution for hydrocarbon-fueled dual-mode scramjets. Hydrocarbon fuels are easier to store and handle than e.g. hydrogen and therefore considered more practical. At the high flow speeds associated with dual-mode scramjets, fuel residence time in the flowpath is however short. Hence a cavity flameholder is often used to create a recirculation region to anchor the flame. Radical species needed for flame stabilization can then be generated due to the extended molecular residence time. Stabilization of the flame reaction front is controlled by intricate coupling of shear flow dynamics, turbulence-chemistry interactions, and mass exchange between the main flow and the cavity flow. These complex flow physics span a wide range of length and time scales, requiring experimental measurement techniques and numerical prediction tools that can capture these broad scales. Current capabilities are limited to the upper range of the turbulent spatio-temporal spectra, i.e. integral scales and larger intermediate-scales. This results in varied accuracy of the numerical tools and the need for new experimental data. In addition

to applications in scramjet combustors, cavity flameholders are valuable means for fundamental research on high-speed combustion by establishing in the free stream a flame with a relatively large normal velocity.

The present work is part of a larger collaborative effort to deepen the fundamental understanding of both the effects of flow compressibility and heat release on turbulent flame structure, regimes, and stabilization mechanisms. To that end, Direct Navier-Stokes simulations (DNS) are applied. DNS simulations provide a complete representation of the flow through all temporal and physical scales, currently yielding the most accurate simulations available over other model based methods such as Large Eddy Simulation (LES) and Reynolds-Averaged Navier–Stokes (RANS) (Rauch et al., 2018). The computational cost of DNS is however very high, at an estimated 75 million CPU hours for  $\sim 8,000$  cubic millimeters in the present study, and hence current capabilities are limited to small volumes. This demands an experimental validation database with both small geometrical scales and well-defined boundary conditions. In turn, this has prompted the use of a new miniature flameholder, high resolution Particle Image Velocimetry (PIV), subsequently combined with Hydroxyl (OH) Planar Laser-Induced Fluorescence (PLIF) in the University of Virginia Supersonic Combustion Facility (UVaSCF). This facility is an electrically-heated, long-duration wind tunnel that is capable of generating conditions to adequately simulate dual-mode scramjet flight conditions with a Mach number near 5 (McDaniel et al., 2005). The present dissertation documents the implementation of the first immersed model for a DNS-friendly domain in the UVaSCF, the highest resolution velocimetry in a high-speed high-enthalpy flow using a novel pre-filtering technique, the first characterization of the flow boundary conditions for DNS on cavities, and the first study of the instantaneous interaction between the flame and the flow in a cavity flameholder. These results not only give unprecedented insights into the flow physics of cavity flameholders, but also enable the initialization of DNS, which will contribute to the investigation of flow characteristics inaccessible to experiments and will enhance general turbulence sub-models used in LES and RANS simulations.

## **Goals and contributions to the field**

Considering the need for a new experimental database, based on a miniature scramjet flameholder, and developed with comprehensive high-resolution diagnostics, three main goals are proposed for this study:

**First goal:** The broad range of combustor Mach numbers, coupled with a high heat flux environment, places a particularly constraining set of design requirements on the flameholder of a dual-mode scramjet. In this particular study, flameholding capability must be balanced against the reduction in geometrical scales, forced by the companion numerical studies, and an array of interactions between hardware and thermofluids (heat transfer, streamline distortions, choking, etc.). As will be discussed in this dissertation, these requirements become even stricter for a flameholder that is immersed in the mainstream flow as opposed to a flameholder that is traditionally located in the wall of the scramjet engine combustor. However, new additive manufacturing techniques offer novel design approaches that can push the design envelope further and enable unique experimental geometries. The first goal is therefore to *design and demonstrate operation of an immersed cavity flameholder with a DNS-friendly-small-scale geometry, well-defined boundary conditions, and adequate experimental diagnostic access.*

**Second goal:** With the new flameholder designed and demonstrated to sustain the facility's harsh conditions, the second goal of this proposed work is to adequately quantify the boundary conditions relevant to the DNS computational domain. Since shear flow dynamics, turbulence-chemistry interactions, and mass exchange are largely driven by convection, the velocity field is viewed as critical for experimental characterization. In particular, the inflow velocity field must be accurately quantified using Particle Image Velocimetry (PIV). Given the small geometrical scales of both the flameholder and the DNS, these measurements need to be performed at high resolution, preferably with resolutions as close as possible to the DNS. The second goal of this work is therefore to *assess the uniformity of boundary-conditions for the new flowpath for DNS and quantify the inflow velocity field at high resolution using PIV.*

**Third goal:** The use of DNS simulations yields an unprecedented level of detail in the combustion process which intertwines fluid mechanics and chemistry down to the smallest spatio-temporal scales. This provides motivation to obtain detailed complementary experimental measurements in parallel. One way to experimentally quantify interaction of the fluid mechanics and chemistry is through simultaneous measurements of PIV and Planar Laser Induced Fluorescence (PLIF). PLIF enables, amongst other outputs, to identify the location of the flame and the associated

heat release. Therefore, the third goal of this work is to *quantify the key characteristics of a high-speed chemically-reacting flow field associated with the velocity field and the concurrent heat release field*. To that end, simultaneous Particle Image Velocimetry (PIV) and Hydroxyl (OH) Planar Laser-Induced Fluorescence (PLIF), hereafter PIV-PLIF, are conducted on a high-speed reacting cavity flow. The benefits are threefold relative to separate PIV and PLIF acquisitions: flow-chemistry coupling is investigated with instantaneous measurements, bias towards reactants in regions of intermittent presence with products are alleviated, and complementary validation metrics are provided to companion CFD work.

The results presented below therefore constitute the first published reference dataset on a DNS-friendly high-speed reacting cavity flow.

## **Outline**

This dissertation is organized in four chapters. Chapter 1 corresponds to the first goal; chapters 2 and 3 present the methodology and the velocimetry required for goal 2; and chapter 4 presents the chemically-reacting flow field characteristics of goal 3. Finally, a conclusion summarizes the completed work and outlooks for future investigations. It is anticipated that each of the four chapters of the present dissertation will form an individual journal publication.

## Chapter 1

# Design and Testing of an Additively Manufactured Flameholder for Scramjet Flows

## 1.1 Introduction

As the need grows for high-speed military flight, fast civil transportation, and low-cost access to space, interest in hypersonic air-breathing propulsion (e.g. scramjets) is increasing. Much of this interest is focused on flight in the Mach number range of 4 to 8. This flight regime is associated with a decrease in gas turbine and ramjet engine efficiency and calls for a particular type of scramjet known as a dual-mode scramjet. Dual-mode scramjets provide for the transition between subsonic and supersonic combustion processes. The engine consists of an inlet, an isolator, a combustor, and an exhaust nozzle. When operating in the subsonic mode, the pressure difference between the inlet and the combustor is accommodated by a pre-combustion shock train in the isolator. At higher Mach numbers, the shock train is diminished and the combustor flow remains predominantly supersonic. The resulting broad range of combustor Mach numbers, coupled with a high heat flux environment, places a particularly constraining set of design requirements on the flameholder of a dual-mode scramjet. At the same time, recent advances in additive manufacturing (AM) techniques and available materials are driving new approaches to design and fabrication that have direct implications for scramjet flameholders and may lead to improved engine performance. The uniquely harsh conditions encountered in hypersonic air-breathing engines combined with AM present both novel opportunities and challenges that are the subject of this chapter .

To date, published applications of AM to hypersonic flight systems have been largely limited to impulse facilities with a low temperature increase within the material or topology optimization studies (Berridge et al., 2018; Liu et al., 2017; Rêgo et al., 2016). In a notable study exploring the potential of an additively manufactured part, Liu et al. (2017) 3D printed in aluminum and numerically simulated a nose cone model for a hypersonic vehicle using topology optimization and computational fluid dynamics (CFD) analysis. The model included an internal convective cooling system consisting of channels following the nose cone contour. Internal lattices significantly reduced the weight and the nose cone was printed in two halves to avoid interior support structures. Numerous other applications of additively manufactured parts have been reported, although not generally in peer-reviewed publications. For example, Orbital ATK announced having tested a 3D-printed hypersonic engine combustor at high-temperature hypersonic flight conditions, including “one of the longest duration propulsion wind tunnel tests ever recorded for a unit of this kind”

(Kidder, 2018). Orbital ATK is also using AM for hypersonic warheads of more complex geometries than conventionally feasible (Judson, 2018). Reaction Systems, Inc. is working on an additively manufactured endothermic fuel catalyst and heat exchanger for scramjets (Anderton, 2017) and the Air Force Research Laboratory is investigating 3D-printed ceramic for hypersonic applications (Cooper, 2018). Extensive research is also being conducted on additively manufactured rocket engine components, including nozzles, fuel injectors, turbopumps, and combustion chambers (Gradl, 2016; Gradl et al., 2018). In particular, NASA is planning to integrate 3D-printed components in the Space Launch System RS-25 engines (Harbaugh, 2017) and Aerojet Rocketdyne successfully tested a thrust chamber assembly for the RL10 rocket engine (Rocketdyne, 2017). Jet engines and gas turbines have achieved significant milestones in efficiency with additively manufactured parts (Madara and Selvan, 2017). The Power and Gas Division of Siemens demonstrated the use of turbine blades 3D printed out of a powdered polycrystalline nickel-based superalloy in 2017 (Siebert, 2017). Finally, General Electric broke the net efficiency record for a power plant gas turbine by enhancing fuel/air mixing in the gas turbine with the use of complex geometries enabled by AM and their operational GE9X jet engines currently include 3D-printed fuel nozzles (Kellner, 2018).

At the high flow speeds associated with dual-mode scramjets, fuel residence time in the flow path is short, on the order of milliseconds. Further, practical considerations such as energy density and fuel storage motivate the use of hydrocarbon fuels that have relatively slower reaction rates as compared to hydrogen fuel. To compensate for the longer reaction times and allow for steady, stable combustion, hydrocarbon fuels may be premixed upstream of the combustor and a cavity flameholder is typically employed to create a recirculation region over which to anchor the flame (Ben-Yakar and Hanson, 2001; Gruber et al., 2018). Radical species needed for flame stabilization can then be generated thanks to the extended molecular residence time. Stabilization of the flame reaction front is then controlled by an intricate coupling of shear flow dynamics, turbulence-chemistry interactions, and mass exchange between the main flow and the cavity flow. These complex flow physics span a wide range of length and time scales, requiring experimental measurement techniques and numerical prediction tools that can capture these broad scales. Current experimental and numerical capabilities are limited to the upper range of the turbulent spatio-temporal spectra, i.e. integral scales and larger intermediate scales, resulting in varied accuracy of the numerical tools and the need for new experimental data.

As part of an effort to better understand the dynamics of cavity-stabilized, high-speed flames, a small-scale cavity flameholder for scramjet flows has been designed, additively manufactured, and tested in the University of Virginia Supersonic Combustion Facility (UVaSCF). This facility is an electrically-heated, long-duration wind tunnel that is capable of generating a Mach 2 flow with a total temperature of 1200 K and a total pressure of 300 kPa - conditions representative of a dual-mode scramjet engine inlet for a vehicle operating at a flight Mach number of 5 and an altitude of approximately 20 km (McDaniel et al., 2005). At these temperatures, commonly used super alloy materials can approach thermal limits. With additional thermal energy from combustion, static temperatures in the flow can easily reach values over 2600 K, which can lead to catastrophic structural failures without adequate cooling. For this study, the flameholder was designed to sustain a premixed ethylene flame with static temperatures in excess of 2600 K in a Mach 0.6 to 0.8 flow. This Mach number range is representative of the conditions downstream of an isolator shock train when the dual-mode combustor is operating in the subsonic mode. This work is part of a collaborative study that seeks to further the fundamental understanding of the effects of flow compressibility and heat release on turbulent flame structure, combustion regimes, and stabilization mechanisms. To that end, direct numerical simulation (DNS) CFD simulations are being conducted in a parallel activity to the experimental work discussed in this chapter Rauch et al. (2018). For this flow regime, accurate DNS requires an experimental validation database of flame structure with both small geometrical scales and well defined boundary conditions. As a result, an immersed wind tunnel model was conceived for the flameholder that would reduce the DNS computational domain and minimize boundary layer growth upstream of the cavity. Minimizing aerodynamic blockage and managing heat loads were then the primary design drivers and needed to be addressed within strict constraints imposed by both the facility and diagnostic methods.

This chapter has three objectives: 1) present the methodology developed for the design and fabrication of an air-breathing hypersonic propulsion flameholder using AM, 2) validate the design with experimental results, and 3) provide recommendations for future designs that are to be additively manufactured. The chapter documents the development and demonstration of a new capability enabling the study of high-speed flameholders at the scale of DNS and presents, to our knowledge, the first published methodology for the design and fabrication of additively manufactured scramjet combustor components. This study also represents the first conversion of a direct-connect,

high-speed combustion wind tunnel to a semi-free jet configuration. Finally, results are presented for the longest duration test of an additively manufactured cavity flameholder supporting a flame in real high-speed flow conditions.

The chapter is structured as follows. In the first part, the methodology and setup are presented, including the design requirements, constraints, and the iterative design process. The latter was supported with Finite Element Analysis (FEA) by Robert Rockwell (Lieber et al., 2018a) and preliminary wind tunnel testing. In the second part, results from the fabrication process and performance results are assessed, in particular wind tunnel tests at operating conditions are presented. Recommendations are also provided for the design of similar parts. Finally, a summary and suggested future work are presented in the conclusion.

## 1.2 Design Requirements and Methodology

A methodology was developed as part of this work using CFD and FEA analysis, iterative AM, and preliminary wind tunnel testing. The design requirements and constraints, chosen fabrication process, and the final experimental setup are presented below.

### 1.2.1 Design Requirements

The most critical design requirement was to optimize the flameholder for both numerical simulation and experiments, while making fabrication reliable and economical. DNS simulations promise a complete representation of the flow through all temporal and spatial scales, yielding the most accurate CFD simulations available over other model-based methods such as Large Eddy Simulation (LES) and Reynolds-Averaged Navier–Stokes (RANS) (Rauch et al., 2018). Unfortunately, the computational cost of DNS is very high, at an estimated 75 million CPU hours for the 8,000 cubic millimeter volume considered for this study. Hence, current DNS capabilities are limited to small volumes. This constraint precludes simulation of any significant portion of the upstream flow path including any isolator shock train and upstream boundary layers. Instead, experimental velocity and turbulence measurements as close to the cavity as possible are needed to generate appropriate DNS inflow conditions.

Thus, a strut-supported flameholder was conceived that would serve to simplify characterization of the cavity inflow condition and minimize the DNS computational domain. Using a strut allows the original wall boundary layer to be bled ahead of the DNS computational domain and the calculation can be initialized from that point. Several key features of the adopted flow path geometry and the dual-mode operating regime are illustrated in Fig. 1.1. These include (a) fuel premixing upstream of the flameholder, (b) establishment of a shock train in the isolator section, which reduces the Mach number of the flow from 2 to approximately 0.6 to 0.8 depending on the length of the shock train, (c) generation of flow turbulence of various length scales and frequencies due to fuel injection and shock-boundary layer interactions, (d) the cavity flameholder supported away from the wall in the diverging section, and (e) an air throttle to back pressure the combustor and control the shock train location in the isolator. Two rows of fuel injectors placed just downstream of the facility nozzle allow for premixing of the fuel with the main air flow upstream of the flameholder.

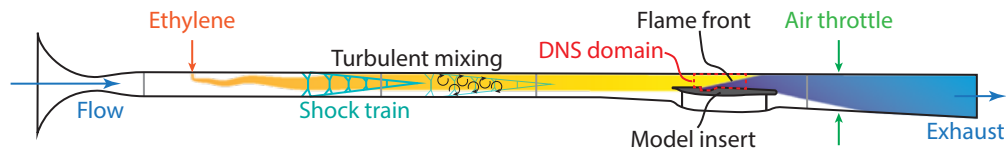


Figure 1.1: Schematic of the facility flow path with small-scale cavity flameholder identifying important flow features.

The critical cavity size, or corresponding cavity residence time, that supports flameholding depends on many factors including local fuel equivalence ratio, temperature, pressure, mass exchange rate or mixing between the cavity and the main flow, and shear layer dynamics. In addition to cavity residence time, two leading factors affecting flameholding are mixing rates between combustion products and the main flow and local static temperature. Ignition delay analysis was performed to assess both effects and a scaling factor of one-third relative to a previously investigated cavity flameholder (Rockwell et al., 2017) was chosen as a compromise between the DNS computational cost and reduced residence time. The residence time of the previously studied large cavity was estimated to be about 2 ms (Ramesh et al., 2018) and the scaled-down cavity has an estimated residence time of 0.6 ms. The original 22.5 degree ramped cavity of Ref. (Rockwell et al., 2017) is hence scaled down in length and depth to  $L = 18$  mm and  $H = 3$  mm, respectively (Fig. 1.2). The original span of  $W = 38$  mm is preserved to extend across the entire width of the duct, maintaining approximate two-dimensionality in the core flow.

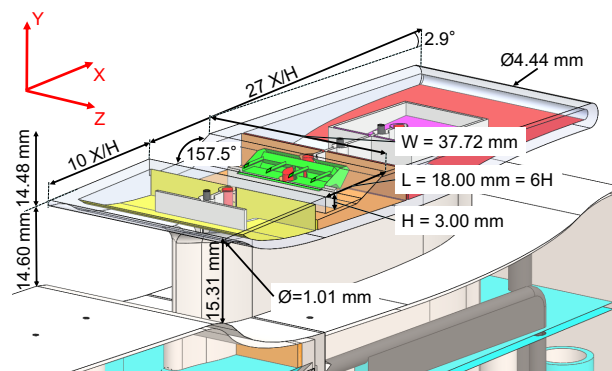


Figure 1.2: Flameholder insert geometry with key dimensions. Cooling passages are in yellow, orange, red, magenta, and cyan; fuel lines in green; thermocouples in red; and pressure taps in dark grey.

Details of the strut-supported flameholder design are shown in Fig. 1.2. A round leading edge followed by a surface of length  $10 \cdot H$  produces a new boundary layer ahead of the cavity.

Downstream, the 2.9 degree divergence from the combustor wall (Rockwell et al., 2017) is matched over a length of  $27 \cdot H$  to delay thermal choking. The resulting simulation-friendly geometry consists of a raised insert that is immersed in the original direct-connect flow path. The insert leading edge is located at half the local duct height (14.5 mm) in order to capture the premixed region of the flow (Cantu et al., 2016a) while remaining offset from the boundary layers.

Additional requirements were imposed by the facility test-section hardware and application of several advanced laser-based measurement techniques. The UVaSCF combustor was designed as a modular setup consisting of a rectangular cage and four walls (Rockwell et al., 2014). The part designed in this study constitutes one of the latter walls, which are sealed with a flange compressing O-rings against the outer surface of the cage. The combustor side walls can be fitted with large fused-silica windows (Rockwell et al., 2014) for particle image velocimetry (PIV) (Kirik et al., 2017; Rice et al., 2015) or planar laser induced fluorescence (PLIF) (Cantu et al., 2016a). The windows are interchangeable with air-purged slotted walls for coherent anti-Stokes Raman spectroscopy (CARS) measurements (Cutler et al., 2018, 2014). The nature of the test-section construction means access for cooling and instrumentation in the flameholder is restricted to one side of the flow path. The CARS slots constrain the design even further by setting four measurement planes as fixed locations in the combustor. The flameholder was therefore positioned in the combustor with CARS measurement planes immediately upstream of the leading edge, as well as in and downstream of the cavity (Fig. 1.3). Pressure taps and thermocouples were subsequently distributed upstream of, in, and downstream of the cavity for monitoring of the flame location and hardware conditions (Fig. 1.4). Ceramic paper gaskets glued onto the sides of the insert provide insulation between the insert and the combustor sidewalls and also serve to isolate the streamtubes above and below the flameholder.

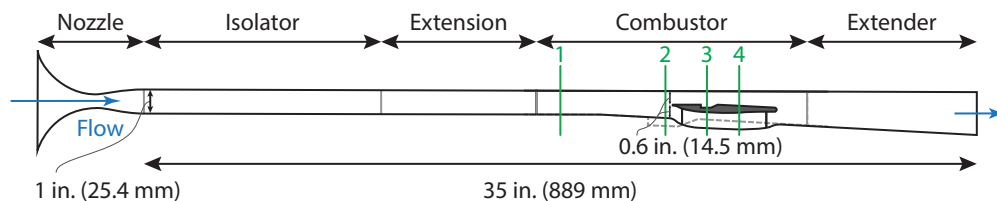


Figure 1.3: Side view of the flow path showing the immersed flameholder. The previous configuration outline with the larger cavity is shown in dashed grey. CARS measurement planes are indicated in green.

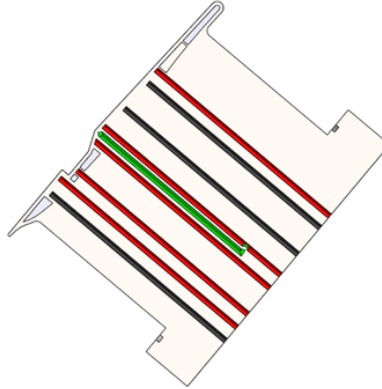


Figure 1.4: Centerplane section with pressure taps in grey, thermocouples in red, and fuel line in green. The part is oriented at  $45^\circ$  as during manufacturing.

Finally, the facility ignition procedure involves injecting hydrogen directly into the cavity to achieve autoignition. Ethylene is then introduced through the upstream fuel injectors and the hydrogen is turned off once an ethylene equivalence ratio within the stable range is reached (Rockwell et al., 2017). Four fuel injectors were therefore included on the surface of the cavity close-out ramp. These injectors are spaced symmetrically about the ramp centerline, 0.75 mm above the cavity floor (see Fig. 1.2). They are supplied by a common fuel line and injection is parallel to the cavity floor. The injectors are designed as rhombi with 45 degree corner angles to create vertical-enhanced mixing. Pure ethylene or an air-ethylene mixture can also be fed through these lines in order to directly fuel the cavity and potentially increase the flame angle relative to the free stream.

The design requirements for the new flameholder can then be summarized as follows:

1. Enable DNS through small experimental geometric dimensions and well-defined inflow boundary conditions at the cavity,
2. Provide access for a variety of experimental diagnostics, including sensors and advanced, laser-based measurement techniques,
3. Provide a means of ignition for the cavity-stabilized flame and direct-cavity fuel injection to potentially increase the flame angle into the free stream,
4. Limit flow path blockage to permit supersonic start of the main facility nozzle and establishment of Mach 2 flow in the isolator, and

5. Survive thermal and structural stresses under a premixed ethylene flame for repeated cycles lasting as long as an hour.

The last two requirements relate to the safe operation of the facility over long-duration testing. As will be seen, heat removal from the geometry shown in Fig. 1.2 is a significant challenge and, in this case, must be achieved through the narrow cross-section of the strut.

### 1.2.2 Additive Manufacturing

The shapes and geometrical scales imposed by the constraints of DNS and the facility would be very expensive to achieve using conventional fabrication techniques, e.g. drilling, milling, and brazing or injection molding. In contrast, AM progressively add material to form a solid part. The nature of this technique enables a wide range of new designs and features. For example, building a part from the inside out permits complex internal geometries that can serve as cooling passages for high heat flux applications such as a scramjet combustor. Interlocked or embedded assemblies may be “grown” in a single fabrication step and efficient construction approaches such as thin shells and lattices that reduce material cost and weight can be employed. Finally, AM enables the easier use of materials such as Inconel and Monel that are very difficult and expensive to machine conventionally.

As the AM industry adds more available material types and improves the quality of finished parts, advanced applications that may have been impossible or cost prohibitive with conventional machining are emerging. Saunders sorted the benefits of AM into a staircase model as follows (Saunders, 2015):

1. Rapid prototypes and tooling (manufacturing while designing, injection molds, etc.),
2. Direct part replacement (easier assembly, material savings, etc.),
3. Part consolidation (joints-free parts, complex features out of a simple process, etc.),
4. Designed for AM (optimized designs taking full advantage of AM including 1-3 above).

It is step 4 that holds the greatest potential for hypersonic propulsion applications, with new possibilities such as porous volumes, lattices of varying stiffness, and increased heat transfer through optimized geometries.

AM in metal is increasingly used for prototyping and production of aerospace components and is particularly applicable to the present study due to the high heat fluxes associated with hypersonic propulsion. A common printing technique is Direct Metal Laser Sintering (DMLS), which uses a focused laser to sinter layers of metal powder together (Frazier, 2014). The part is grown up from a build plate with layers of fresh powder progressively stacked in the powder bed. Print times are on the order of 10-20 hours for the current design. Typical layer thicknesses are 0.0008 in. (0.02 mm) and print resolutions within a layer can reach 0.0012 in. (0.3 mm). DMLS provides higher print resolutions than alternative metal AM techniques such as electron beam printing (Frazier, 2014).

While AM enables new geometries and features, the technique also has specific constraints for the designer and the manufacturer. First, each printed layer must have a solid support underneath it. A general manufacturing guideline restricts overhangs to angles greater than 45 degrees relative to the horizontal or to radii greater than 0.06 inches (1.5 mm). Beyond these limits, a support structure in the form of a lattice must be incorporated into the design. The lattice is in some cases difficult or impossible to remove, e.g. within intricate interior cavities. Second, the process involves the sudden heating of one localized spot in order to sinter the powder, which can result in residual stresses as the sintered spot cools down. Undesirable deformations or even cracks may result if these stresses are not managed properly. The extent of this phenomenon is specific to each design, although it is generally recommended to minimize the sintered area of each layer, which can be achieved through print orientation, use of hollow volumes, or splitting the construction into several parts. Another potential consequence of localized heating is laser burn. As heat propagates away from the sintering spot, it can partially sinter neighboring powder resulting in a rough surface, loose agglomerates, or even stalactites. Such features may be a concern, for example, with internal cooling channels where flow rates are critical. Third, unsintered powder may be trapped inside hollow sections of the part during the printing process and is typically removed by tumbling or flushing the part. With critical internal features such as cooling lines, it is therefore important to ensure adequate escape passages for the powder at the design stage prior to printing. Finally, less common issues such as thin walls, excessive porosity, printing head positioning errors, variable powder diameters, or the size of the printer further condition the feasibility of a print. AM is therefore not appropriate for every application and should be considered on a case-by-case basis. Considering the small dimensions, intricate internal and external geometry, a need for high strength

material such as Inconel, and the unit volume production of this study, DMLS was selected as both the most economical and feasible fabrication method. The manufacturing process was contracted with GPI Prototype, which used an EOS M290 machine with a standard Inconel 718 powder and a mean grain size in the 30 to 80  $\mu\text{m}$  range.

Once printed, the additively manufactured part must be post-processed before delivery. Cleaning of powder can involve bulk removal, brushing, tumbling, shaking, and flushing. Depending on requirements, surface or heat treatments can be applied. Conventional machining is required to remove support structures and add specific features such as threads. Post-print machining, however, was found to be a risky process, as distortions from residual stresses can lead to machining errors and shavings can become lodged in complex geometries such as internal channels or lattices.

### 1.2.3 Transformation into a semi-free jet configuration flow path

The introduction of the raised flameholder into the UVaSCF direct-connect combustor flow path effectively transformed the facility into a semi-free jet configuration with an immersed tunnel model. This represents a significant change in the facility operation and an array of challenges ensued, including dealing with tunnel blockage as well as increased thermal loads and stresses.

The additional tunnel blockage was extensively studied experimentally. Initial attempts to support the flameholder from the downstream end of the combustor as a cantilevered sting led to a full tunnel unstart. It was concluded that while the effective minimum flow path area dictates the shock train location, local flow features including boundary layers and separated flow regions choked the strut-side streamtubes, which in turn led to full unstart. An area relief was therefore added to the wall section below the flameholder and elliptically-contoured in order to avoid separated flow and stagnation points (see Figs. 1.2 and 1.3). This area relief also provided more flexibility in the design by accommodating the strut, which alleviated bending and vibrations due to local pressure variations around the cantilevered insert. The strut was also contoured with ellipses in order to smoothly divert the flow and was compensated by a larger area relief into the wall (Fig. 1.2). Integration of sensors and cooling was then straightforward through the strut. Three pressure taps and five thermocouples were included to provide live monitoring of the experimental hardware as well as reference data for optical diagnostics (Fig. 1.2).

Thermal loads and stresses were expected to be significantly higher in an inserted part due to thin immersed volumes, high temperatures, and strong thermal gradients across the immersed part. Thus, internal cooling channels were designed using detailed thermal-structural FEA at each design iteration. FEA was performed in ANSYS<sup>TM</sup> by Robert Rockwell using conventional thermal-structural elements. For full details on the techniques and the heat flux boundary conditions from a previous collaborative CFD-FEA study, the reader is referred to (Rockwell et al., 2014). A series of design iterations led to a cooling loop arrangement with four independent loops (Fig. 1.5) to balance geometrical constraints, heat removal demand, and coolant flow pressure drops across the channels.

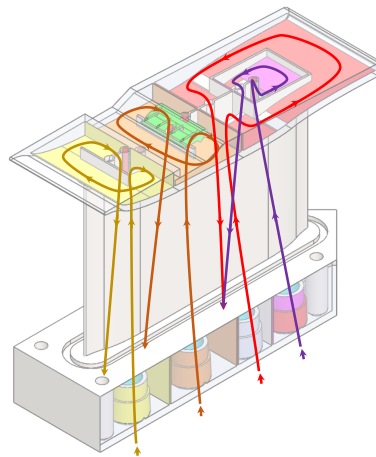
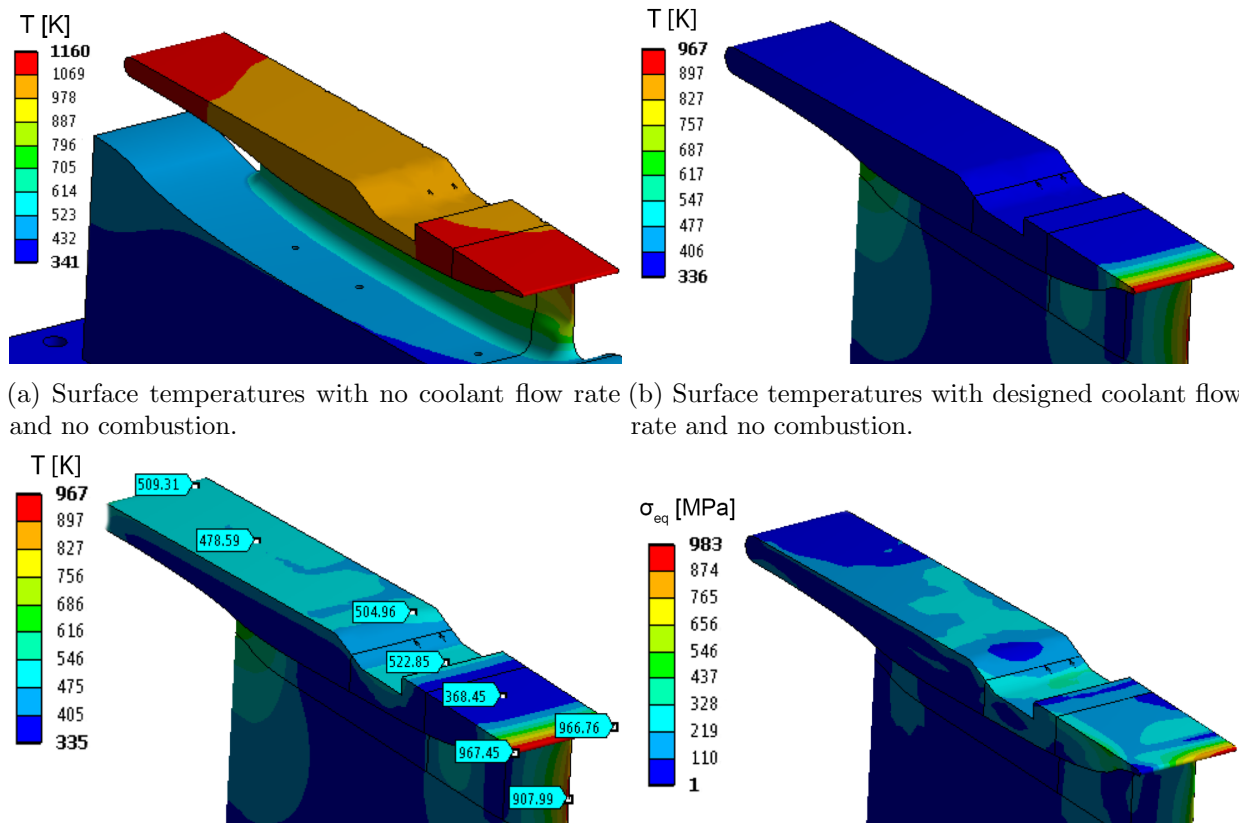


Figure 1.5: Isometric view highlighting the cooling channels arrangement in yellow, orange, red, and purple.

Despite extensive internal cooling, Inconel 718 was required to manage the thermal loads and mechanical stresses, in particular along the leading edge of the insert and strut (Fig. 1.6). Figure 1.6a shows the predicted surface temperature of the insert with exposure to a stagnation temperature of 1200 K in a  $M=0.6$ , non-reacting flow, with no coolant flow rate. Figure 1.6b shows the same with the designed coolant flow of 50/50 ethylene glycol and water at approximately 1 gallon per minute (3.8 L/min) per cooling channel. These results are consistent with experimental images shown in Fig. 1.8a and 1.8b, respectively, and gave confidence in the coolant flow and material models used in the FEA. It should be noted that the cooling passages were initially designed as circular tubes with a 1 mm diameter. Following very low coolant flow rates (see section 1.3.1), the passages were expanded to fill much of the internal volume of the flameholder with 0.05 in. (1.27

mm) exterior walls (Fig. 1.2). The strut was actively cooled by acting as a junction between the flameholder and ports outside the tunnel connected to the facility cooling system.



(a) Surface temperatures with no coolant flow rate and no combustion. (b) Surface temperatures with designed coolant flow rate and no combustion.

(c) Surface temperatures with designed coolant flow rate and combustion. (d) Equivalent stresses (MPa) with designed coolant flow rate and combustion.

Figure 1.6: FEA calculation of the Inconel 718 cavity flameholder by Robert Rockwell (Lieber et al., 2018a).

Figure 1.6c shows the predicted surface temperature with an ethylene flame anchored on the cavity. Although the flow static temperatures are highest in the combusting region of the flow, the proximity of the cooling passages keeps temperatures largely below 550 K. The flow-facing extremities at the flameholder and strut leading edges have the highest expected temperatures with a maximum of 967 K along the flameholder leading edge. This temperature is below the reported maximum operating temperature of 980 K for Inconel 718, although the low margin suggests inspection and monitoring of the leading edges during testing. Additionally, differential thermal growth of the upstream portion of the insert produces a significant mechanical stress as shown in Fig. 1.6d. The maximum equivalent von-Mises stresses in the FEA is about 10% below

the material yield strength of 1075 MPa. Again, inspection and monitoring of the part is suggested. Fortunately, this high stress area is also highly localized and experimental usage has demonstrated that these stresses are below rupture even for repeated cycles. Lastly, lateral thermal growth of the inserts was a concern due to the presence of fused silica windows on either side of the flameholder. Gaps of 7.5/1000 in. (0.19 mm) between the sides of the insert and the windows were included to account for thermal growth while preserving the integrity of the windows.

#### 1.2.4 Modularity

A modular design was conceived for the present study. This consisted of splitting the main wall along its span and clamping the flameholder strut in between (Fig. 1.7). Splitting large parts has the potential to lower printing costs by providing flexibility in the arrangement of parts on the printing plate: wide or high pieces can be laid out more efficiently. Additional benefits of the modular design include the ability to easily swap flameholder geometries, adjust the height of the flameholder into the flow path, and distribute the risk of fabrication failure across three parts. The two main wall parts are labeled in the following upstream and downstream wall respectively. Sealing from the flow path was ensured with a flange, as well as compressed O-rings and silicone room temperature vulcanizing sealant.

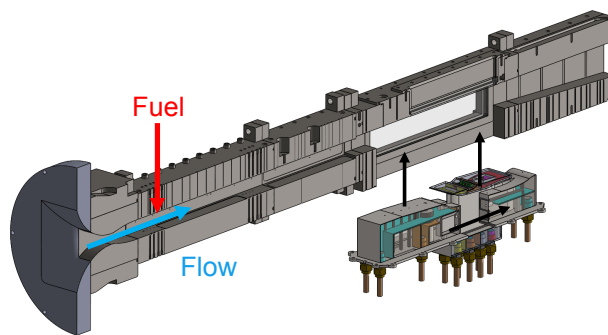


Figure 1.7: Modular design and assembly into the UVaSCF flow path.

Lattices were considered in the cooling passages as both a structural support and an enhancement to the heat exchange by providing more surface area and increasing turbulence in the coolant flow. FEA studies, however, predicted such structures to be both structurally and thermally unnecessary. In addition, a careful design along with a 45-degree inclination on the printing plate avoided overhangs with support structures (Fig. 1.4). In order to optimize powder removal and coolant

flow rates, the cooling passages were designed as cavities, filling the entire inner volume of the flameholder and strut. The external skin thickness is 0.05 inches (1.27 mm). Guide walls were used to force the coolant into sides and corners (Fig. 1.2). This “hollow volume” concept was extended to the two wall parts in order to reduce both residual stresses and fabrication costs.

Post-print machining was necessary for threads and geometrical accuracy on key dimensions: the printed flameholder showed significant bending and shrinking of its aft (see section 1.3.2). This is common in AM of metals, as the thermal stresses originating from the laser spot compound over layers and distort the part. To compensate for these geometrical errors, a layer of material was added to all upper surfaces in the CAD model, which was then milled off to the required geometry. Because deformations in AM can be severe, a new coordinate system for machining may be needed, otherwise excessive removal of material may result. A comparison of the CAD geometry with the printed geometry revealed that geometries closest to the build plate matched design dimensions best. This is consistent with the known trend of the print accuracy which decreases away from the build plate.

The above methodology and setup were the result of several iterations in fabrication, with improvements added after tests were performed on each part. Section 1.3 presents this work and demonstrates the validity of the final design with results from extensive tunnel testing.

## 1.3 Design Iterations and Results

This section presents results from the fabrication process, including failures, and assesses the final design through a report of tunnel testing at operating conditions. Table 1.1 summarizes the design iterations and test results.

Table 1.1: Design iterations of the flameholder insert.

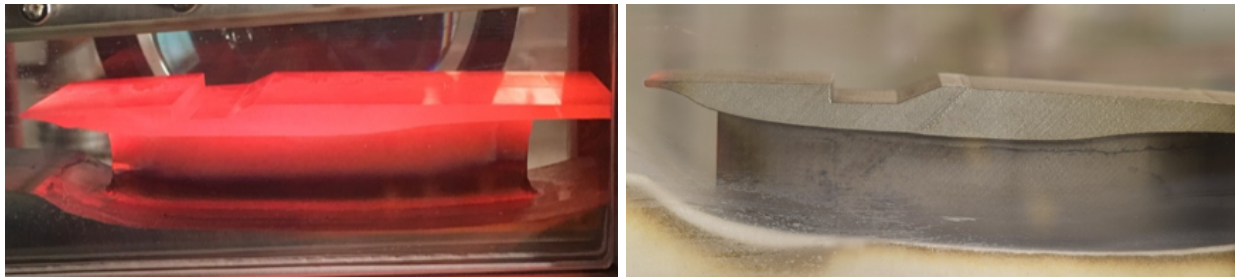
ITERATION	STATUS	DESCRIPTION
1	Thermal failure	Single part flameholder comprising the insert, strut, and facility wall. Circular cooling lines of diameter 0.039 inches (1 mm).
2	Thermal failure	Single part flameholder comprising the insert, strut, and facility wall. Circular cooling lines of diameter 0.045 inches (1.14 mm).
3	Operational	Three parts modular shell design.

### 1.3.1 First two prints

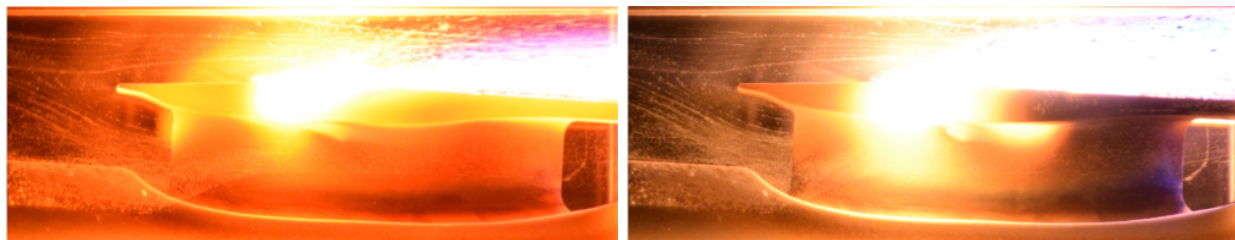
Iterations 1 and 2 of table 1.1 failed due to bending of the part from residual stresses. This resulted in post print machining that breached fuel and cooling lines. These two designs were printed flat on the build plate as one part instead of three inclined parts, as in the modular design (Iteration 3). Hence residual stresses from sintering large cross-sectional areas, compounded over several layers, were suspected to be very high. Furthermore, severe blockage of the circular cooling lines — from sintered residual powder present in the form of either surface roughness, stalactites, and/or agglomerates — prevented adequate cooling flow rates throughout the part.

Repairs and modifications enabled test runs with these parts in an attempt to demonstrate flameholding. The tunnel is run at a total temperature of  $T_0 = 1200$  K and total pressure of  $p_0 = 300$  kPaa. The local flow Mach number at the cavity is  $M \sim 0.6$  and the ethylene-air mixture has a global equivalence ratio  $\Phi_g \sim 0.4$ . Figure 1.8 shows several photographs taken during the test run of the second printed part, with larger circular cooling lines of diameter 1.5 mm. Figure 1.8a shows the part prior to ignition. The entire flameholder plate was glowing from insufficient coolant flow rates but the strut was notably cooler (darker) and additional cool spots were observed in the middle of the plate in the vicinity of the cooling lines. Based on the color of the glowing part, the surface temperature was estimated to be on the order of 1000 to 1100 K, which is consistent

with the FEA prediction for these conditions with no cooling in the strut or plate. FEA for these conditions (following ignition) predicted the part's failure. However, it was deemed to be valuable to see if the geometry was capable of flameholding for even a short period. Figures 1.8c and 1.8d show the part during and soon after ignition. Ethylene ignition was successfully achieved by first injecting hydrogen in the cavity, which self-ignited and anchored a flame onto the leading edge, then ethylene upstream of the isolator. Upon reaching a given ethylene equivalence ratio, hydrogen was to be turned off and the ethylene flame sustain itself. Soon after ignition, however, melting was observed on the top surface of the insert in the vicinity of the ramp close out and the test was terminated. The cool region on the right of Fig. 1.8d is due to the increase in coolant flow rate through a breach in the cooling line. Post-test inspection revealed that complete blockage of several cooling lines occurred during the test either from displaced residual powder, thermal collapse, or some combination of the two.



(a) Failed design glowing due to almost no coolant flow rate. (b) Successful design with required coolant flow rate.



(c) Ignition of the failed insert.

(d) Post-ignition melting of the failed insert.

Figure 1.8: Visible light images acquired during test runs.

### 1.3.2 Third print: modular insert assembly

The above issues motivated the three-parts hollow design shown in Fig. 1.7. A shell design with cooling cavities taking most of the internal volume (in yellow, orange, red, and magenta in Fig. 1.2) solved this problem with flow rates of about 1 gallon/minute, i.e. ten times the minimum flow rate.

Furthermore, this third design was made modular by manufacturing the facility wall in two pieces and clamping the flameholder insert in between as illustrated in Fig. 1.7. An added benefit of the modular design is the ability to swap immersed geometries with lower costs and delays. The three parts were additively manufactured at an inclination of  $45^\circ$  to alleviate excessive residual stresses.

While no structural failure nor insufficient flow rates occurred from residual stresses, the latter remain present and distorted the part. Figure 1.9 present the outline of the fabricated flameholder insert in solid grey over the CAD geometry in white. The primary discrepancies were: a rear-facing step angle larger than 90 degrees; a step discontinuity on the divergence past the cavity ramp; a progressive bend towards the aft; and a shorter overall length. The insert width was within 0.007 in. (0.18 mm) as specified. The two wall parts experienced worse distortions up to 0.035 in. (0.089 mm) due to its larger number of print layers. Machining, sanding, and sealing however ensured a good fit into the tunnel cage.

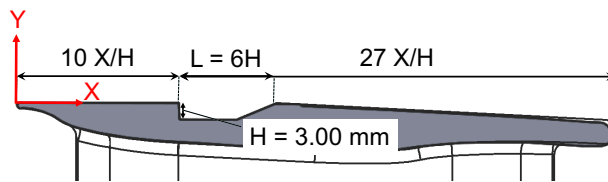


Figure 1.9: Modular design and assembly into the UVaSCF flow path.

The above listed distortions on the insert flameholder geometry prompted a new fabrication where 0.05 in. (1.27 mm) were added to the cavity-side surfaces, exceeding the maximum difference in dimensions observed with iteration 3. Top surfaces were machined using Electric-Discharge Machining (EDM) with a specified surface roughness of  $32 \mu\text{in}$  ( $0.8 \mu\text{m}$ ). Since the top surfaces were most critical, the referential for machining was set on the leading edge with one axis normal to the surface between the leading edge and the cavity. This corresponds to the surface closest to the building plate, which was observed to incur the least distortion. This fabricated part was validated with caliper measurements and will be tested in the tunnel in the near future.

Tunnel runs validated the successful flameholding and operation of the design. All runs were set at a total temperature of  $T_0 = 1200 \text{ K}$  and total pressure  $p_0 = 300 \text{ kPa}$ . Measurements included static wall pressures and temperatures, as well as chemiluminescence. CH is a combustion radical in the reaction of ethylene, which chemiluminescence in the blue indicates the flame presence. Figure 1.10 displays its chemiluminescence acquired at a global equivalence ratio of  $\Phi_g = 0.434$  and depicts

stable flameholding. The observed reaction front angle remained nearly the same as the previous full-sized cavity flameholder with  $H = 9$  mm,  $L = 50$  mm Rockwell et al. (2017). No signal is detected upstream of the cavity or under the insert, demonstrating that chemical reactions are solely initiated at the cavity and anchored over the cavity. The insert remained intact after many hours of operation over several months. As expected due to the smaller geometrical scales, the operability range as a function of the equivalence ratio  $\Phi_g$  was narrower when compared with the previously used large cavity flameholder. The measured axial pressure distributions were consistent with dual-mode scramjet operation in the subsonic mode, i.e. supersonic inflow and subsonic combustion, separated by a shock train. Pressure traces 1 and 2 in Fig. 1.11 show initial conditions with a fully started flow path up to the flameholder insert; a minimum backpressure is imposed with the air throttle to enable flame stabilization. The upper limit of global equivalence ratio of the facility is primarily dictated by the thermal choking occurring downstream of the cavity, typically at a location where the area ratio is about 1.44. For the scale-down cavity insert, this higher limit occurred at a global equivalence ratio of about 0.434, corresponding to pressure trace 3 with the shock train pushed upstream to  $X/H \sim -140$ . The resulting Mach number at the insert is  $M = 0.66$  using a one-dimensional Fanno flow and shock train analysis (Heiser et al., 1994; Rockwell et al., 2017) based on experimental pressure data. Previous work had shown a limit of 0.42 with the large cavity (Rockwell et al., 2017). The lowest global equivalence ratio  $\Phi_g$  that was able to anchor a flame in present configuration was about 0.365, which is higher than the lower limit of 0.28 for the large cavity (Rockwell et al., 2017). Since only one-half of the injectors were turned on in present experiment (i.e. only the injectors on the top wall in Fig. 1.1), the local equivalence ratio ( $\Phi_l$ ) at the cavity insert is nearly the double of the global equivalence ratio. In other words, the scaled down cavity requires a much higher local equivalence ratio to flamehold at similar local flow conditions, i.e. Mach number, static temperature, and pressure. The corresponding pressure trace 4 shows the shock train located  $X/H \sim -100$ , leading to a Mach number of  $M = 0.74$ . When maintaining this low equivalence ratio while pushing the shock train back to  $X/H \sim -140$ , pressure traces overlap (trace 5 vs. 3) and the Mach numbers of  $\Phi_g = 0.434$  and  $\Phi_g = 0.365$  match. These extreme flow conditions define cases 1, 2, and 3 of the test matrix summarized in table 1.2 with key parameters detailed in table 1.3. They respectively correspond to a low Mach number/high heat release, high Mach number/low heat release, and low Mach number/low heat release case. These cases will in

turn enable the study of discernable trends in combustion dynamics relative to flow compressibility and heat release. Case 4 is identical to case 1 with the exception of a non-ignited flow in order to isolate the effect of heat release on turbulence in future studies.

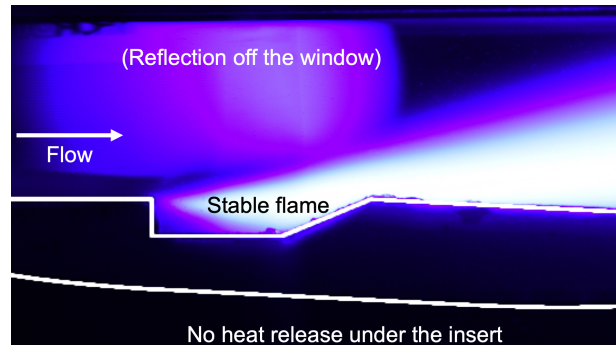


Figure 1.10: CH chemiluminescence of a premixed ethylene-air flame stabilized over the scaled-down cavity of iteration 3 of table 1.1 with inflow conditions at  $M = 0.6$ ,  $T_0 = 1200$  K,  $p_0 = 300$  kPa and an equivalence ratio  $\Phi_g = 0.43$ .

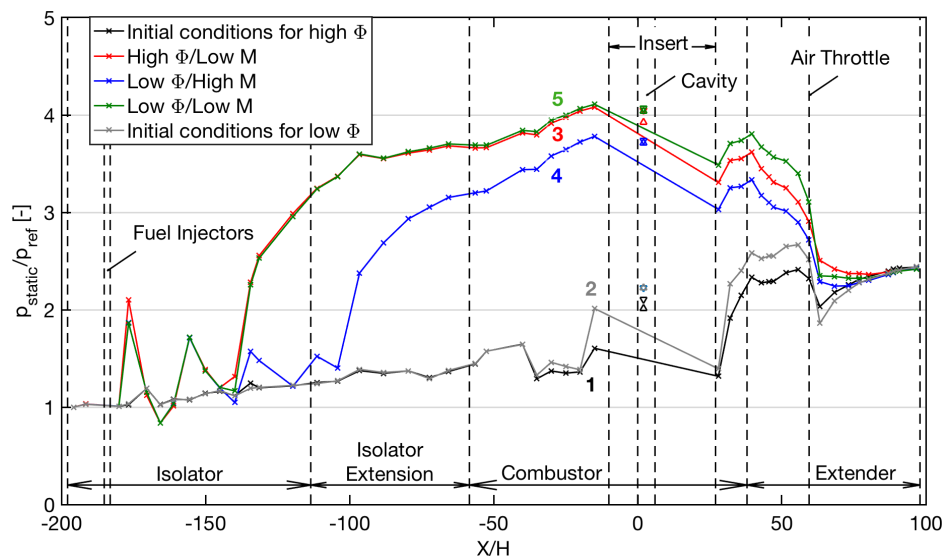


Figure 1.11: Pressure traces with the flameholder insert. The X-axis is normalized by the cavity height ( $H = 3$  mm).  $p_{ref}$  is the corresponding pressure immediately past the converging-diverging nozzle for each trace.  $X/H = 1$  data taken below the insert.

Table 1.2: Test matrix.

	High heat release	Low heat release	No heat release
High Mach number	-	Case 2	-
Low Mach number	Case 1	Case 3	Case 4

Table 1.3: Flow parameters computed by Robert Rockwell for the in-situ tests described in section 1.3.2. Plenum refers to conditions prior to the tunnel converging-diverging nozzle. Uncertainty includes instrumentation uncertainty and temporal variability of the facility and fuel system.

Parameter	Case 1	Case 2	Case 3	Case 4
Plenum Total Pressure $p_0$		$(300 \pm 3)$ kPaa (1%)		
Plenum Total Temperature $T_0$		$(1200 \pm 9)$ K (0.8%)		
Global Equivalence Ratio $\Phi_g$	$0.47 \pm 0.03$ (6.6%)	$0.37 \pm 0.01$ (4.0%)	$0.37 \pm 0.01$ (4.0%)	$0.47 \pm 0.03$ (6.6%)
Air Throttle Setting	Minimum for flameholding		Pressure trace match with case 1	
Mach Number $M$	0.66	0.74	0.66	0.66

## 1.4 Discussion and Recommendations for Designs of Additive Manufactured Parts

Based on the results of this study, guidelines are proposed to render the above iterative process more efficient in the design and fabrication of additively manufactured parts in air-breathing hypersonic propulsion.

Internal channel blockage was the primary cause for failure in our application. While the circular channels on iterations 1 and 2 were designed for adequate cooling rates within allowed the diameter range for additively manufactured internal channels, the cumulation of residual powder, laser burns, and partially sintered powder along the channel length mostly or completely blocked the cooling passages. Attempts to flush powder out were insufficient to prevent failure. As predicted by the FEA for the measured flow rates, the part quickly reached glowing temperatures as the tunnel heat up and exceeded the melting point of Inconel 718 with the flame on. Should there be no access to the internal features for post-print machining, planning for powder escape routes, building angular overhangs, or maximizing the cross-sectional area is recommended. For the latter, AM allows the fabrication of complex shells as long as the tangent to internal surfaces does not exceed 45 degrees relative to the horizontal plane.

The second main issue encountered was residual stresses. These occur when several dense layers of sintered metal powder are compounded over several layers, e.g. a solid part printed flat on the surface. Residual stresses lead to bending or cracks and critical problems during machining can ensue. The difficulty in predicting them with e.g. FEA motivates more general guidelines including printing long blocks at an angle to decrease the cross-sectional area, splitting one part into several to be assembled, and printing shells/lattices.

In summary, AM enables novel designs and efficient prototyping but comes with a set of restrictions. The following guidelines will help alleviate issues and mitigate risks:

1. Prepare for the fabrication process ahead of designing:
  - (a) Survey of the full range of benefits provided by AM to know all available options. In particular, hollow internal volumes or lattices are unique solutions provided by AM for high heat flux applications

- (b) Trade study of the above benefits over constraints specific to AM (Conner et al., 2014) (restricted range of materials and their properties, residual stresses, rough imprecise internal features, support lattices which must be removed, etc.)
  - (c) Survey of available printer sizes, accuracies, powder sizes, and post-print processes including their associated risks. Current powder bed build plates are limited to 11 x 11 inches (280 x 280 mm) and may require fabrication at an angle (increasing costs) or a split into several parts.
  - (d) Selection of a CAD software adequate for new complex parts enabled by AM, with topology optimization if relevant (Liu et al., 2016).
2. Avoid severe distortions and residual stresses by minimizing the sintered area in each layer. This can be achieved with strategic orientation of the part on the printing plate, hollow volumes, or a split into several parts.
  3. Avoid rounded overhangs (e.g. for cooling channels), especially with diameters outside the 0.06 in. - 0.13 in. (1.5 – 3.3 mm) range. Build angular overhangs instead, inclined by more than 45 degrees relative to the horizontal plane.
  4. Take into account laser burns and powder evacuation when designing parts with an internal flow rate requirement by maximizing the cross-sectional area or adding powder escape routes.
  5. Regarding internal cooling, consider channel geometries unconventional for machining such as rhombi or shells. In the latter case, a range of lattice geometries is available to provide additional properties to the shell, e.g. structural strength. The benefits of lattices may however be outweighed by excessive pressure drops, in particular when combined with turns in the channel path, and difficulty removing the residual powder. Shell geometries often require guide walls to force the coolant into sides and corners.
  6. For geometries specified with tolerances, add excess material to account for printing distortions and errors. Subsequently post-machine them down to specifications.

7. Orient the part for printing with the surfaces to be machined closest to the printer referential/build plate. Else define a new referential for machining in order to account for distortions during the build.

## 1.5 Conclusion

Hypersonic air-breathing propulsion ground testing capabilities are extended by the use of additive manufacturing in the UVaSCF to enable the study of high-speed flameholders at the scale of DNS. AM allows for the novel transformation of the original direct-connect flowpath into a flowpath enabling semi-free jet testing for high-speed combustion. The first published methodology for the design and fabrication of additively manufactured scramjet combustor components is presented and experimentally validated in the UVaSCF. Recommendations for future designs to be additively manufactured are provided.

In essence, a host flowpath is developed for an immersed model with a small cavity flameholder. The mid-duct immersed model creates new boundary-conditions and includes a small-scale cavity to enable the first studies of high-speed flameholders with DNS and other well-validated CFD approaches. The resulting tunnel blockage and thermal loads are addressed with the use of contoured wall geometries and active convective cooling. Several design iterations stemmed from an inter-disciplinary collaboration including CFD, FEA, and in-situ testing. An iterative design process was conducted until the new parts could sustain an ethylene flame for repeated extended cycles lasting up to an hour. The final design consists of an Inconel 718 shell of 0.05 in. (1.27 mm) thickness with internal cooling loops running an ethylene-glycol solution throughout the flameholder. The design is modular for operational flexibility and efficient fabrication. Repeated tests in the tunnel demonstrated that the concept met, or exceeded, design requirements: low tunnel blockage, resistance to cycles of thermal loads and structural stresses, ignition and flameholding, as well as access for optical and sensors-based diagnostics. To the author's knowledge, this experiment constitutes the longest test duration for an additively manufactured cavity flameholder under a flame in real high-speed flow conditions.

In the next chapters, the characterization of the inflow boundary-conditions and the cavity flow with PIV is presented. These will be used to prescribe inflow boundary conditions to the DNS computation, which will yield the temporarily and spatially resolved flame structure. Based on these results, appropriate sub-models for LES will be implemented. The fourth iteration with a machined cavity-side geometry was also recently experimentally validated in the UVaSCF. In the longer term, the current hardware enables the integration of virtually any immersed model into the

flowpath by replacing the flameholder with a new design on the strut.



## Chapter 2

# High-Resolution PIV Capability for High-Speed High-Enthalpy Flows

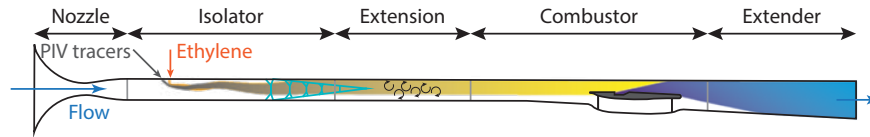


Figure 2.1: Schematic of the facility flow path with the small-scale cavity flameholder identifying important flow features.

## 2.1 Introduction

### 2.1.1 Motivation and research question

Steady, efficient combustion in high-speed flow is a necessary condition for ramjets and dual-mode scramjets. Hydrocarbon fuels are prime candidates due to their ease of storage and handling. In these engines, the residence time of hydrocarbon fuel molecules is however shorter than their characteristic reaction time, requiring the use of fuel/air premixing and a cavity flameholder (Ben-Yakar and Hanson, 2001; Gruber et al., 2018). Radical species needed for flame anchoring are generated in the cavity, which is sized for a sufficiently-long molecular residence time. Stabilization of the flame reaction front is thus controlled by an intricate coupling of shear flow dynamics, turbulence-chemistry interactions, and mass exchange between the main flow and the cavity flow. These complex flow physics span a wide range of length and time scales, requiring high-resolution experimental measurement techniques and numerical prediction tools. Current capabilities are limited to about 1 mm, i.e. the upper range of the turbulent spatio-temporal spectra, i.e. integral scales and larger intermediate scales, resulting in varied accuracy of the numerical tools and the need for new experimental data.

To address this, high-resolution Direct Numerical Simulations (DNS, Rauch et al. (2018)) are applied to the high enthalpy flow of the University of Virginia Supersonic Combustion Facility (UVaSCF) to better understand the dynamics of cavity-stabilized, high-speed flames. An immersed small-scale cavity flameholder for scramjet flows was designed to render DNS computation times feasible (Lieber et al., 2018b). The UVaSCF is an electrically-heated, long-duration wind tunnel generating a Mach 2 flow with a total temperature of 1200 K and a total pressure of 300 kPa. These conditions simulate a flight Mach number of 5 and an altitude of approximately 20 km (Krauss and McDaniel, 1992; McDaniel et al., 2005). Figure 2.1 illustrates the new flowpath configuration.

DNS simulations can resolve all flow scales, from the largest integral scales  $\mathcal{O}(10)$  mm down to

the smallest Kolmogorov micro-scales  $o(10) \mu\text{m}$ . In order to reproduce the flow of experiments, these numerical simulations need accurate boundary-conditions including the gas mixture composition and velocimetry. NO-mixing PLIF measurements by (Cantu et al., 2016a, Figure 5, p. 378) characterize fuel premixing and show on average a homogeneous concentration over the half duct height for a single-sided injection with the shock train upstream. One other key input for DNS is high-resolution velocimetry. In particular, the turbulence characteristics of the incoming flow are to be captured over the widest possible range of the turbulence spatial spectrum. The goal of the present work is to quantify with the highest feasible resolution the mean profile and turbulence characteristics at the upstream boundary of the domain of interest, i.e. immediately upstream of the insert and cavity leading edges. These characteristics will be compared at a later point against DNS-generated boundary-conditions in order to assess their conformity to the experimental flow.

Increasing the spatial resolution of PIV over previous measurements, however, conflicts with trade-offs imposed by the harsh environment encountered in the UVaSCF combustor, e.g. high seed densities, localized seeding (potentially causing measurement bias in mixed regions), and low magnifications. Achieving the above goal therefore requires the investigation of novel methodologies and digital signal processing filters. Uncertainties will be estimated as comprehensively as possible to enhance the reliability of comparisons between simulations and experimental data. The principle of PIV and its application to high-speed flows will be presented next, before a survey of previous work illustrating state-of-the-art capabilities and a statement of objectives.

### 2.1.2 Flow velocimetry in high-speed flows

An array of velocimetry techniques has been developed to diagnose flows, Each technique has its set of advantages and disadvantages that first must be carefully considered. The extreme speeds, temperatures, and sensitivity to disturbances of the present flow prevent the use of intrusive techniques, e.g. probes such as hot wires (Tropea et al., 2007), due to survivability and flowfield disturbances. Optical velocimetry methods are, in contrast, non-intrusive. These include Laser Doppler Anemometry (LDA, Petrie et al. (1986)), and Doppler Global Velocimetry (DGV, Fischer (2017); Meyers (1995)), Molecular Tagging Velocimetry (MTV, Gendrich et al. (1997)), Particle Tracking Velocimetry (PTV, Schanz et al. (2016)), Laser Speckle Velocimetry (LSV), and Particle Image Velocimetry (PIV, Raffel et al. (2007)). PTV enables very high spatial resolutions by tracking

individual particles rather than an ensemble (Schanz et al., 2016). However, PTV requires excellent signal quality, a series of more than two images or pre-processing with PIV, and controlled low seeding densities. These conditions are impossible to achieve in the present flow with current capabilities. Another arising technique in the field of flow velocimetry is optical flow velocimetry based on the principle of pixel brightness conservancy (Horn and Schunck, 1981). Recent work (Schmidt and Sutton, 2018) demonstrated this technique on PIV image pairs with a density of one velocity vector per pixel. However the technique is still in its early development stage and requires further characterization and guidelines before advanced applications. It also remains highly sensitive to signal disturbances present in the UVaSCF flow (varying particle seeding density and luminosity, strong divergence, gas density gradients) and requires low pixel displacements (e.g. 3 px in Schmidt and Sutton (2018)), which significantly clips the wide dynamic range of velocities found in cavity flows. The extreme conditions of the present high enthalpy, high speed flow make Particle Image Velocimetry (PIV) particularly adequate to resolve it non-intrusively, in multiple spatial dimensions, and to build large samples over time (Raffel et al., 2007; Westerweel et al., 2013).

PIV is however a complex technique inherently relying on significant signal processing and with limitations. Its fundamental principle of cross-correlating two consecutively-acquired images to derive the motion of a particle group is based on key assumptions including homogeneous particle size, density, and brightness; a small proportion of particle loss of pairs; small but  $\gtrsim 2$  px particle image diameters; and low background noise. Departures from these conditions can generate significant random and systematic errors. Finite discretization of the flow motion in time and space mean that the output velocity vectors constitute the temporal mean of the flow motion between the two laser pulses and the spatial mean of the flow domain within the interrogation window (IW). Hence while the spatial density of the vector field depends on the IW overlap, the velocimetry spatial resolution is only dependent on the IW size and the imaging scale factor. For example, a 50% overlap for 48 px IW yields a density of 1 vector every 24 px; however, the cross-correlation method does not resolve flow structures below 48 px and hence the velocimetry resolution remains 48 px. Hence scaling and timing must be astutely adjusted to minimally trim the broad spatial spectra of high-speed, high-enthalpy turbulent flows.

Extensive PIV work has been conducted in compressible and thermally-convective flows with a selection of publications listed in table 2.1. Issues specific to these flows for optical velocimetry

were reported early on in the literature. In particular, optical distortions from density gradients, velocity gradients, and weak signal-to-noise ratios have been reported. Spatial resolutions have been kept at  $\sim 1$  mm to maintain feasibility, with a few exceptions reaching 0.5 mm, and seeding was often contained to the boundary-layer or core flow to avoid window fouling — potentially causing measurement bias in global statistics. High resolution PIV has also remained a challenge for these flows due to hardware limitations stemming from cameras and optics, e.g. the sensor pixel size and the laser timing limits, relative to the flow temporal and length scales. Early digital PIV studies include Urban and Mungal (2001) who measured turbulent mixing layers with a resolution of  $\sim 1$  mm. Scarano and Oudheusden (2003) investigated the compressible flow in the wake of a blunt base in a Mach 2 supersonic flow. They used interrogation window deformations and multi-grid methods to improve the spatial resolution to  $420 \mu\text{m}$ , resolving a wider range of spatial scales. Williams and Smits (2012) applied PIV to measure turbulence within the boundary layer of a Mach 7.4 flow. The authors reached resolutions down to  $480 \mu\text{m}$  and noted the presence of large density and velocity gradients, which reduced seeding uniformity and skewed the correlation peaks. Higher resolutions have been achieved for PIV in high-temperature reacting flows with an open test section and low velocities. For example, Foley et al. (2015) applied PIV on shear layer stabilized flame with a preheat temperature set at 533 K and a bulk flow velocity of 35 m/s. The spatial resolution was  $\sim 220 \mu\text{m}$  in-plane with a laser sheet thickness of  $\sim 1$  mm in thickness.

Scramjet combustor flows are characterized by high enthalpies, high speeds, and high turbulence intensities, adding significant challenges to the application of PIV. These flows are also usually contained within a metallic duct. Weisgerber et al. (2001) reported PIV and LDV measurements in a Mach 2 supersonic flow and highlighted the sensitivity of these measurements to the tracers. The PIV resolution was reported to be 0.5 mm/vector. Goyne et al. (2001) obtained early PIV in a scramjet combustor. A hydrogen fuel jet was seeded with  $0.3 \mu\text{m}$  alumina powder and injected into a Mach 2 flow with a total temperature of 1200 K. The velocimetry resolution was 1.2 mm in-plane and  $800 \mu\text{m}$  in depth. In a subsequent study, Scheel (2004) used 12 nm Aerosil R812 tracers (a  $\text{SiO}_2$ -based particle) to compare flameholding performance of scramjet fuel injector geometries with a  $200 \mu\text{m}$ -thick laser sheet and a  $31 \mu\text{m}/\text{pixel}$  resolution. Stereoscopic PIV was first applied in a scramjet combustor flow by Smith (2011), who measured the two counter-rotating vortices that are induced by the ramp fuel injector. The laser sheet in these experiment was

particularly thick to resolve the third component at 2.6 mm, while the in-plane resolution was 1 mm. Relatively lower resolutions are also found when adding the third physical dimension with e.g. tomography PIV (Dominik and Noel, 2016; Weinkauff et al., 2013). Rice (2014) extended the application of SPIV to the dual-mode combustion regime, finding that the average velocity fields compared within 10% difference to hybrid LES/RANS predictions downstream. RMS velocities were however over-predicted. The discrepancy in RMS velocities between experiments and simulations was confirmed by CARS measurements which indicated an over-reactive mechanism in the CFD. Inaccurate turbulence modeling in the LES was identified as its cause, highlighting the need for accurate boundary-conditions from PIV. Tuttle et al. (2014) applied PIV to a hydrocarbon-fueled supersonic reacting flow in a cavity flameholder and in the nearby freestream. These authors observed significant out-of-plane motion from pathline convergence/divergence in the cavity but not in the freestream. Using spherical  $\text{TiO}_2$  particles and short combustion runs of 30 seconds each, they alleviated severe window obscuration and achieved a velocimetry spatial resolution of 1.81 mm in-plane and 0.5 mm in depth. Kirik et al. (2014) and Peltier and Carter (2015) applied PIV to a scramjet cavity flameholder to investigate the effects of inlet distortion. The spatial resolution was  $\sim 1$  mm in all dimensions. Previous in-house work by Kirik et al. (2017) achieved PIV in the reacting cavity flow of a dual-mode scramjet by using graphite nanoflakes as tracers. These tracers alleviate window fouling observed with other types of particles. While the laser sheet was 0.3 mm thick, the in-plane velocimetry resolution was 1 mm, clipping the turbulent kinetic energy spectrum near the integral length scales. In addition, seeding density was kept very high to avoid spurious vectors at the cost of higher uncertainties from broader correlation peaks. The present work builds upon the solution of graphite nanoflakes to improve the resolution and accuracy of PIV in high-enthalpy ducted flows.

### 2.1.3 Objectives and Contributions

Enabling high-resolution PIV in high enthalpy, high speed, and high turbulence intensity flows requires a careful study of the setup and measurement signal to maintain velocimetry with minimal bias errors. The measurement conditions in this work are exceptionally harsh. Table 2.2 lists key flow characteristics for the test cases of table 1.3, estimated from previous work and CFD studies (Kirik, 2017; Nielsen et al., 2018; Ramesh et al., 2018). The disturbances induced by the present

high-speed, high-temperature flow on the above characteristics accumulate with disturbances from imaging at high resolutions as well as in a small ducted metal test section. The first part of the present work is therefore a trade-off study for a high-resolution setup satisfying PIV guidelines for dual-mode scramjet flows.

Second, signal disturbances occurring at higher resolutions are analyzed and addressed with a documented methodology minimizing or avoiding them. The development and demonstration of a novel pre-processing filter enabling PIV on images with strong particle intensity variations, e.g. flakes or laser sheets, to enable the recovery of lost signal and the removal of systematic errors is documented. Finally, detailed *a posteriori* uncertainties are computed in order to quantify the precision, enhance the resolution, and enable thorough comparisons of measurements. This chapter has three objectives: design the PIV measurement technique and conduct a trade study in order to improve the spatial resolution and to explore limitations of high-resolution PIV in a scramjet combustor; explore and implement approaches to improve the quality of the PIV to minimize experimental uncertainties; and quantitatively estimate *a posteriori* cross-correlation errors and propagate them into uncertainties for turbulence statistics.

The chapter is structured as follows. In the first part, the setup and its optimization are presented, including the timing and imaging setup, and the PIV post-processing routines. In the second part, images acquired from tunnel runs are assessed for their quality, and the sources of signal disturbances are identified. Third, results on both synthetic PIV and real measurements using the above methodology are analyzed and compared against a conventional approach. The computation of uncertainties is described. Finally, a summary is presented in the conclusion. This study represents the highest resolution velocimetry available thus far in a high-speed compressible environment, at  $355\ \mu\text{m}$ , allowing the broader capture of the spatial turbulent kinetic energy spectrum to prescribe accurate CFD boundary-conditions.

Table 2.1: Key past 2D-2C PIV work in high-speed flows

Paper	In-plane PIV resolution	Laser sheet thickness	Tracer
Urban and Mungal (2001)	$\sim 1$ mm	Unknown	15 mm $\text{TiO}_2$
Weisgerber et al. (2001)	0.5 mm	12 nm Aerosil R812	
Goyne et al. (2001)	1.2 mm	800 $\mu\text{m}$	0.3 $\mu\text{m}$ $\text{Al}_2\text{O}_3$
Scarano and Oudheusden (2003)	420 $\mu\text{m}$ estimated	500 $\mu\text{m}$	27 mm $\text{TiO}_2$
Scheel (2004)	1 mm estimated	200 $\mu\text{m}$	12 nm Aerosil R812
Wagner et al. (2010)	1.78 mm	1.4 mm	0.02 $\mu\text{m}$ Evonik P25 $\text{TiO}_2$
Tuttle et al. (2014)	1.81 mm	0.5 mm	100 mm $\text{TiO}_2$
Kirik et al. (2014) and Peltier and Carter (2015)	0.96 mm	1 mm	
Williams and Smits (2012)	Kirik et al. (2017)	1 mm	0.3 mm
Williams and Smits (2012)	480 $\mu\text{m}$	Unknown	100 mm $\text{TiO}_2$

Table 2.2: Key flow characteristics for the present measurements representing operation at the maximum fuel equivalence ratio  $\Phi_g = 0.47 \pm 0.03$ .

Mach number [-]	0.66
Total temperature [K]	1200
In-plane $U_{AVG}$ [m/s]	$\sim 350$
In-plane $U_{RMS}$ [m/s]	$\sim 50$
Out-of-plane $\bar{U}$ [m/s]	$\sim 6$
Out-of-plane $U_{RMS}$ [m/s]	$\sim 40$

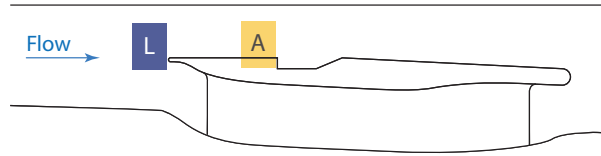


Figure 2.2: Fields of views of the present work up to scale relative to the model insert.

## 2.2 Experimental setup

The available hardware is described in this section along with a method to identify an adequate set of setup parameters for high-resolution PIV. The objective is to measure key turbulence statistics including the velocity mean and root-mean-square in the fields of views (FOV) L and A (figure 3.1), i.e. immediately upstream of the leading edge and of the cavity, at the highest resolution feasible. These fields of view define the boundary-conditions for the accompanying numerical work (Nielsen et al., 2018; Rauch et al., 2018)).

### 2.2.1 Summary and hardware specifications

The test section and flameholder model are summarized first and described in greater details in Lieber et al. (2018b) . The test section is a  $\sim 1.5 * 1.5$  in<sup>2</sup> rectangular duct with the flameholder set halfway into the freestream as shown in figure 2.1. Ethylene is injected as a 90° cross-flow jet in the isolator, upstream of a shock train promoting efficient mixing and decreasing the flow to subsonic speeds. Results in this chapter have been acquired at a global fuel equivalence ratio of  $\Phi_g = 0.47 \pm 0.03$  (6.6%) and a Mach number of 0.66 corresponding to case 1 of tables 1.2 and 1.3 .

The PIV system described below consists of a seeder with graphite nanoflakes, a laser, one camera, and LaVision’s data acquisition hardware and software. A 500 mJ/pulse, double-cavity Spectra Physics PIV-400 Nd:YAG laser delivers two pulses at  $\lambda_{Laser} = 532$  nm, separated by a set time interval  $\Delta t$  of 300 ns and at a repetition frequency of 10 Hz. 95% of the energy is dumped using beam splitters to maintain the fluence at the downstream mirrors and model below the damage threshold. The beams are transformed by cylindrical telescoping optics into a laser sheet of constant height  $\sim 25$  mm and converging thickness. The latter is characterized with a 2D beamprofiler at a FWHM of  $\sim 140$   $\mu$ m at its focus and a depth of focus — i.e. a  $\sqrt{2}$ -factor increase of its waist — of 6 mm. The laser sheet is inserted into the test section through a fused silica window, is co-planar with

the tunnel center plane, and its focus coincides with the center of the imaging field of view. Graphite nanoflakes of mean length  $1.1 \mu\text{m}$  and thickness  $16 \text{ nm}$  (Kirik et al., 2015) are levitated in a fluidized bed seeder (Howison and Goyne, 2010) and injected at 35 psi above tunnel pressure in the isolator, upstream of the fuel injectors and on the centerline. The cross-flow jet penetrates approximately halfway into the duct and is thoroughly mixed with the freestream by turbulent convection amplified by the isolator shock train. One LaVision Imager Pro X 2M CCD 14-bits camera captures the illuminated particles. Due to the camera rotation by  $4^\circ$  about the tunnel streamwise axis, reflections off the model metal surfaces are clipped by the model edge. A Scheimpflug lens adapter rotates the focal plane back to coplanar with the laser sheet. The camera's  $1600 \times 1200$  array of  $L_{Pixel} = 7.4 \mu\text{m}$  square pixels is 55% quantum efficient at 532 nm. A Micro-Nikkor 105mm f/2.8 lens set at a magnification  $m = 1 : 1$  and an aperture of f/8 images the measurement volume through the test section's 9.5 mm-thick planar fused silica window. A  $532 \pm 10 \text{ nm}$ -wide bandpass filter mounted on the lens alleviates spurious light from e.g. radiation or combustion. The imaging system is calibrated using a pinhole mathematical model with first-order radial distortions and a dotted grid of  $125 \mu\text{m}$  discs separated by  $250 \mu\text{m}$ . The following below further detail the setup and the tradeoffs stemming from high-resolution PIV in a high-speed high-temperature environment.

### 2.2.2 Tracer properties and seeding

Kirik et al. (2017) demonstrated PIV of a cavity flameholder in dual-mode scramjet conditions using graphite nano-flake tracers. The latter prevent window fouling over other typical PIV tracer materials ( $\text{Al}_2\text{O}_3$ ,  $\text{TiO}_2$ ,  $\text{SiO}_2$ , Chen and Liu (2018); Melling (1997)), which suppressed optical access, through a combination of lower adhesion rates and combustion in stagnant areas. The flakes flow tracking ability is predicted adequate from theoretical analysis using its Stokes number (Kirik et al., 2015). An experimental demonstration of their flow tracking capabilities may be found in appendix 3.6. The flake nature of the tracers is necessary due to unavailability of spherical graphite particles with adequate Stokes numbers. Diffraction-limited imaging leads to particle images in the form of Airy disks on the camera sensor, which approximate as Gaussians and thus are cross-correlated identically to spherical particles. Tracers seeding is particularly difficult for nano-particles in a high-enthalpy tunnel and in particular in the free stream. In this work, a fluidized bed seeder (Howison and Goyne, 2010) suspends 50-100 mL of particles from a porous

plug. Agglomerates breakup is promoted by using ultrasonic and turbine vibrators but remain unavoidable. Pulsing the air supply is necessary to achieve seeding duration exceeding 10 s at the cost of constant density through time. In addition, the seeder supply pressure not only impacts the bed fluidization but also the jet penetration depth in the tunnel. Good seeding is achieved at 3.4 atm, at which the cross-flow jet penetrates up to halfway into the duct to seed the entire measurement domain (figure 2.1). Mixing across the streamtube of interest occurs mostly through turbulent convection generated by the isolator shock train. Overall, uniform seeding density and mono-disparity requirements are not met in the measurement domain and further stress the need for *a posteriori* error estimates.

### 2.2.3 Laser timing and sheet characteristics

A 10 Hz double-cavity Nd:YAG laser able to deliver two 500 mJ, 532 nm pulses is used for tracers illumination. Nano-graphite flakes require substantial amounts of energy for acceptable signal levels due to their small size and low reflectance. As a result, background noise from laser reflections off the metal duct walls is significant and must be taken into account during post-processing. Inter-pulse timing is adjusted to capture independent velocimetry samples as follows. Turbulence time scales are estimated on the order of 1  $\mu$ s. These time scales are to be much lower than the interval between velocimetry samples in order to ensure statistical independence, and greater than the inter-frame time  $\Delta t$  in order to approximate the frozen flow hypothesis.  $\Delta t = 300$  ns satisfies this criterion while allowing particle displacements  $\mathcal{O}(1)$  px for the minimum velocities. Laser sheet formation is addressed next. High-resolution PIV, in addition to achieving high in-plane resolutions, implies the highest possible resolution normal to the plane, i.e. a thin laser sheet. Indeed, as the sheet is made thicker, the resulting velocimetry corresponds to a broader average across the sheet cross-section. A minimum thickness is however to be maintained to sustain dense particle images and minimize particles loss of pairs. Consequently, a trade-off in laser sheet thickness is found at four times the maximum cross-plane displacement (Keane and Adrian, 1990; Nobach and Bodenschatz, 2009; Tropea et al., 2007) or 103  $\mu$ m. A telescope of equivalent focal length  $f_{LS} = 600$  mm creates the converging laser sheet with its beam waist at the camera's FOV center. The beam waist thickness is measured before each experiment using an optics train consisting of a glass beam splitter and neutral density filters directly imaging the laser sheet onto a CCD sensor at the plane of focus. Figure 2.3

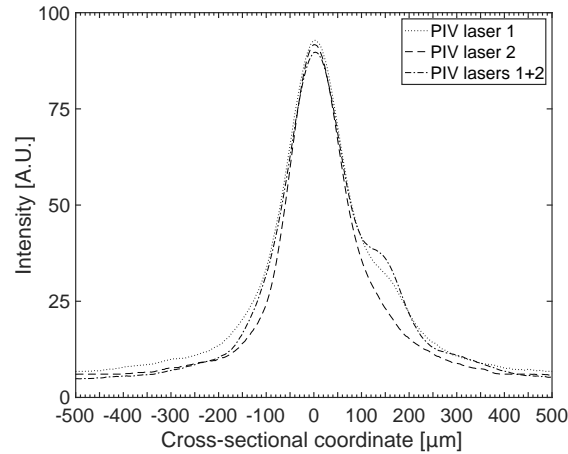


Figure 2.3: Laser sheets cross-sectional intensity profiles.

shows the cross-sectional intensity profile of the dual-cavity laser sheets, showing Gaussian profiles with a FWHM of 150 and 135  $\mu\text{m}$  for laser 1 and 2 respectively. An asymmetry on the right side of the laser 1 profile however increases the relative width, causing systematic loss of pairs. The beam 50 mm depth of focus being much larger than the 12 mm-long FOV, the laser sheet thickness is approximated as constant.

#### 2.2.4 Imaging setup optimization

Due to the combination of geometrical particle images smaller than 1 px, the flow high velocities, and the high imaging magnification, the setup must be carefully designed in order to achieve good signal to noise ratios. A theoretical model is built to identify adequate sets of setup parameters for particle images between 2.5 and 3.5 px and to assess the signal sensitivity to these parameters. Inputs are representative of the real experimental conditions.

##### Theoretical model

A mathematical model specific to the present test conditions was designed to output an array of PIV imaging setups satisfying all constraints. Inputs are collected from experimental and CFD results as well as manufacturers. The model enables anticipation of departures from ideal PIV conditions and defines a solution space using application-specific constraints as well as guidelines found in

the literature, including Westerweel (1997), Raffel et al. (2007), Scarano (2013), Sciacchitano et al. (2015), and Tropea et al. (2007).

The following challenges were identified as primordial for the present application:

- The geometrical particle size is  $\ll 1$  px;
- A very wide dynamic range of speeds and strong gradients:
  - from  $\sim 600$  m/s in the freestream down to  $\sim -100$  m/s in the cavity over a shear layer a few millimeters thick;
  - with azimuthal fluctuations of  $\sim 10$  m/s in the smallest eddies of diameter  $\sim 100$   $\mu\text{m}$  (estimates based on results from Naka et al. (2016));
  - causing particle image distortions due to density variations;
- A very wide range of length scales from integral length scales on the order of millimeters down to Kolmogorov length scales  $\sim 10$   $\mu\text{m}$  (Kirik, 2017).

## Inputs

The simulation uses the above setup characteristics in addition to:

- a range of magnifications  $m$ ,
- a range of depths of measurement volume  $D_z$ , equal in practice to the laser sheet Full Width Half Maximum (FWHM), and
- a set of numerical apertures  $N$

to generate a three-dimensional matrix of parameter combinations representing all possible setups.

The flow is then modeled with the reference velocities given in table 2.2 based on previous measurements Kirik et al. (2017) and numerical simulations Nielsen et al. (2018). The maximum displacement is estimated with  $U_{max} = U_{AVG} + 3 \cdot U_{RMS}$ . The minimum displacement would be the azimuthal displacement of the finest eddies found in the flow. Tanahashi et al. (1997), Tanahashi et al. (2004), and Naka et al. (2016) investigated these structures both numerically and experimentally. Fine scale structures are universal in turbulence due to their unity Reynolds number

Table 2.3: Inputs for the theoretical model described in section 2.2.4 to identify enhanced setups.

Magnifications $m$ [-]	0.5 - 1 x
Depth of Measurement Volume $D_z$ [mm]	0 - 0.5
f-numbers $N$ [-]	{5.6; 8; 11; 16}
In-plane $U_{AVG}$ [m/s]	350
In-plane $U_{RMS}$ [m/s]	50
Out-of-plane $\bar{U}$ [m/s]	6
Out-of-plane $U_{RMS}$ [m/s]	40

and take the form of coherent tube-like eddies. Key findings include the fine eddy diameter and the azimuthal velocity being  $d_\theta = 8\eta_K$  and  $u_\theta = 1.5u_K$ , respectively and approximately. In this application, while  $u_\theta = 12$  m/s corresponds to a detectable displacement of 0.7 px,  $d_\theta \sim 80 \mu\text{m}$  is well below the achievable velocimetry resolution. Hence  $d_\theta$  is much too small for current PIV capabilities and the turbulence spatial spectrum must necessarily be clipped at high wave numbers.

### Computations and filtering

The imaging magnification and aperture is found based on the predicted particle image size, both at the center and at the edges of the laser sheet cross-section. Diffraction, smearing, and focusing blur are taken into account in the  $d_p$  calculation. Criteria for the rejection of parameters combinations are based on literature guidelines found in Keane and Adrian (1990); Raffel et al. (2007); Scarano (2013); Sciacchitano et al. (2015); Tropea et al. (2007); Westerweel (1997) including:

- a minimum particle image diameter  $d_p$  of 2.5 px and a maximum of 4 px, based on the most suitable diameter of slightly more than 2 px for a Gaussian fit error of  $< .01$  px;
- a maximum streak length of 1 px;
- and a maximum first-pass IW size of 128x128 px combined with a maximum particle displacement of 25% of the IW.

The geometrical particle image dimensions are the graphite flakes dimensions projected onto the sensor without any imaging effects except magnification. For an imaging magnification of 1:1, the geometrical particle image is 0.15 px in length and 0.002 px in thickness. To keep estimates conservative,  $d_{Geom} = 0.002$  px in the following. Sub-pixel particle sizes cause peak-locking, i.e. skew the pixel displacement distribution towards integer values, since conditions for sub-pixel Gaussian

interpolation are not met (Tropea et al., 2007). As a result, peak-locking causes large systematic errors. Diffraction and blur can however be astutely used to increase the required particle image diameter  $d_p$ .

The following imaging effects are quantified in terms of equivalent diameters and combined with  $d_{Geom}$  into  $d_p$ :

**Diffraction spot** For a combination of an aperture  $N$  and a magnification  $m$ , the diffraction spot diameter is estimated as

$$d_{Diff} = 2.44 \cdot \lambda_{Laser} \cdot N \cdot (1 + m). \quad (2.1)$$

**Blur circle** The blur circle is estimated at the edges of the measurement volume along its depth dimension  $Z$  with

$$d_{Blur} = D_z/2 \cdot f_C^2 / (f_C/m + f_C)^2 / N, \quad (2.2)$$

where  $f_C$  is the focal length of the camera lens.

**Streak** The streak drawn by a particle during the duration of one laser pulse is calculated with

$$L_{Streak} = U_{max} \cdot \delta t \cdot m. \quad (2.3)$$

**Particle image diameter** The above is combined into two extrema for the particle image diameter,  $d_{p,focus}$  at the focal plane and  $d_{p,edge}$  at the measurement volume edge, using the Euclidean norm

$$d_{p,focus} = \sqrt{d_{Geom}^2 + d_{Diff}^2 + L_{Streak}^2}; \quad (2.4)$$

$$d_{p,edge} = \sqrt{d_{p,focus}^2 + d_{Blur}^2}. \quad (2.5)$$

Finally,  $d_p$  in pixels is computed for each term as:

$$d_p^* = d_p / L_{Pixel}. \quad (2.6)$$

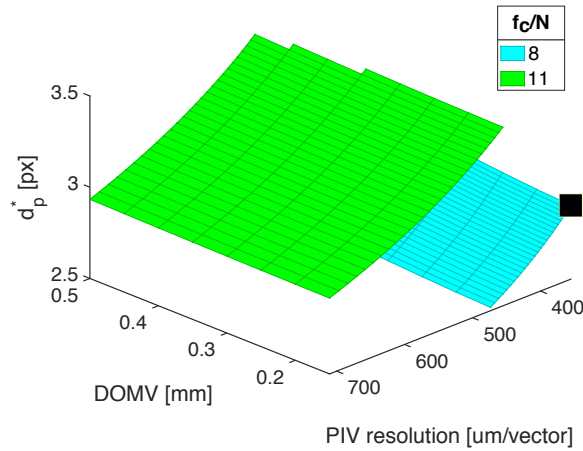


Figure 2.4: Solution space for PIV setups in the UVaSCF flow. The chosen solution is the highlighted vortex.

## Outputs

The developed Matlab model creates three-dimensional solution spaces for  $d_{p,focus}^*$  and  $d_{p,edge}^*$ . Both are tested for the rejection criteria listed in section 2.2.4. Input combinations failing the test are removed.  $d_{p,edge}^*$  is subsequently plotted as a function of the f-number  $N$ , the velocimetry resolution — directly related to the imaging magnification by  $L_{IW} * L_{Pixel}/m$  where  $L_{IW} = 48$  px is the IW length — and the Depth Of Measurement Volume (DOMV), as shown in figure 2.4. Experiments demonstrate excellent agreement between the model’s predictions and measurements. While the DOMV doesn’t significantly affect the particle image diameter, an increase in aperture or resolution display a non-linear relationship with the particle image diameter. A most suitable set of setup parameters is chosen by the user taking into account the gradients and offsets of the surface plots. Results in this chapter used the data point highlighted in figure 2.4 as a compromise between a high PIV resolution corresponding to a magnification of 1:1 and a particle size less than 3 px. The chose setup f-number is 8, the DOMV=  $150 \mu\text{m}$ , and the PIV resolution is =  $355 \mu\text{m}/\text{vector}$ , resulting in  $d_p^* = 2.9$  px

Magnifications greater than 1:1 are possible with extension tubes or long-distance microscopes. However tests at  $m = 1 : 1$  revealed additional disturbances occurring when magnification is increased, including locally streaked and out-of-focus particle images. Similar effects were observed in compressible or thermally-convective flows by Tuttle et al. (2014). These phenomena have no

Table 2.4: Relevant setup characteristics for the present high-resolution PIV experiments.

Reproduction ratio $R$ [-]	1:1
Scale factor [px/mm]	135.1
Scheimpflug angle [deg]	5
FOV length - X-axis [mm]	11.8
FOV length - Y-axis [mm]	8.9
Maximum displacement [px]	15.2
First pass IW size [px]	128x128
Last pass IW size [px]	48x48
Velocimetry resolution [ $\mu\text{m}$ ]	355.2
Streak size [px]	0.7
Velocity resolution <sup>1</sup> [m/s]	2.5
$d_{p,edge}^*$ [px]	2.90
DOMV [ $\mu\text{m}$ ]	150

correlation in time nor uniformity in space. Some frames are also completely in focus with no streak. In addition, pairs of frames always look very similar. It is therefore proposed that these effects are due to randomly-distributed, convected flow structures causing a lensing effect leading to the out-of-focus blur, or a dynamic ray deviation tracing a streak onto the camera sensor. These disturbances are hypothesized to distort the propagation of both the laser sheet and the light reflected off of the particles. The low angular displacement of the light rays would only be detectable at high magnifications. In effect, this artificially increases the particle image diameter  $d_p^*$  along one axis or radially. The uncertainty resulting from a larger particle image diameter can be captured by the *a posteriori* technique described in section 2.4. Disturbances at  $m = 1 : 1$  are considered acceptable but it was decided not to further increase the magnification to limit the severity of this effect.

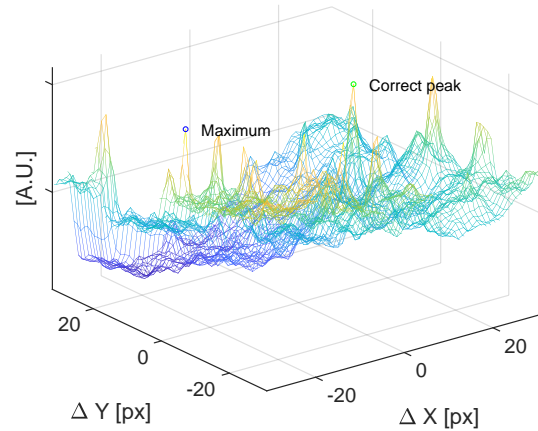


Figure 2.5: Signal of a common PIV pair of frames acquired in the flow of table 2.2 and in region L of figure 3.1. The correct displacement is  $\Delta X = 13.5$  px and  $\Delta Y = 1.5$  px.

## 2.3 Signal enhancement

Once the PIV measurements have been acquired with the setup described in section 2.2, the signal is pre- and post-processed with software in an attempt to compensate for hardware and environmental shortcomings still preventing reliable velocimetry.

### 2.3.1 Raw signal quality assessment

Despite the high quality setup presented above, the raw signal out of the camera does not satisfy the criteria for high quality PIV signals listed in section 2.1.2. Figure 2.5 shows a cross-correlation map from PIV signal acquired upstream of the model insert leading edge. The presence of many spurious peaks in the cross-correlation map and their low amplitude raise the concern for bias errors in the form of spurious vectors, as exemplified in the example cross-correlation map where the maximum value doesn't match the correct displacement. Spurious vectors can be filtered out with e.g. a median filter but only if they locally constitute a minority. Due to the large number of spurious vector, a solution involving pre-filtering the raw signal is necessary as described further in this chapter .

A close-up view of a typical pair of frames in figures 2.6a and 2.6b displays the intensity sub-range below 1000 pxcounts. The FOV histogram is shown in figure 2.6c. A wide dynamic range is observable, ranging from  $\sim 100$  pxcounts to saturation (16,383 pxcounts). This wide dynamic range is present across the entire image, ranging from dim particles (region 1 of frame 1)

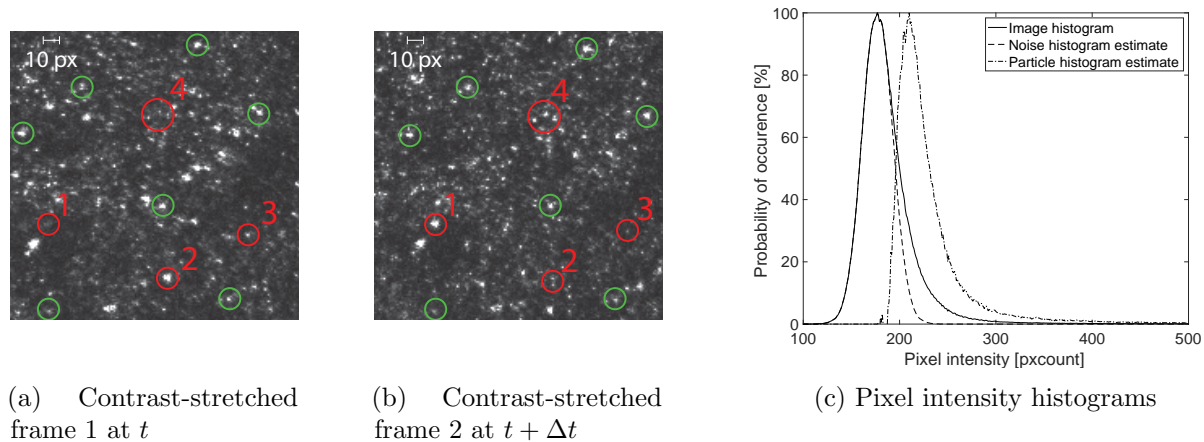


Figure 2.6: Raw PIV frames.

to saturated particles or agglomerates (region 2 of frame 1). The particle signal is also overlapped with background noise. The histogram of figure 2.6c displays a distribution with a single peak and high kurtosis indicating low signal-to-noise ratio likely due to a combined small particle size (Dellenback et al., 2000) and high background noise from the nearby metallic duct. This is verified assuming a Gaussian background noise distribution (Masullo and Theunissen, 2017; Westerweel, 2000) peaking at the histogram maximum. One may then separate the histogram into background noise and particles signal as in figure 2.6c. Under these assumptions, the background noise intensity profile is characterized as a Gaussian curve with  $\mu_{noise} = 177$  pxcounts and  $\sigma_{noise} = 16$  pxcounts, overlapping with the particle signals peaking at 210 pxcounts.

Seeding is determined as uniform on average based on the homogeneous standard deviation of pixel intensities across the FOV. Mixing is however highly unsteady and images may have areas with little to no particle present while others reach a saturated pixel density. Instantaneous seeding inhomogeneities have a direct effect on bias and random errors. In particular, the cross-correlation uncertainty becomes specific to each interrogation window, stressing the need for *a posteriori* uncertainty quantification described in section 2.4.

Strong variations in particle luminosity, both in space and time, are also observed and constitute another source of cross-correlation noise. Brightness changes can be explained by the use of flakes to track the flow. While the use of graphite particles re-established optical access, flakes add three rotational degrees of freedom relative to spherical particles. The amount of scattered light for a fixed source and observer is thus dependent on the particle angle. The angular frequency is likely higher

than the inter-frame frequency due to the highly turbulent flow. In turn, the intensity of the same particle may strongly vary between frames, typically by 600%. Particles across the FOV display this behavior (particles circled in red in figure 2.6). Other particles show the expected behavior in PIV, i.e. identical brightness (circled in green in figure 2.6). The particle labeled 1 changes from dark to very bright, opposite to particle 2. Particle 3 undergoes a smaller change in intensity. A group of particles in region 4 all undergo a large intensity variation between frames. While in- and out-of-plane motion explains these intensity variations to some extent, their significant proportion in areas of denser seeding and in very thick laser sheets point to additional causes. Moreover, the hypothesis of a large discrepancy in laser sheet overlap is ruled out based on beam profiles, from which overlap is verified with an accuracy of  $\sim 10 \mu\text{m}$  before and after every experiment. It is therefore suggested that the flake nature of the tracers cause these abrupt intensity variations. The intensity of light reflection off a flake being dependent on the flake orientation in space, should the particle rotate between frames, the intensity varies accordingly. Whether the drop or increase in intensity is caused by in- and out-of-plane motion, poor laser sheet overlap for dual-cavity lasers, or change in particle reflectance due to tumbling, the effect of intensity variations in the raw signal is investigated next with synthetic PIV.

### 2.3.2 Diagnosis with synthetic PIV

Synthetic PIV signals are first generated with parameters representative of real measurements and allow to gain control over all signal parameters. The diagnosis of the root cause of the signal noise observed in figure 2.5 is presented next, before designing filters to address it and enable high first-to-second peak ratios in cross-correlation maps.

#### Setup

A 128x128 px canvas is populated with 30 synthetic particle images randomly distributed across. The particle locations, intensities, and diameters are also randomly distributed. Particles are simulated as Gaussians of FWHM itself distributed as a Gaussian distribution ( $\mu_{FWHM} = 2 \text{ px}$  and  $\sigma_{FWHM} = 0.85 \text{ px}$ ). Particle intensities also follow a Gaussian distribution with ( $\mu_{intensity} = 750 \text{ pxcounts}$  and  $\sigma_{intensity} = 200 \text{ pxcounts}$ ). A set proportion of these particles are simulated with an intensity amplitude change of 600% between frames, either as an increase or decrease. This

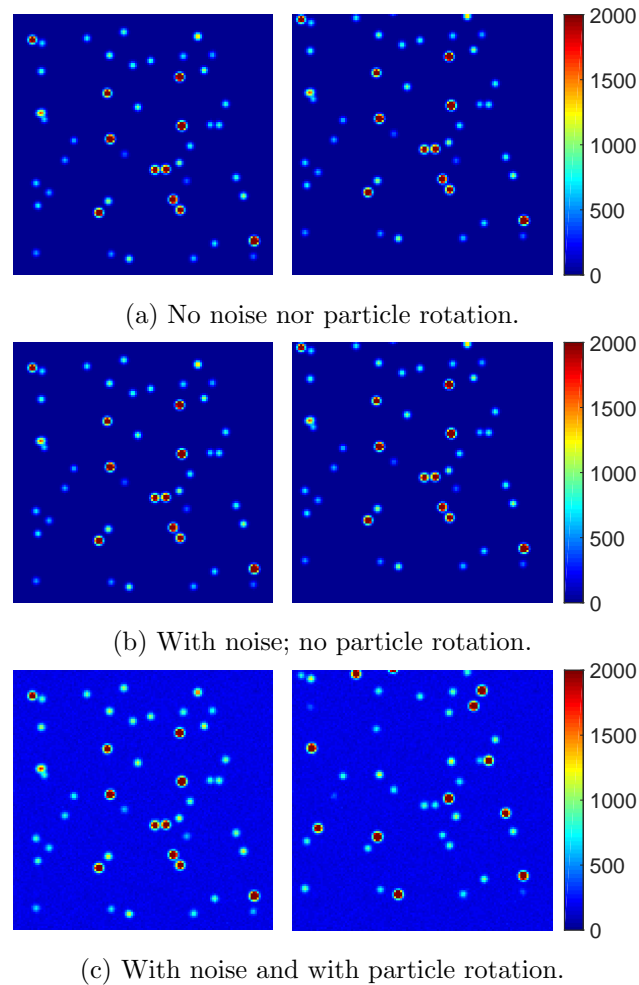


Figure 2.7: Synthetic 14-bit PIV image pairs for the three simulation cases described in section 2.3.2.

models the intensity changes observed in section 2.3.1 and likely caused by the nanoflakes rotation. Additive Gaussian noise is simulated with parameters  $\mu_{noise} = 185$  pxcounts and  $\sigma_{noise} = 19$  pxcounts. Finally, a set proportion of particles will disappear and contribute to particles loss-of-pairs. Figure 2.7 shows the input images for 75% of particles experiencing an intensity amplitude change between frames and 10% affected by loss-of-pairs. All parameters are representative of the real signal acquired in this work, however the latter is significantly heterogeneous due to seeding. These synthetic PIV images are used next to diagnose the root cause behind the multiple peaks seen in the cross-correlation maps.

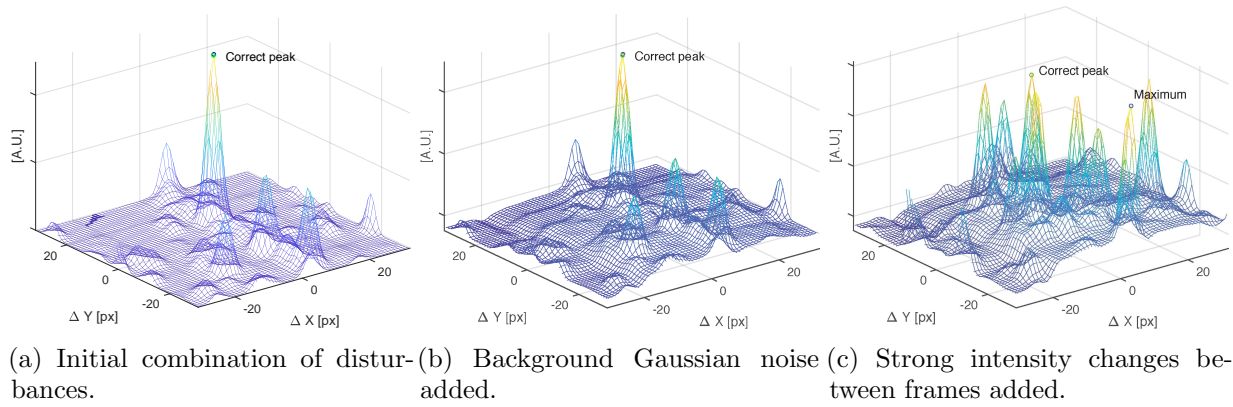


Figure 2.8: Cross-correlation maps for one identical set of particles with three different combinations of signal disturbances.

### Diagnosis of the noise root-cause

Figure 2.8 displays the cross-correlation maps sharing the same synthetic set of particles and uniform motion ( $\Delta x = 5$  px,  $\Delta y = 10$  px) but having different combinations of disturbances. The maximum peak and the correct peak are highlighted in each map. These cross-correlations are repeated over 2,500 samples and the proportion of matching maxima and correct peaks is measured for each case.

The first map (figure 2.8a) corresponds to a signal with relatively minimal disturbances, i.e. 50% of particles are 600% brighter than the initial Gaussian distribution due to forward-facing flakes and 10% are lost in one of the two frames (particles entering and exiting the laser sheet). Despite these disturbances, the local maximum corresponds to the correct displacement and the resulting vector is correct. Note that the peak has a finite width and is surrounded by small peaks due to partial overlap between the two frames at displacement values other than the correct displacement. In figure 2.8b, background Gaussian noise is added relative to figure 2.8a, peaking at 25% of the mean particle intensity. The base is now lifted above 0 and the peak broadened, which decreases the peak correlation value. The correct peak remains however unambiguously selected. Observations from the experimental data of figure 2.5 are reproduced when the bright particles (with intensities 600% brighter than their attributed value from the initial Gaussian distribution) undergo an intensity variation between frames. This phenomenon would occur when the nanoflakes would rotate between frames. The corresponding correlation map is shown in figure 2.8c. The addition of intensity variations either lead to the selection of the wrong peak, as in figure 2.8c, or low first-to-second peak ratios, causing low confidence in the velocimetry. In conclusion, the primary source of spurious peaks

in cross-correlation maps for the present test conditions is identified as strong particle intensity variations between pairs. It is suggested that the most likely causes for the latter are:

1. Flakes rotation;
2. Partial particle loss-of-pairs (i.e. the particle remains visible but dim);
3. Laser beam steering by density gradients;
4. Agglomerate break-up;
5. Misalignment between the laser sheets and difference in beam divergence due to the use of a double-cavity laser.

Nobach and Bodenschatz (2009) studied the effect of individual particle image intensity variations between two consecutive frames, however with lower amplitudes. These authors concluded that the phenomenon introduced an additional error in displacement estimates when particle images overlap, limiting accuracy to the order of 0.1 pixel. The particle number density was shown to have a negligible effect on the added error.

The root-cause for the large number of spurious peaks being identified, a newly-developed Logarithmic Contrast Stretch (LCS) filter applied to pixel intensities is demonstrated next to significantly decrease the spurious peaks amplitudes in cross-correlations.

### **2.3.3 Logarithmic Contrast Stretch filter design**

Following the above diagnosis that low signal-to-noise ratios in cross-correlation maps are caused by large intensity changes for a same particle between frames, signal pre-processing filters are tested on synthetic and recorded images. Improvement of PIV input signal using post-processing filters on the acquired data is common. For example, Theunissen et al. (2006) used adaptive PIV interrogation windows in a hypersonic flow to improve the resolution and decrease the signal-to-noise ratio. Dellenback et al. (2000) studied pre-processing filters on PIV images for contrast-enhancement, including direct transfer functions, histogram modification methods, and sharpening. In particular, these authors found that "the logarithmic transfer function enhanced the low-contrast edges of the histogram by expanding the gray scales there, provided a constant SNR, and transformed

multiplicative noise into additive noise.” This method significantly decreased the number of erroneous vectors for low seed densities by up to 60% for turbulent duct flows. As a result, the method provided desensitization of PIV to seed density, increasing the optimum seed density range by 5–30%. Masullo and Theunissen (2018) developed a MP-PIV (multiple peak PIV) method to resolve velocimetry when multiple peaks are present in the cross-correlation map due to strong velocity gradients. The authors noted that ”SNR is defined as the ratio between the highest and the second highest peak and can be indicative of measurement quality. However, a SNR below the threshold does not necessarily imply unreliable peaks. Multiple correlation peaks can be of equal height and well above the noise level.” The phenomenon observed in this work also incurs low signal-to-noise ratios and multiple peaks but due to strong intensity changes instead of velocity gradients or low contrast. The above methods are therefore not adequate. A methodology to extract the correct peak when significant particle image intensity variations are present is suggested next.

To address the observed large intensity changes, two approaches are considered: leveling all intensities above a given threshold, or compressing the dynamic range. PIV relies on the spatial information and the pixel intensities of the tracers to output the displacement. Hence clipping the histogram often leads to errors by changing spatial distributions from e.g. a Gaussian to a top-hat profile. The objective of the targeted filters is therefore to compress the upper dynamic range of images more than their lower dynamic range. The higher intensities correspond to particles, while the lower correspond to the background noise. Hence filters with a gradient  $do/di$  proportional to  $1/i^\alpha$  are tested, where  $o$  and  $i$  respectively correspond to the output and input pixel intensities, and  $\alpha$  is a constant.

Pre-processing transform filters with a gradient  $\propto 1/i^\alpha$  are therefore suggested here, in particular a Logarithm Contrast-Stretch (LCS) filter. It consists of passing the intensities of an image stack through a logarithm function and stretching their histogram across the full 16-bit range. In the case of high background noise, e.g. in a flame, the image can be normalized by the background noise prior to filtering; pixels equal or dimmer than the background would therefore have a nil output and will not contribute to the cross-correlation matrix. Background normalization is a tolerable histogram clipping since it does not significantly clip the particle signal itself. However, removing the background by subtraction or normalization alters the particle signal itself and should thus be avoided when the noise is tolerable, e.g. in the free stream vs. in a flame. Figure 2.9 displays

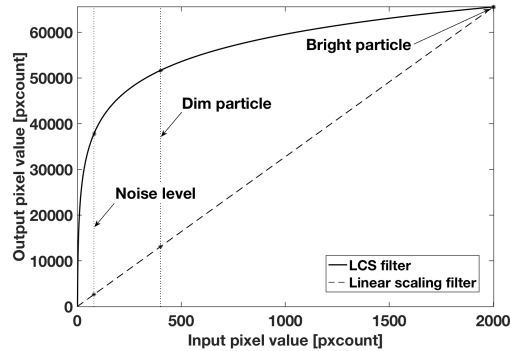


Figure 2.9: Logarithm-contrast-stretch (LCS) filter transform. (\*) Markers denote the intensities used in the example above.

the shape of the LCS filter relative to the input intensity. Its gradient  $\propto 1/i$  upscales the lower intensities (noise) less than medium intensities (dim particles), which themselves are less amplified than high-intensities (bright particles). Consider as a realistic example: a 2,000 pxcounts particle rotating into a 400 pxcounts image in the second PIV frame. The background noise is 80 pxcount. In the original image, the dim particle image is 80% darker than the bright image in the other frame, and the background is 80% darker than the dim particle image. In the LCS-filtered image, the dim particle is only 27% darker than its bright counter-part. The background noise is however also only 37% darker than the dim particle image. Despite amplifying background noise, the LCS filter transform improves PIV processing since random background noise has a weaker — and most importantly quantifiable *a posteriori* — effect on the cross-correlation error as demonstrated in section 2.3.2. The LCS filter is demonstrated in section 2.5 on both synthetic PIV and real measurements. It is shown to produce the best results on the present signal relative to other filters with a  $\propto 1/i^\alpha$  gradient.

#### 2.3.4 Cross-correlation and vectors post-processing

Once processed with the LCS filter, a pair of frames goes through a multi-pass cross-correlation process iteratively using 128 x 128 px interrogation windows down to 48 x 48 px windows. Below this size, uncertainties significantly increase and the number of vectors after post-processing decreases. A 75% IW overlap in the final passes minimizes truncation errors. The first-pass interrogation windows are weighted by an elliptical Gaussian with its major axis along the streamwise component; subsequent passes use automatically-deformed interrogation windows to account for gradients in

the flow (Scarano, 2002; Scarano and Oudheusden, 2003). An array of post-processing filters is applied to remove spurious vectors. The quality of the final dataset is assessed through the dominance of the correct peak in the cross-correlation map and the complete removal of spurious vectors as indicated by the temporal distribution of velocities and their random uncertainties: the velocity distribution is expected to approximate a normal distribution and uncertainties a log-normal distribution (Sciacchitano and Wieneke, 2016). The temporal mean and Root Mean Square (RMS) are then outputted at each vector location. The RMS vectors are separated into flow fluctuations and random errors as discussed in section 2.4. The former is retained as  $u_{RMS}$  and its uncertainty is updated following the method of Sciacchitano and Wieneke (2016).

## 2.4 Signal Uncertainties

Finally, uncertainties were computed in order to quantify the measurement precision and accuracy, to balance the velocimetry resolution versus reliability, and to enable thorough comparison studies between different flows. Uncertainties of the hardware are combined for each vector with *a posteriori* cross-correlation error estimates, based on the correlation statistics method developed by Wieneke (2015). The latter relies solely on the source PIV images to output an error estimate using a statistical analysis of the correlation map itself. The detected errors contain residuals from the calibration, seeding-related errors (density, particle shape, size, intensity), the background noise, in- and out-of-plane motion, and particle disparity from fluctuations within the interrogation window. Sciacchitano et al. (2015) compares the correlation statistics method to other *a posteriori* error quantification methods and measured its accuracy to exceed all others at over 85% of the correct RMS value corresponding to the above-listed errors. The uncertainty maps generated by the correlation statistics method are propagated to statistical quantities assuming uncorrelated variables. A 95% confidence interval is then provided by multiplying the random component of the standard deviation by the factor 1.96. This corresponds to a 95% likelihood that the considered statistical quantity falls within  $\pm 1.96 * \sigma_{error}$ . This assumes normal distributions visually checked for each data sets.

### 2.4.1 Sources of Uncertainties and Signal Noise

#### **Conventional methods and recent improvements for instantaneous random errors quantification**

Uncertainty estimates have been proven difficult to assess in PIV due to its long chain of processes, the signal discretization in time and space, and its inherent multi-dimensionality. From the real flow motion to the computation of the instantaneous vectors to the statistical quantities of interest, dozens of elementary computations occur based on assumptions. Extensive care in setting up experiments (section 2.2) cannot always prevent the signal being subject to an array of disturbances accumulating into both significant systematic and random errors. PIV uncertainties have typically been estimated using a reference numerical simulation, values from the literature, or the parallel use of a second setup (Sciacchitano et al., 2015; Tuttle et al., 2014; Wagner et al., 2010; Westerweel,

1997). PIV uncertainty quantification methods were however recently made available (Sciacchitano et al., 2015) and the correlation statistics method of Wieneke (2015) — implemented in the LaVision software DaVis 8 — is used in the present work. This method accounts for the random errors contained in the image, stemming from e.g. Gaussian noise, particle image size and density, as well as in- and out-of-plane motion. It does not account for systematic or bias errors, including timing errors, calibration errors, turbulence spectrum clipping, strong velocity gradients, particle slip, and statistical convergence. Some of the latter are addressed next and combined with the random uncertainties. The final output should be interpreted as a lower bound of the real uncertainty due to the assumptions and non-quantifiable errors described in the following.

### **Turbulent Kinetic Energy spectrum clipping**

One objective is to minimize Turbulent Kinetic Energy (TKE) spectrum clipping. Previous work (Kirik, 2017) estimated the tunnel's Kolmogorov temporal frequency at  $f_K = 1/\tau_K = 500 \text{ kHz}$  and spatial frequency at  $\eta_K = 10 \text{ } \mu\text{m}^{-1}$ , where  $\tau_K$  and  $\eta_K$  are the Kolmogorov time and length scales respectively. In order to fully resolve the flow, the Nyquist-Shannon sampling theorem requires a temporal resolution of  $\nu_{req} = 2 * f_K = 1 \text{ MHz}$  and a spatial resolution of  $k_{req} = 2/\eta_K = 200 \text{ mm}^{-1}$ . These numbers far exceed the capabilities of the most advanced hardware available at the time of writing. Sutton (2013) reports currently achievable PIV resolutions with well-designed experiments of  $\gtrsim 250 \text{ } \mu\text{m}$ . The present experiments, pushing the limits in resolution of high-performance hardware, have a temporal resolution of  $\nu_{PIV} = 10 \text{ Hz}$  and  $k_{PIV} = 2 \text{ mm}^{-1}$ . This results in necessary clipping of the lower tail of the TKE spectrum, introducing an error in all statistics related to the flow fluctuations. This error cannot be quantified in our case due to non-isentropic, non-homogeneous turbulence.

### **Velocity gradients and particle slip**

Particle slip was extensively studied theoretically by Kirik et al. (2017) who used the same particles. These authors found an average aerodynamic slip uncertainty of 5.1E-5% of the mean velocity magnitude. The results of an experimental test on their flow tracking capability are presented in appendix 3.6. In addition, Samimy and Lele (1991) concluded that the RMS error stemming from

aerodynamic slip was less than 1% for  $St < 0.1$ , which is the case for nano-graphite particles. Hence particle slip is taken into account with a 1% bias error added to the RMS velocities.

### **Imaging distortions**

The residual error from image dewarping is propagated into statistical quantities as a systematic error. Density gradients in thin flow structures, facility windows, and along the laser beam path in the facility surroundings induce refraction index gradients and thus distort light propagation. This optically inhomogeneous medium results in virtual particle displacements, particle image blurring, and illumination plane deflection. The latter effects have been previously identified and studied by several authors (Elsinga et al., 2005a; Schlüßler et al., 2014; Tuttle et al., 2014). Elsinga et al. (2005b) performed a detailed analysis of aero-optical distortions in PIV, sorting them in three categories: particle image blur, position and velocity errors. The latter two lead to systematic errors while particle image blur decreases the SNR and broaden the correlation peak, leading to additional random errors. Since pairs of frames in this work always look similar, it is assumed that the refractive index is frozen over the inter-frame time interval  $\Delta t$ . Distortions hence may incur an increase in random and vector location uncertainties whereas uncertainties in velocity magnitudes and direction can be neglected. Random uncertainties from blurring can in turn be estimated using the software built-in method. Vector location shifts could be corrected with the information of density gradients across the FOV with e.g. simultaneous Schlieren measurements. However, their small apparent magnitude  $o(1)$  pixel relative to the interrogation window size of 48 px support the assumption of negligible effects on the velocimetry.

### **Change of relative intensity between particle images and LCS**

The change of relative intensity between particle images between the first and second exposure was demonstrated to be the source of large errors by Nobach and Bodenschatz (2009) in the case of overlapping particle images. In the present case, this phenomenon is worsened by large intensity variation amplitudes, incurring bias errors for all particle images. The LCS filter was demonstrated to reduce the occurrence of bias errors by amplifying the correct peak in the cross-correlation map in section 2.3.2. Spurious vectors will however remain and the remainder is removed using post cross-correlation filters.

### 2.4.2 RMS correction and uncertainties propagation

Uncertainties are combined using adequate propagation assumptions. The measured displacement RMS can then be corrected to separate the flow fluctuations from noise fluctuations according to Sciacchitano and Wieneke (2016):

$$u_{RMS,flow} = u_{RMS,total} - \sigma_{u,noise} \quad (2.7)$$

In the following, uncertainties are presented in the form of confidence intervals assuming normal distributions for the random errors. The confidence level is chosen at 95%, corresponding to  $\pm 1.96\sigma$  intervals. For example, a typical uncertainty for the streamwise mean is  $\pm 4$  m/s.

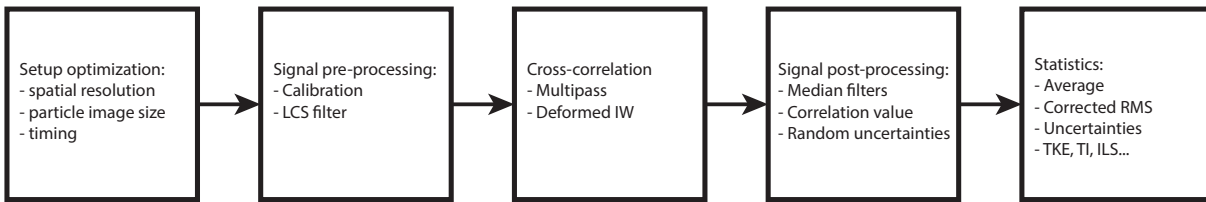


Figure 2.10: Setup design and processing steps for high-resolution PIV in a high-speed flow.

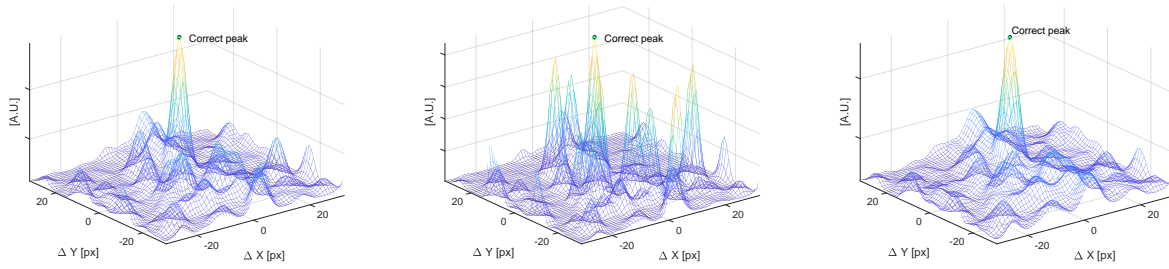
## 2.5 Discussion and recommendations for high-resolution velocimetry in high-speed combusting flows

The entire process described above, from the setup design to the final statistical fields, is summarized in figure 2.10. Results of this approach on both synthetic PIV and real measurements are presented in the following.

### 2.5.1 LCS results on synthetic PIV

The LCS filter effectiveness is illustrated with the cross-correlation map of figure 2.11a. This cross-correlation uses the same synthetic PIV images as the cross-correlation map of figure 2.8c. In this example, the use of the LCS filter successfully prevents the selection of a spurious peak. This is however at the cost of increased random errors stemming from peak broadening. Increased random errors are nonetheless much preferable to the bias error of a spurious vector and quantifiable with the correlation statistics method of Wieneke (2015).

An infinity of alternative functions with a gradient proportional to  $1/i^\alpha$  may be considered by varying the value of  $\alpha$ . Two alternative options are explored: a filter with gradient  $\propto 1/i^{0.5}$ , corresponding to a square-root function-based filter, and a filter with gradient  $\propto 1/i^2$ , corresponding to a negative inverse function-based filter. The  $1/i^{0.5}$ -gradient filter will induce a weaker compression of the dynamic range than the LCS filter, which enhances the signal in case of higher background noise but worsens it for identical or stronger particle intensity variations. On the other hand, the  $1/i^2$ -gradient filter will induce a greater compression of the signal dynamic range, which worsens the cross-correlation map in case of equal or higher background noise but enhances it for greater particle intensity variations. Tests run on synthetic PIV show that, for the present case, the LCS filter strikes a good balance between the two and outputs the highest number of correctly identified



(a) Logarithm contrast-stretch transform filter:  $o \propto \log_{10}(i)$  and  $\alpha = 1$  (b) Square-root contrast-stretch transform filter:  $o \propto \sqrt{i}$  and  $\alpha = 0.5$  (c) Negative inverse contrast-stretch filter:  $o \propto -\frac{1}{i}$  and  $\alpha = 2$

Figure 2.11: Performance comparison of pre-processing filters with a gradient  $\frac{do}{di} \propto \frac{1}{i^\alpha}$  for conditions identical to figure 2.8c, where  $o$  is the output pixel intensity,  $i$  the input pixel intensity, and  $\alpha$  a constant.

peaks. This is highly dependent on conditions including the seeding density, which in practice vary throughout an acquisition. Other inverse-gradient filters should therefore be considered for each specific application. As an example for a case representative of the present experimental conditions, the LCS filter applied to 2,500 image pairs led to 98.3% of correctly identified peaks while the square-root-based filter led to 97.5% of correct peaks, the negative inverse-based filter to 48.7% of correct peaks and cross-correlation without any pre-filtering led to 20.9% of correct peaks. Note that the correct peaks without pre-filtering still have very low peak ratio values, leading to unreliable velocimetry. These numbers highlight the need for LCS pre-filtering since commonly-used post-processing filters would likely fail to remove all spurious vectors. Indeed, considering the previous example, the peak ratio filters would only keep the 20.9% of correct peaks at best, leading to low sample sizes and low spatio-temporal signal continuity. Median filters would also fail to all remove spurious vectors given that 79.1% of the sample is erroneous. In contrast, LCS outputs 97.5% of correct peaks and the remaining 2.5% of spurious peaks can be filtered out using peak ratio and spatio-temporal median filters. The dramatic improvement in signal quality is demonstrated next on experimental datasets.

### 2.5.2 LCS results on real PIV measurements

The above observations from tests on synthetic PIV are confirmed by applying the LCS filter on experimental acquisitions. Figure 2.12 displays the correlation peak for the same image as in figure

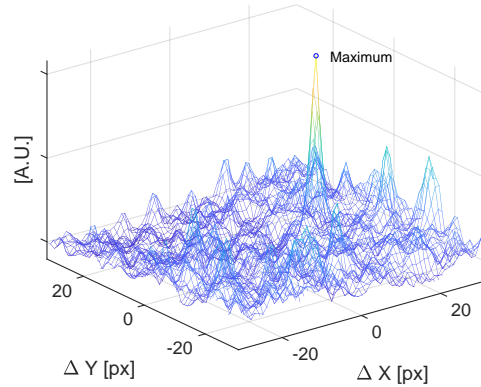


Figure 2.12: Cross-correlation map of the signal of a common PIV pair of frames (see figure 2.5) acquired from experiments in the flow of table 2.2 and in region L of figure 3.1.

2.5. The spurious peaks present in the unfiltered signal are all significantly decreased in amplitude and the correct peak stands out for its unambiguous selection by the algorithm. The width of the peak is again broadened from the greater influence of random background noise.

A stack of PIV image pairs acquired at a flow Mach number of  $M \sim 0.6$  and a global ethylene equivalence ratio of  $\Phi_g \sim 0.48$  is processed using the LCS filter and the operations chain of figure 2.10. The L FOV (figure 3.1) is located immediately upstream of the Insert Leading Edge (ILE) and above its Upstream Surface (US). The tunnel wall opposite to the flameholder is represented with the continuous line at  $Y/H = 4.8$ . A sub-sample of average velocity vectors are displayed with white arrows to show flow directionality. Streamlines in purple originate from each vector. The mean and RMS velocity fields are computed from the stack of instantaneous velocity fields and presented in figure 2.13. The velocimetry shows no evidence of bias errors: the mean and RMS distributions are continuous, display expected trends, and have similar values to comparable velocimetry (Kirik et al., 2017). The velocity streamwise-component profile in figure 3.2a, taken at a remote streamwise location from the leading edge, shows a thick boundary-layer extending down to the leading edge location. The average velocity fields of figures 3.2a and 3.2b show significant disturbance from the immersed model up to  $X/H \sim -11.5$ . The rounded leading edge creates a stagnation point immediately under the US y-location and diverts the incoming upward with transverse speeds up to  $\sim 60$  m/s. The Turbulence Intensity is in the range of 10.6 - 14.6 % with relative uncertainties of  $\sim 3\%$ , steadily decreasing across the boundary-layer. The turbulence intensity plotted in figure 2.13c shows a consistent trend with a fully developed pipe flow, steadily decreasing from higher

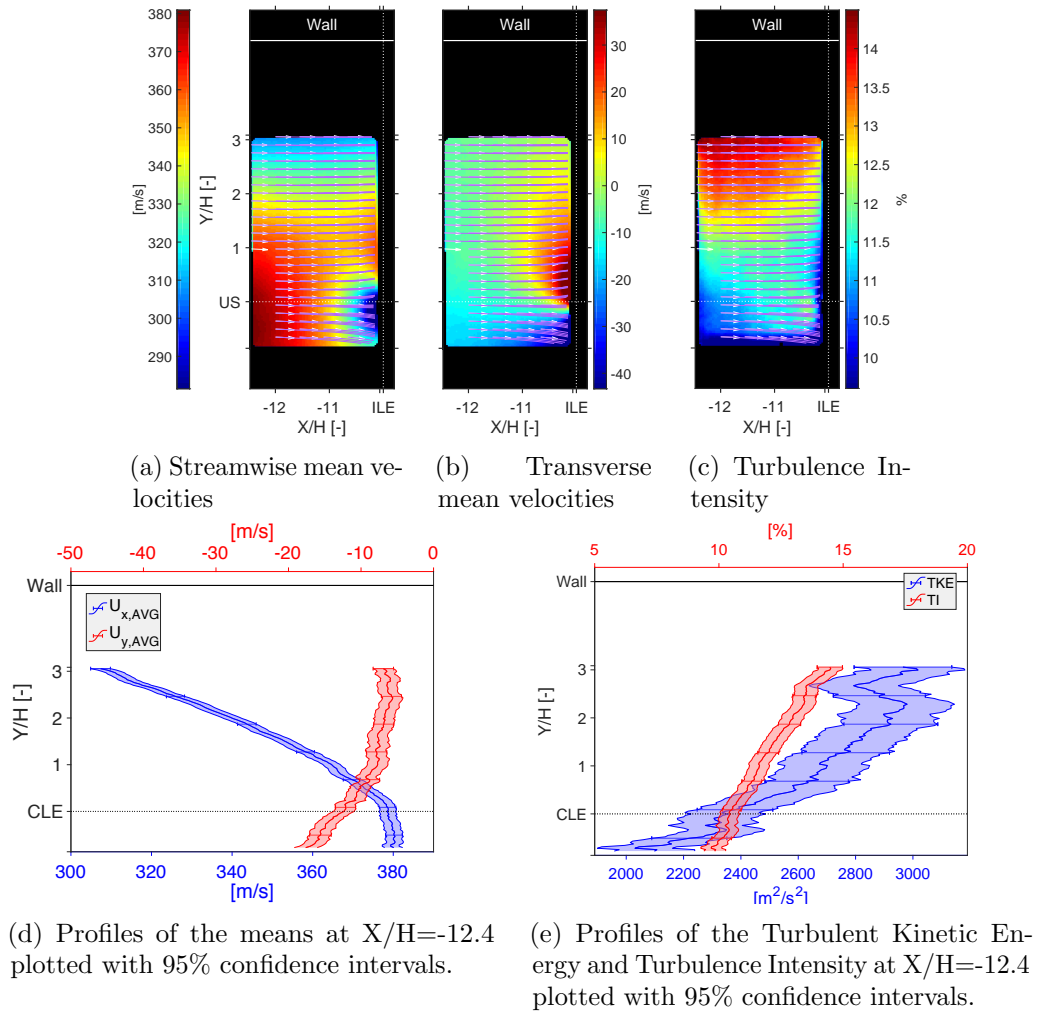


Figure 2.13: Velocimetry highlights for a flow Mach number of  $M \sim 0.6$  and a global ethylene equivalence ratio of  $\Phi_g \sim 0.48$  acquired immediately upstream of the model leading edge.

values near the wall down to the US and levels off to an approximately constant value of 10.7%. These trends and values provide the basis to validate the DNS simulations setup by comparing the coarsened DNS-generated boundary-conditions to fully characterized PIV results. Additional data and further analysis are provided in chapter 3.

## 2.6 Conclusion

A new methodology is presented to enable high-resolution PIV in high-speed high-enthalpy flows. These flows are particularly challenging due to an array of setup constraints and disturbances specific to compressible and thermally-convective flows. The approach is three-pronged: first a setup is designed using a theoretical model for trade-offs. Data acquired with this setup remains affected by strong disturbances that are addressed post-acquisition with software. In particular, a Logarithm Contrast-Stretch (LCS) filter is demonstrated as a novel application to PIV to decrease the amplitude of spurious peaks in cross-correlation maps. The origin of these spurious peaks is attributed to strong change in particle image intensity for the same particle between frames. Occurrence of this phenomenon is suggested to be primarily caused by the tracer flakes tumbling. In- and out-of-plane motion, laser sheet mismatch, light distortion by density gradients, and agglomerate break-ups are probable secondary causes. Finally, the velocimetry is characterized with an uncertainty analysis solely based on setup specifications and the acquired data. This approach is demonstrated to output reliable results with synthetic and experimental data at a  $355 \mu\text{m}$  velocimetry resolution. These results encourage further use of computing-intensive methods to extend the capabilities of PIV towards harsher flows.

Next is presented a detailed analysis of the velocimetry acquired before the insert and cavity flameholder leading edges using the methodology described in the present chapter.

## Chapter 3

# High-Resolution PIV for Characterization of the Inflow to a Cavity for High-Speed Flameholding

### 3.1 Introduction

The dynamics of cavity-stabilized, high-speed flames generate significant interest for the development of dual-mode scramjets. Hydrocarbon fuels are an attractive solution for these engines due to ease of handling and storage. The residence time of hydrocarbon fuel molecules in these engine is however small relative to their reaction time and must be extended using premixing and a cavity flameholder to enable flame anchoring (Ben-Yakar and Hanson, 2001; Gruber et al., 2018). Cavity-stabilized flames also enable the fundamental study of the physics governing compressible, premixed, and turbulent flames with a significant velocity component normal to the flame front.

The present work is part of a collaborative effort seeking deeper understanding of flow compressibility and heat release on turbulent flame structures with an array of experimental and numerical capabilities. The study leverages high-resolution diagnostics to capture a wider range of the turbulence spatial spectrum. Prediction tools and diagnostics include Direct Numerical Simulations (DNS, Rauch et al. (2018)), Large Eddy Simulations (Nielsen, 2019), Planar Laser-Induced Fluorescence (PLIF, Geipel et al. (2019)), Coherent Anti-Stokes Raman Spectroscopy (CARS), and Particle Image Velocimetry (PIV). While high-speed combustion has been extensively studied (Chen and Liu, 2018; Laurence et al., 2015; Le Pichon and Laverdant, 2016; Rockwell et al., 2014), cavity flameholders in high-speed flows have been the subject of fewer studies. The large geometrical scales employed so far prevent the DNS-modelling of the experimental flows. Tuttle et al. (2014) conducted an early study of these flameholders by applying PIV to a hydrocarbon-fueled ramped cavity in a supersonic flow as part of a multi-disciplinary AFRL research task to develop scramjet propulsion. The cavity used was 16.5 mm deep and 73 mm long. Kirik et al. (2014) and Peltier and Carter (2015) investigated with this same setup the effects of scramjet inlet distortion using PIV. In a subsequent study, Kirik et al. (2017) achieved PIV in the reacting flow of a dual-mode scramjet cavity. The latter was part of a collaborative effort combining an array of experimental and numerical diagnostics (Rockwell et al., 2017). The cavity was 9 mm deep and 54 mm long. The dimension of these cavities, and the cross-sectional area of the flowpath require DNS computational times exceeding current capabilities. In order to reach feasible DNS computational times, an immersed small-scale cavity flameholder for scramjet flows has been designed, additively manufactured, and tested in the University of Virginia Supersonic Combustion Facility (UVaSCF, McDaniel et al. (2005)). The cavity depth and length are

one third of the cavity presented in Rockwell et al. (2017), while the span was maintained to match the full tunnel flowpath width. The new cavity and flowpath are detailed in Lieber et al. (2018b).

This chapter has three objectives: to characterize the inflow to prescribe boundary-conditions for numerical models by measuring key flow statistics upstream of the flameholder insert and its cavity; to first characterize the inflow to an immersed model in a direct-connect facility converted to a semi-free jet rig and validate the flowpath design requirements described in chapter 1; and to determine trends when varying the shock train location and heat release with statistical models taking into account the estimator uncertainties. The present study provides 355  $\mu\text{m}$  resolution velocimetry, constituting the highest resolution velocimetry available yet in a high-speed compressible environment and enabling a broader capture of the spatial turbulence spectra to provide reasonably accurate turbulence intensity estimates. Turbulence intensity is a critical parameter that governs the propagation of the flame (Cantu et al., 2016a). In addition, the inflow to an immersed model in a direct-connect facility converted to a semi-free jet rig is studied for the first time and the first database for DNS modelling of a cavity flameholder is created.

The chapter is structured as follows. In the first part, the method and setup used are summarized. Results are then presented starting with the main case to be numerically simulated. This case sets the flow at a relatively low Mach number with a high equivalence ratio and is analyzed both at the insert and cavity leading edges. These measurements are then compared with other cases to investigate the effect of heat release and the shock train location. Finally, a summary is presented in the conclusion.

## 3.2 Method and Setup

The PIV setup and post-processing involved in the present chapter experiments are identical to those of chapter 2. Uncertainties will be additionally used in the following for thorough comparisons between cases using statistical tests. Details about the flowpath may be found in chapter 2. Cases referred to below are detailed in the test matrix of tables 1.2 and 1.3.

Measurements are acquired in the fields of views (FOV) immediately upstream of the leading edge and of the cavity (L and A of figure 3.1, respectively). These fields of view define the boundary-conditions for the accompanying numerical work (Nielsen et al. (2018), Rauch et al. (2018)).

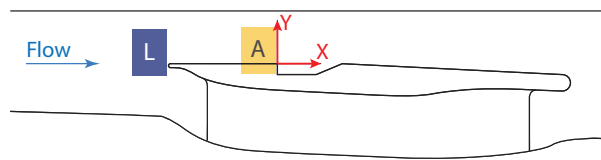


Figure 3.1: Insert close-up displaying the coordinate system and fields of views L and A.

In the calculation of the turbulent kinetic energy (TKE), the third Root-Mean-Square (RMS) component is assumed to be the average of the streamwise and transverse components. This is however a rough approximation since the flow is highly anisotropic. Parallel LES work has shown that the three-components turbulent intensity (TI) would increase  $o(1)$  % while the TKE would decrease  $o(100)$   $\text{m}^2/\text{s}^2$  (Nielsen, 2019).

### 3.3 PIV at the model leading edge

Velocimetry acquired in the tunnel freestream and upstream of an immersed model is presented for the first time. Data are acquired at a flow Mach number of  $M = 0.66$  and a global ethylene equivalence ratio of  $\Phi_g = 0.47 \pm 0.03$  corresponding to case 1 of table 1.2. The FOV is labelled L in figure 3.1, located immediately upstream of the Insert Leading Edge (ILE) and above the plane of the Cavity Leading Edge (CLE). In all figures, the tunnel wall opposite to the flameholder is represented with the continuous line at  $Y/H = 4.8$ , i.e.  $Y = 14.4$  mm, for scale. The ILE has a radius of 0.38 mm and its tip is located at  $Y/H = -0.13$ . The bounded areas in line plots represent the 95% confidence intervals. Temporal sample sizes are in excess of 2,000 counts. These measurements enable validation of flowpath design objective achievement (see chapter 1), including locally-contained leading edge disturbances to the main flow and smooth divergence of the lower streamtube under the insert. Taking into account the difference in measurement location in the UVaSCF combustor, all values presented below agree very well with previous data reported by Kirik (2017).

#### 3.3.1 Means

The mean velocity fields for each component  $x$  and  $y$  are presented in figure 3.2. Furthest upstream (figure 3.2c), the flow is characterized as a fully developed duct flow ( $Re_D \approx (10,000 - 100,000) \gg Re_{transition}$ , Schlichting and Gersten (2017)), with the opposite wall boundary-layer extending down to the ILE location corresponding to the mid-duct point. The streamwise mean velocity remains constant while the  $2.9^\circ$  divergence on the lower facility wall ( $Y/H \sim -4.8$ ) induces a negative transverse component  $\approx 1$  m/s. As the flow approaches the ILE starting  $X/H \sim -11$ , significant disturbance from the immersed model is encountered. The rounded leading edge creates a stagnation point at its tip and splits the flow into two streamtubes with transverse speeds of up to  $\pm 60$  m/s (figure 3.2d), corresponding to maximum local angular deviations of  $13^\circ$ . The change in sign of  $U_{y, AVG}$  occurs at the ILE tip location ( $Y/H = -0.13$ ). Streamlines depicted in continuous purple lines in figure 3.2a show no evidence of flow separation near the leading edge, validating a critical design requirement for the wall area relief.

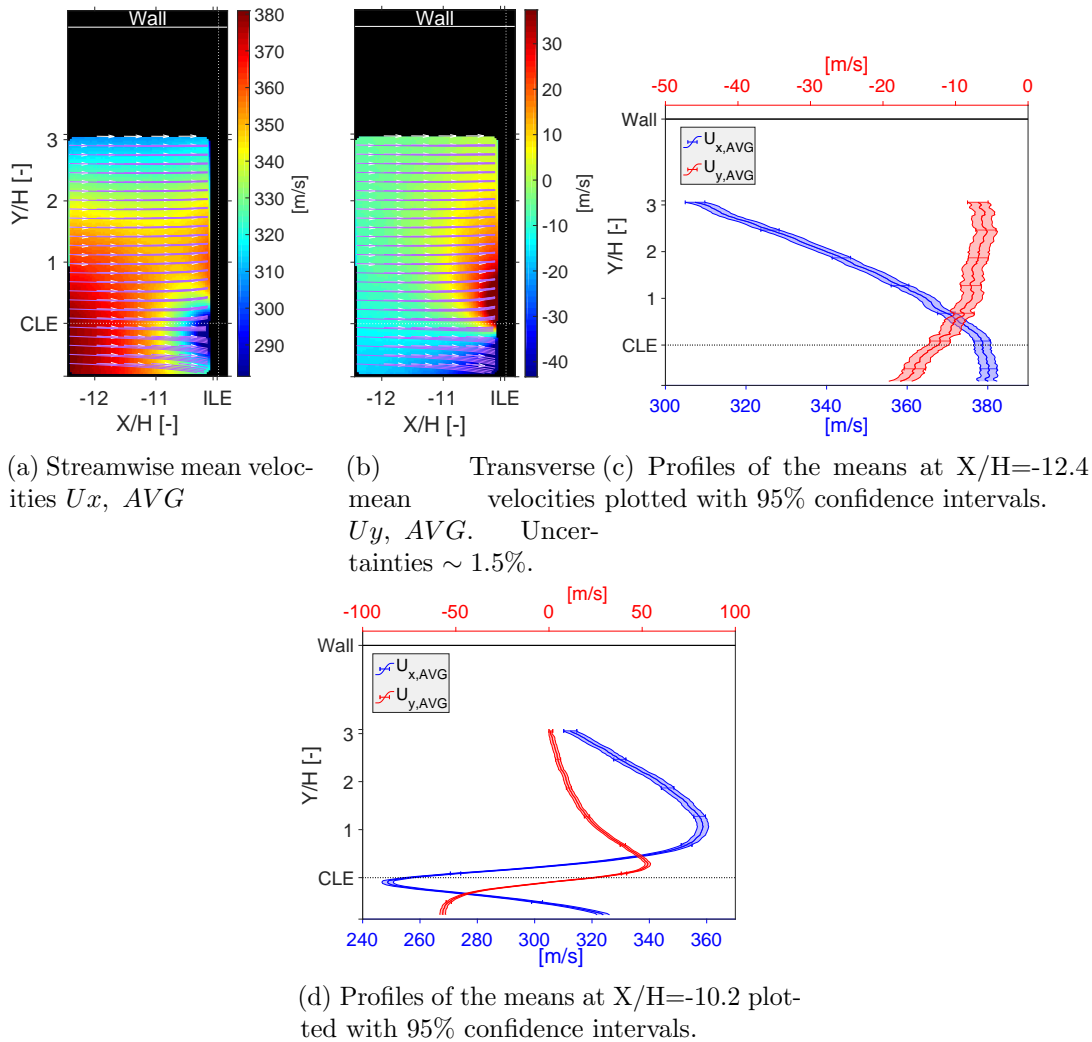


Figure 3.2: Mean velocimetry for a flow Mach number of  $M = 0.66$  and a global ethylene equivalence ratio of  $\Phi_g = 0.47$  acquired upstream of the flameholder insert.

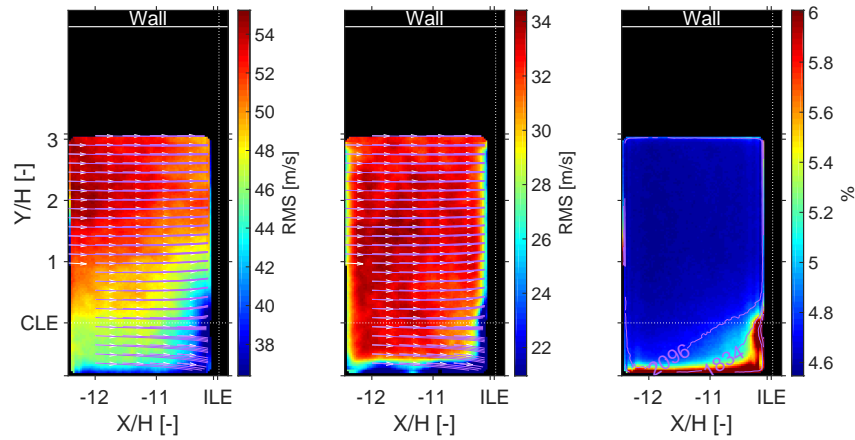
### 3.3.2 Root-Mean-Square velocities

RMS velocities are shown in figure 3.3. Figure 3.3c displays the uncertainties for the RMS corrected with the method of Sciacchitano and Wieneke (2016) and described in section 2.4. Overlaid is the contour plot of the sample size in purple. The sample size has a direct impact on the uncertainty of the RMS as well as the edges of the measurement domain, more significantly affected by loss-of-pairs and distortions. These causes are often combined and induce discrepancies in the RMS fields near the edges, which should be treated with caution for samples below  $\sim 2,100$  vectors where uncertainties may exceed 10%. Both the streamwise and transverse components remain constant along the x axis until  $X/H \sim -11$  (figure 3.3d), where the presence of the insert incurs a gradual

drop  $o(1)$  m/s. Anisotropy is demonstrated with the streamwise component of figure 3.3a 55 to 85% greater than the transverse component of figure 3.3b.  $U_{x, RMS}$  is also expected to be greater than  $U_{z, RMS}$ . Furthest upstream, the transverse RMS remains constant across the duct height at  $U_{y, RMS} \sim 30$  m/s while the streamwise RMS velocities decrease across the boundary layer from  $U_{x, RMS} \sim 55$  m/s to  $\sim 47$  m/s mid-duct. Overall, the RMS velocities of the streamtube captured by the insert, representing boundary conditions for numerical simulations, are unaffected by the insert presence upstream of  $X/H = -11$ . They are constant in space except for  $U_{x, RMS}$  along the  $y$  axis, which decreases with  $Y$ . Therefore, CFD domain boundaries for the inflow to the insert should be located upstream of  $X/H = -11$  and conditioned with anisotropic turbulence representative of a boundary-layer extending mid-duct.

### 3.3.3 Turbulent Kinetic Energy and Intensity

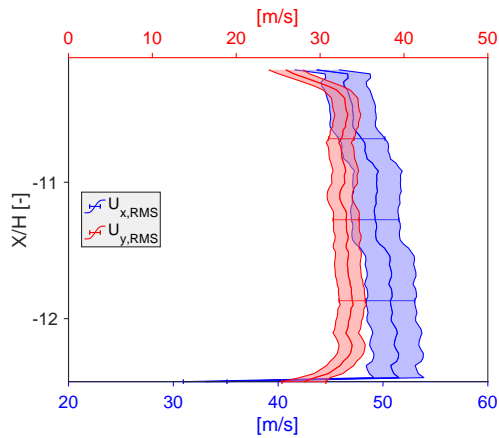
The TKE and TI plots are computed using the corrected RMS and mean velocities analyzed above and shown in figure 3.4 to prescribe CFD boundary conditions. The turbulence intensity lies in the range of 10.6 - 14.6 %, steadily decreasing across the boundary-layer, with relative uncertainties of  $\sim 3\%$ . The turbulent kinetic energy starts at a level of  $\sim 3,000$   $m^2/s^2$  before steadily decreasing down to  $Y/H = 0$ . Both the TI and TKE level off to an approximate constant value of 10.7 % and 2,500  $m^2/s^2$  respectively.



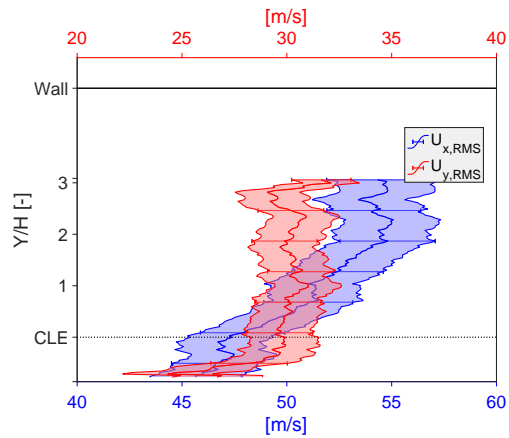
(a) Streamwise RMS velocities  $U_{x, RMS}$ . Uncertainties for a 95% confidence interval  $\in [1.2 - 2.2]$  m/s.

(b) Transverse RMS velocities  $U_{y, RMS}$ . Uncertainties for a 95% confidence interval  $\in [0.6 - 1.6]$  m/s

(c) Streamwise RMS uncertainties for a 95% confidence interval;

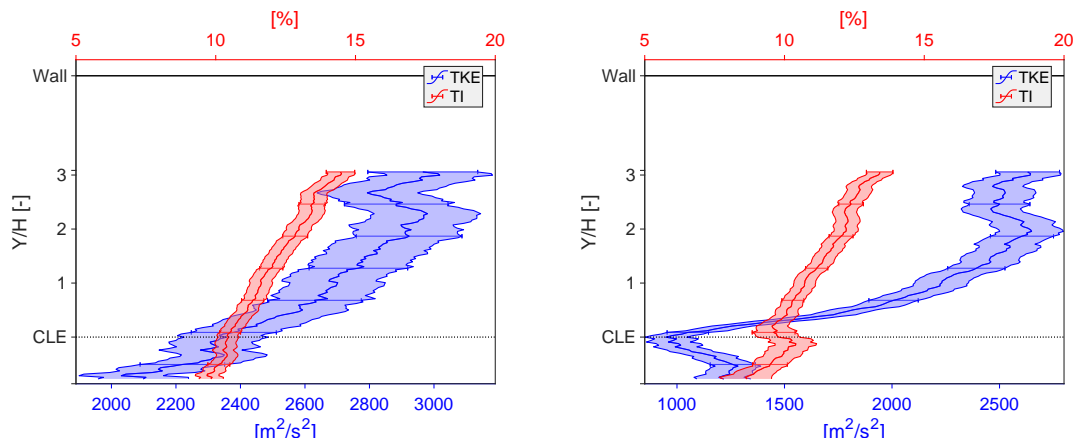


(d) Profiles of the RMS at  $Y/H=1.0$  plotted with 95% confidence intervals.



(e) Profiles of the RMS at  $X/H=-12.5$  plotted with 95% confidence intervals.

Figure 3.3: Corrected root-mean-square velocimetry for a flow Mach number of  $M = 0.66$  and a global ethylene equivalence ratio of  $\Phi_g = 0.47$  acquired upstream of the flameholder insert.



(a) Profiles of the TKE and TI at  $X/H=-12.4$  plotted with 95% confidence intervals. (b) Profiles of the TKE and TI at  $X/H=-10.2$  plotted with 95% confidence intervals.

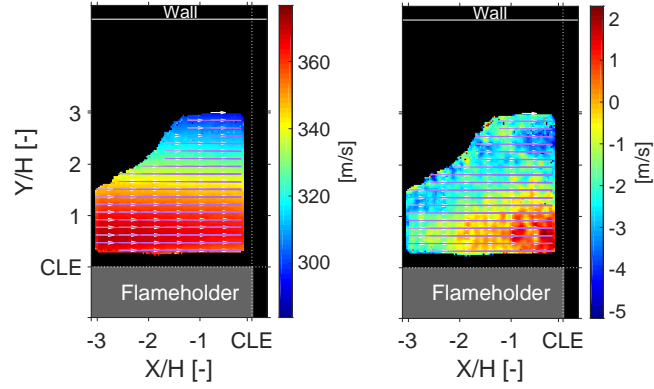
Figure 3.4: Turbulent Kinetic Energy (TKE) and Intensity (TI) for a flow Mach number of  $M = 0.66$  and a global ethylene equivalence ratio of  $\Phi_g = 0.47$  acquired upstream of the flameholder insert.

### 3.4 PIV at the cavity inflow

The inflow to the cavity is measured next as a direct boundary-conditions measurement for the companion DNS domain starting at  $X/H = -2.4$ , located in FOV A of figure 3.1. Furthermore, insert design requirements are verified: the boundary layer originating from the ILE is kept thin (for improved mass exchange across the cavity shear layer) and no re-circulation region from flow separation at the insert leading edge is observed. This constitutes, to the author's knowledge, the first dataset on inflow velocimetry to a dual-mode premixed cavity flameholder. In the following figures, the insert leading edge is located upstream at  $X/H=-10$  and the cavity leading edge (CLE) downstream at  $X/H=0$ , both at  $Y/H=0$ . The surface in between is flat and 30 mm long. The tunnel wall opposite to the flameholder is represented with the continuous line at  $Y/H = 4.8$  and the cavity floor is located at  $Y/H = -1$ . Sample sizes are in excess of 3,000 vectors across most of the FOV. In two-dimensional velocity fields, a sub-sample of average velocity vectors are displayed with white arrows to show flow directionality; streamlines in purple originate from each vector.

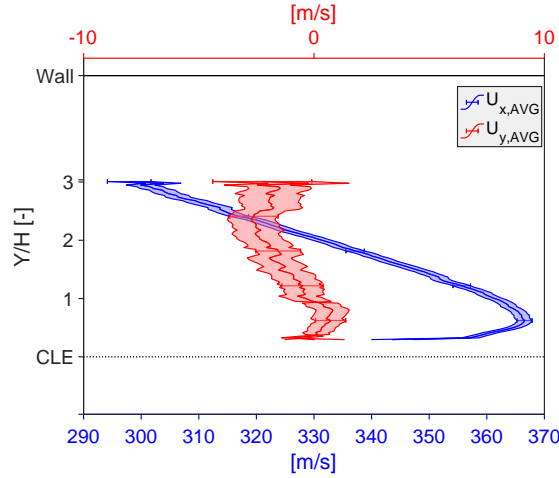
#### 3.4.1 Mean velocities

Mean velocities are shown in figure 3.5. A thick facility wall boundary-layer extends down to  $Y/H \sim 0.5$ , at which point it merges with the boundary-layer of the flameholder wall. This corresponds to a  $\sim 1.5$ -mm thin boundary-layer immediately upstream of the cavity. Omni-directional streamlines in purple demonstrate the absence of separated flow in the cavity inflow. The streamwise velocity gradually decreases as the flow approaches the cavity while the transverse component increases in the streamtube closest to the flameholder. These trends are consistent with the presence of the premixed flame starting at  $X/H = 0$ , which locally expands the flow. The change due to the cavity proximity begins at  $X/H \sim -2$ , validating the DNS domain boundary location at  $X/H=-2.4$ . Negative transverse velocities in the center of the constant area duct can be explained through residual flow adjustments from the deviation at the ILE, geometric discrepancies in the flowpath, or an error in the image rotation relative to the walls. The relative magnitude between components indicates a maximum error of  $1^\circ$  assuming freestream vectors in reality parallel to the flowpath walls.



(a) Streamwise mean velocities  $U_x, AVG$ . Uncertainties for a 95% confidence interval  $\in [3 - 4]$  m/s.

(b) Transverse mean velocities  $U_y, AVG$ . Uncertainties for a 95% confidence interval  $\in [0.5 - 1.4]$  m/s



(c) Profiles of the means at  $X/H = -1.4$  plotted with 95% confidence intervals.

Figure 3.5: Mean velocity components for a flow Mach number of  $M = 0.66$  and a global ethylene equivalence ratio of  $\Phi_g = 0.47$  acquired upstream of the cavity.

### 3.4.2 RMS velocities

RMS velocities in figure 3.6 reveal increasing fluctuations from the insert to the opposite wall (figure 3.6d) with similar profiles to FOV L and non-isotropic turbulence. RMS values in the duct core are similar to previously found values upstream of the leading edge. Since in FOV L  $U_{x, RMS}$  decreases approximately linearly at a rate of  $\frac{\partial U_{x, RMS}}{\partial x} \sim -540 \text{ s}^{-1}$ ,  $U_{x, RMS}$  is expected to be lower than 40 m/s. Therefore,  $U_{x, RMS} \sim 53 \text{ m/s}$  indicates turbulence production by the flow diversion over the leading edge. Figure 3.6e shows  $U_{y, RMS}$  remaining constant along X at  $\sim 20 \text{ m/s}$  while  $U_{x, RMS}$

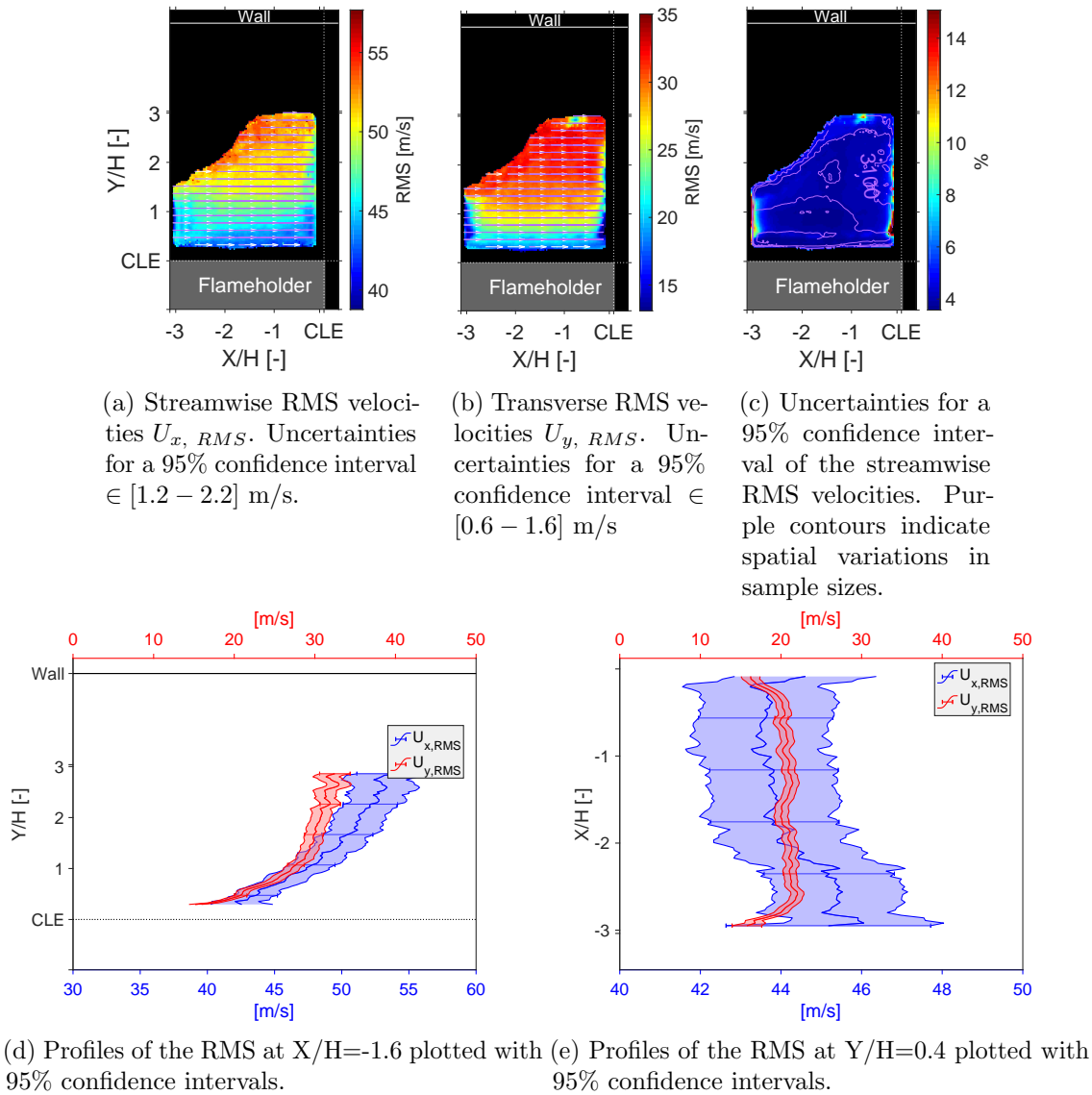


Figure 3.6: Corrected RMS velocity components for a flow Mach number of  $M = 0.66$  and a global ethylene equivalence ratio of  $\Phi_g = 0.47$  acquired upstream of the cavity.

decreases  $o(1)$  m/s between  $X/H = -3$  and  $-2$  before plateauing. This corresponds to the location where the transverse component becomes positive, indicating expansion of the boundary-layer from the downstream combustion process starting at  $X/H$ . As discussed in section 3.3.2, edge values should be considered cautiously as the uncertainties for the corrected RMS are significantly higher (figure 3.6c).

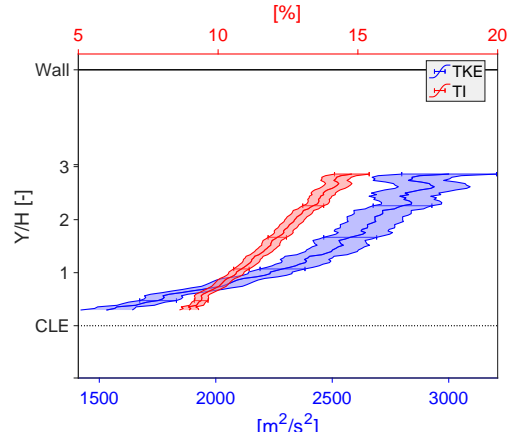


Figure 3.7: TKE and TI for a flow Mach number of  $M = 0.66$  and a global ethylene equivalence ratio of  $\Phi_g = 0.47$  acquired upstream of the cavity at  $X/H = -1.6$ .

### 3.4.3 Turbulent Kinetic Energy and Intensity

The TKE and TI distributions display similar trends and values to measurements upstream of the insert leading edge (figure 3.4b). The TKE and TI increase across the streamtube height as  $Y/H$  increases, from  $\sim 2,800$  to  $\sim 1,700$   $\text{m}^2/\text{s}^2$  and 14% to 9% respectively. Both display a constant trend along the tunnel axis.

### 3.5 Comparison between flow conditions

Investigation of the effect of the shock train location and heat release on the flow characteristics is performed by comparing the turbulence statistics of all the table 1.2 cases. Flow conditions are compared using the difference in average velocities and the normalized difference in RMS velocities upstream of the insert (FOV L). Uncertainties are propagated accordingly and differences in RMS are tested using the F-test. The F-test outputs statistical significance to reject a nil hypothesis, e.g.

$$H_0 : U_{x, RMS, case\ 1} = U_{x, RMS, case\ 2} \quad (3.1)$$

and accept the alternative, e.g.

$$H_1 : U_{x, RMS, case\ 1} > U_{x, RMS, case\ 2} \quad (3.2)$$

In this study, a p-value of 0.05 is used, meaning in the following that a statistical significance greater than 95% indicates that inequality between cases is most likely.

#### 3.5.1 Variation in global fuel equivalence ratio $\Phi_g$

Cases 1 and 3 are compared first to identify effects of varying the global fuel equivalence ratio  $\Phi_g$  from 0.47 to 0.37 at a constant Mach number of 0.66. Difference in average velocities are verified with PIV to be within  $o(1)$  m/s. Figure 3.8 presents the F-test results on the nil hypothesis

$$H_0 : U_{\beta, RMS, case\ 1} = U_{\beta, RMS, case\ 3}, \quad (3.3)$$

where  $\beta$  is the vector component  $x$  or  $y$ . The results are largely negative across the FOV, in particular for the transverse RMS. The streamtube between  $Y/H = 1$  and  $2$  may experience a slight increase from the increased  $\Phi_g$ . Primarily negative tests on

$$H_0 : U_{\beta, RMS, case\ 1} = 1.01 * U_{\beta, RMS, case\ 3} \quad (3.4)$$

reveal that any increase in this region may be considered negligible. It is therefore concluded that the flow properties are relatively insensitive to the equivalence ratio value. This matches expectations:

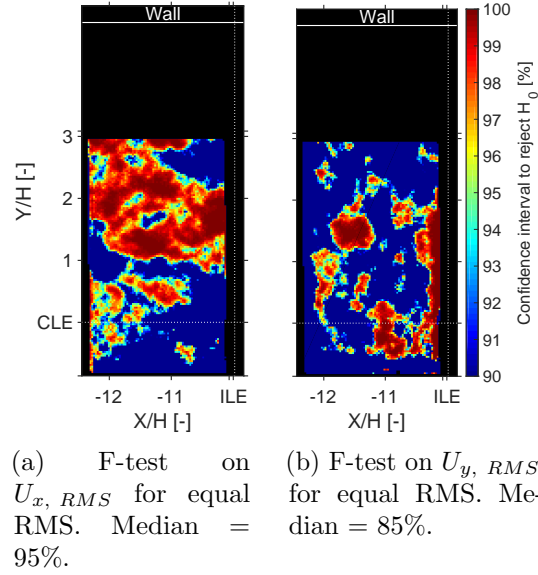


Figure 3.8: F-test results on case 1 versus case 3. Increase in mean velocities are  $o(1)$  m/s.

the cross-flow fuel jet is 180 cavity heights upstream and behind the shock train, hence turbulence generate by the jet should be negligible relative to the shock train. In addition, the added mass and momentum is small relative to the main flow,  $o(1)$  % and  $o(0.01)$  % respectively. Finally, influence of the combustion-generated heat onto the flow upstream of the cavity was previously shown to be limited to  $2*H$ , thus the present area spanning from  $X/H \sim -10$  to  $-12$  should not be affected.

### 3.5.2 Variation in the shock train location

Differences between the flow of cases 2 and 3 of table 1.2 are considered next to investigate the effect of the shock train location on turbulence. The global fuel equivalence ratio  $\Phi_g$  is maintained constant at 0.37 and the tunnel backpressure is adjusted to translate the shock train and vary the Mach number from 0.66 to 0.74. Average velocities in the core flow ( $Y/H=0$ ) increase by 25% to  $\sim 500$  m/s. A marked increase in RMS velocities is visible in figure 3.9, displaying positive values for the normalized difference defined by

$$\frac{U_{x, RMS,2}}{U_{x, RMS,3}} - 1. \quad (3.5)$$

across the FOV for both components with two regions delimited by  $Y/H \sim 1$ . Streamwise RMS velocities experience a greater change than the transverse component. This is confirmed with the

F-test which output a 95% median statistical significance across the FOV when testing

$$H_0 : U_{x, RMS, case 2} = 1.35 * U_{x, RMS, case 3}$$

and

$$H_0 : U_{y, RMS, case 2} = 1.20 * U_{y, RMS, case 3}$$

, corresponding to a 35% increase in the streamwise RMS and a 20% increase in the transverse RMS. This strong increase is confined within the upper streamtube for  $Y/H > 1$ , where the RMS velocity increase remains constant (3.9c). Following a transition, the RMS increase drops between  $Y/H=2$  and 0 before plateauing again for both components. Weaker hypotheses of

$$H_0 : U_{x, RMS, case 2} = 1.15 * U_{x, RMS, case 3}$$

and

$$H_0 : U_{y, RMS, case 2} = 1.1 * U_{y, RMS, case 3}$$

are rejected across the entire FOV, indicating minimum increases of 15% and 10% for  $U_{x, RMS}$  and  $U_{y, RMS}$  respectively. Hence a change in Mach number will incur significant effects on the flow turbulence attributed to the mixing region of the pseudo-shock described by Matsuo et al. (1999). The pseudo shock encountered in case 3 is measured on figure 1.11 (trace 5) 70H to 80H in length based on the pressure gradient reversal at  $X/H=-65$ . This length is in the lower portion of the expected 80H to 160H range based on compiled experimental results by Matsuo et al. (1999). The pressure trace of case 2 (trace 4) shows a 35H to 40H downstream shift of the shock train leading-edge but no pressure gradient reversal due to the flowpath divergence beginning at  $X/H=-36$ . The shock train length is in turn assumed to be longer than for case 3 due to the additional boundary-layer growth between the facility nozzle and shock train leading-edge Matsuo et al. (1999). Assuming a shock train length of 80H to 90H, the mixing region of the pseudo shock would end in the PIV FOV. The weaker turbulence decay in this area would explain the greater increase within the facility boundary layer, above  $Y/H \sim 1$ . Hence the increase values of 15% for  $U_{x, RMS}$  and 10% for  $U_{y, RMS}$  are retained for this investigation. The increase in turbulent fluctuations is attributed to the shorter

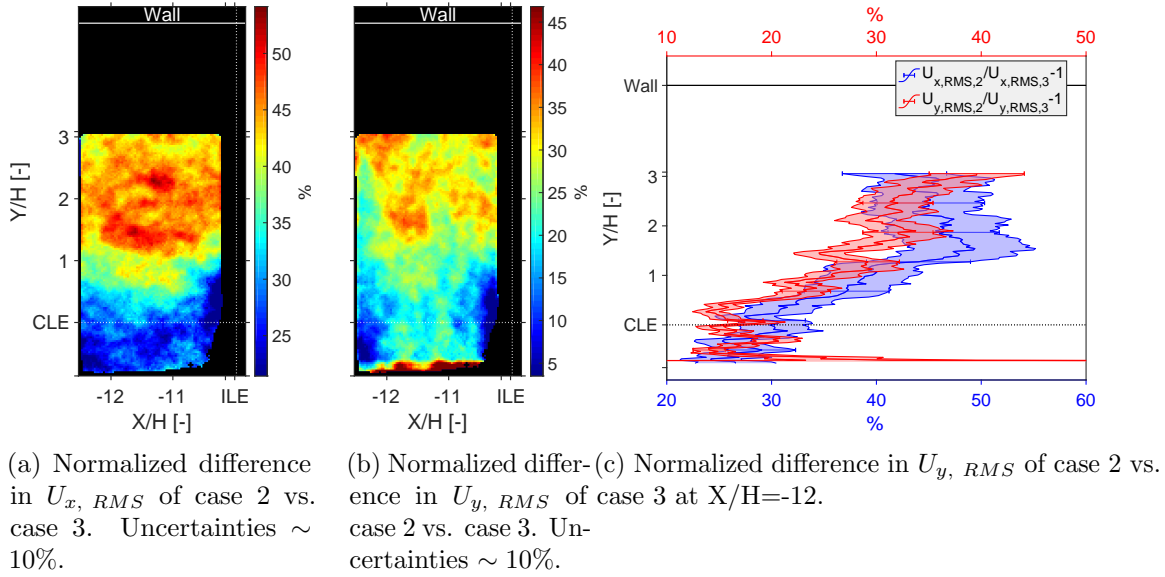


Figure 3.9: F-test results. Increase in AVG  $o(1)$  m/s.

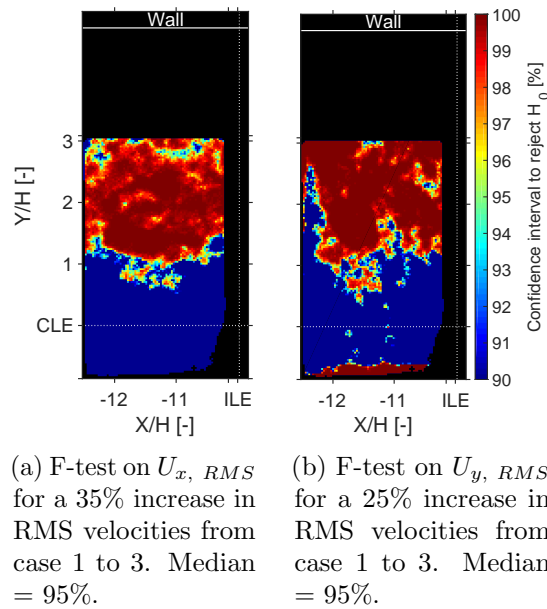


Figure 3.10: F-test results on case 1 versus case 3.

distance from the main turbulence source, i.e. the shock train, hence decreasing the decay of the turbulent fluctuations. In summary, this test demonstrated that the turbulence characteristics are very sensitive to the shock train location, increasing RMS velocities when the shock train is shifted downstream.

### 3.5.3 With and without heat release

Finally, the influence of heat release on the inflow to the insert is tested by comparing the case of maximum heat release with no heat release. Two experimental cases are compared, between which the global equivalence ratio of  $\Phi_g = 0.47$  and Mach number of  $M = 0.66$  are kept identical. The premixed flow is however not ignited in case 4 and the shock train is placed at the position of the combusting case with the air throttle, which simulates the heat release. Applying the F-test on

$$H_0 : U_{i, RMS, case\ 1} = U_{i, RMS, case\ 4}$$

returns unequivocally negative results across the domain and retains the  $H_0$  hypothesis. Therefore the heat release occurring downstream, in the cavity and beyond, does not affect the boundary conditions of the CFD domains. This result is consistent with the observations in region A of section 3.4, where the heat release from the cavity is found not to affect the flow velocity fluctuations upstream of  $X/H=-2$ .

Table 3.1: Integral length scales measured from PIV data

Case	$\eta_{xx}$	$\eta_{yy}$
1	9.0 mm	3.7 mm
2	> 6.6 mm	3.0 mm
3	> 6.6 mm	4.0 mm

### 3.5.4 Integral Length Scales

Integral length scales at the inflow are computed using a space correlation at a measurement point located upstream of the insert leading edge at  $X/H = -12$  and  $Y/H = +2$ . The correlation is repeated over the entire stack and the mean curve outputted. The integral length scale is taken as the length from this point at which the correlation value reaches  $1/e$ . For cases 2 and 3, the  $\eta_{xx}$  correlation curve did not reach  $1/e$  over the shorter available FOV width and thus is given as greater than the latter (6.6 mm). Results are summarized in table 3.1 for the different cases of table 1.2. In all cases, the turbulence is observed to be highly anisotropic with  $\eta_{xx} \gg \eta_{yy}$ . While expected for this flow and consistent with the difference in RMS components, another contributing factor large scale axial oscillations unrelated to turbulence such as thermoacoustic waves observed by Allison et al. (2017). While trends are expected to be similar between  $\eta_{xx}$  and  $\eta_{yy}$ , only  $\eta_{xx}$  will be considered in the following analysis. Increasing the flow Mach number at a set equivalence ratio (case 2 versus 1) is seen to decrease  $\eta_{yy}$  by 20%, a trend which is consistent with the shorter distance from the turbulence source (the shock train) limiting its decay. Conversely, decreasing the equivalence ratio at a set flow Mach number increases  $\eta_{yy}$ . This may be due to the weaker cross-flow jet of fuel in the isolator, however the small difference relative to the method accuracy would warrant further investigation to confirm this trend.

### 3.6 Particle Flow Tracking Assumption

Accurate flow tracking with minimal bias errors is a critical assumption in PIV to ensure reliable velocimetry. The problem is two-fold: the tracers must accurately follow the gas phase, and the post-processing algorithm must accurately track the tracers. The latter is detailed in chapter 2 on both synthetic and experimentally-acquired PIV. In particular, the LCS pre-filtering is demonstrated in section 2.5.1 to significantly decrease bias errors to levels manageable by commonly-used post-processing filters, e.g. median and peak ratio filters. Random errors are increased by LCS pre-filtering but are captured by the *a-posteriori* estimator of Wieneke (2015). The tracers flow-tracking assumption is more challenging to test as it implies prior knowledge of the gas velocity. This assumption is usually tested with a theoretical study or a numerical simulation. No particle perfectly tracks any flow due to the two-phase nature of the problem, resulting in a particle lag or lead characterized by a particle response time. The response time can however be decreased to acceptable levels for the purpose of a specific measurement by selecting an adequate particle material and geometry as detailed below.

#### 3.6.1 Background on the graphite nanoflakes selection and flow tracking theory

Commonly-used PIV tracer materials for reacting flow studies include oxides of aluminum, titanium, and silicon ( $\text{Al}_2\text{O}_3$ ,  $\text{TiO}_2$ ,  $\text{SiO}_2$ , Chen and Liu (2018); Melling (1997)). These tracers are spherical and the theory on the particle response time of spheres is well developed and tested. The theoretical Stokes drag model can be applied to the graphite nanoflakes and  $\text{SiO}_2$  particles used in this study since their dimensions are  $\text{o}(1) \mu\text{m}$  or lower. Details and derivations for the equations below may be found in Kirik et al. (2017) and Loth (2008). Two key quantities include the particle slip velocity, defined as the difference between the instantaneous particle velocity  $\vec{u}_p$  and the fluid velocity  $\vec{u}_f$  at the same location:

$$(\vec{u}_p - \vec{u}_f) = - \left( \frac{\rho_p d_{vol}^2}{18\mu f} \right) \vec{u}_p \frac{d\vec{u}_p}{d\vec{x}} \quad (3.6)$$

The other quantity is the particle response time, defined as the time needed for a particle to reach of the flow velocity past a step change.

$$\tau_p = \frac{m_p}{3\pi d_{vol}\mu f} \quad (3.7)$$

$f$  is the Stokes correction factor (ratio of the particle drag to that of a spherical particle of the same volumetric diameter  $d_{vol}$ , dependent on particle geometry only and equal to 1 for a sphere. For the graphite nanoflakes, particles are modeled as an oblate spheroid). To relate the particle response time to the flow fluctuations, the Stokes number is a non-dimensional number used to assess flow tracking:

$$St_D = \frac{\tau_p}{\tau_D}, \quad (3.8)$$

where  $\tau_p$  is the particle relaxation time when responding to a step acceleration of the fluid, and  $\tau_D$  the domain timescale.

The commonly-used PIV tracers above are however not suitable for velocimetry in the cavity and freestream of high-enthalpy flows due to gradual window fouling in regions where the residence time and temperature are high, e.g. in the re-circulation region of the cavity. Adhered particles quickly accumulate on windows to the extent of suppressing optical access. Kirik et al. (2017) demonstrated PIV of a cavity flameholder in dual-mode scramjet conditions using graphite nano-flake tracers. The latter prevent window fouling through a combination of lower adhesion rates and combustion in stagnant areas. The flakes were measured to a length of  $1.1 \pm 0.12 \mu\text{m}$  and a thickness of  $16 \pm 2.4 \text{ nm}$  for 95% confidence intervals (Kirik et al., 2015). Particle slip was extensively studied theoretically by Kirik et al. (2017) who used the same particles. The graphite nanoflakes are assumed adequate for this application since the Stokes number  $St = 0.023$  (based on the integral length scale and maximum shear layer mean velocity) remains below the 0.25 rejection criterion suggested by Samimy and Lele (1991). In addition, Samimy and Lele (1991) concluded that the RMS error stemming from aerodynamic slip was less than 1% for  $St < 0.1$ , which is verified for the flows of this dissertation. Hence particle slip is taken into account with a 1% bias error added to the RMS velocities. The flake nature of these particles is necessary due to unavailability of spherical graphite particles with  $St < 0.25$ . Indeed, the smallest commercially available spherical graphite particles were found to be  $3 \mu\text{m}$  in diameter, resulting in Stokes numbers of  $St_D = 2.8$  and  $St_K = 35$  above the 0.25 threshold. Diffraction-limited imaging however compensates for the irregular flake shape. Particle images result in Airy disks on the camera sensor as described in section 2.2.4, which approximate as Gaussians and can be cross-correlated identically to spherical particles.

### 3.6.2 Comparison experiment between tracers

#### Experimental setup

Previous work in the UVaSCF used 250 nm spherical SiO<sub>2</sub> to seed a hydrogen fuel jet in the core of the freestream (Rice et al., 2015), avoiding exposure of the windows to the particles and thus fouling. The Stokes number of the SiO<sub>2</sub> nanospheres based on the turbulent integral length scale is 0.031 i.e. 35% larger than the Stokes number of graphite nanoflakes. Since accessing the gas phase velocity is impossible with the available capabilities, velocimetry acquired with the graphite nanoflakes is compared with SiO<sub>2</sub> results, considered a reference. In order work with a common flow configuration and match the latter as closely as possible to the experiments in this dissertation, measurements are conducted in the UVaSCF at its isolator exhaust.

Figure 3.11 illustrates the experimental setup. The PIV hardware and its arrangement are identical to those described in chapter 3, section 3.2. The combustor and downstream sections are removed, leaving the flowpath as a 16 inches-long straight rectangular duct. A Mach 2,  $T_0 = 1200$  K flow is established at the converging-diverging nozzle exit. Particles are injected in the upstream portion of the isolator, immediately before nitrogen jets simulating fuel injection. The absence of air throttle locates the shock train further downstream than in experiments, with its leading edge between 20 and 50 mm before the exit plane. The exhaust jet is perfectly expanded to atmospheric pressure and creates a shear layer with the ambient air along which the flow is decelerated and velocity fluctuation gradients are broadened. The PIV measurement plane is located in the shear layer where the high level of turbulence and decelerating axial velocities constitute a robust test on the tracers flow tracking. The particles with the best flow tracking are expected to have greater drag and thus display more intense fluctuations further out into the shear layer. This would correspond to a relatively larger gradient in the mean and larger RMS values at a given location. Post-processing for the graphite particles is described in chapter 3, section 3.2 and is identical for the SiO<sub>2</sub> with the exception of no LCS pre-filtering.

#### Results and discussion

Figure 3.12 overlays the mean axial velocity profiles along the transverse axis. Both exhibit an s-shaped profile with a strong gradient, which is characteristic of a high-speed shear layer. The



Figure 3.11: Schematic of the flow path and PIV field of view up to scale relative to the tunnel.

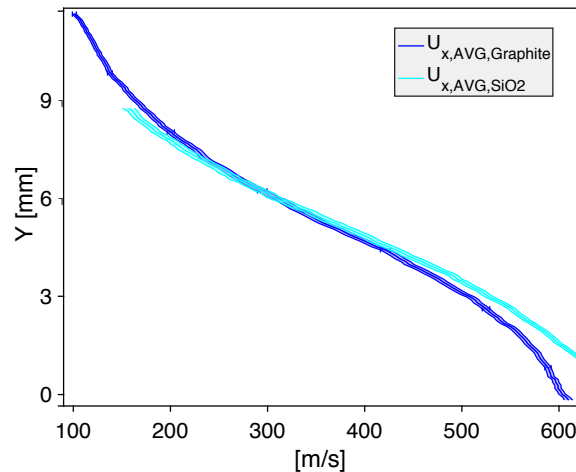


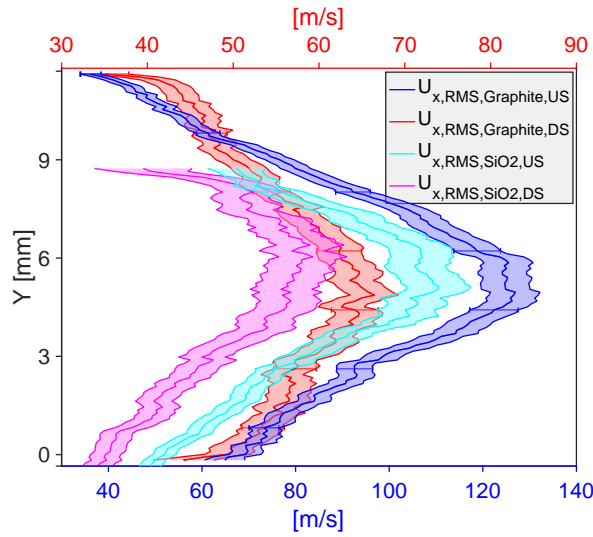
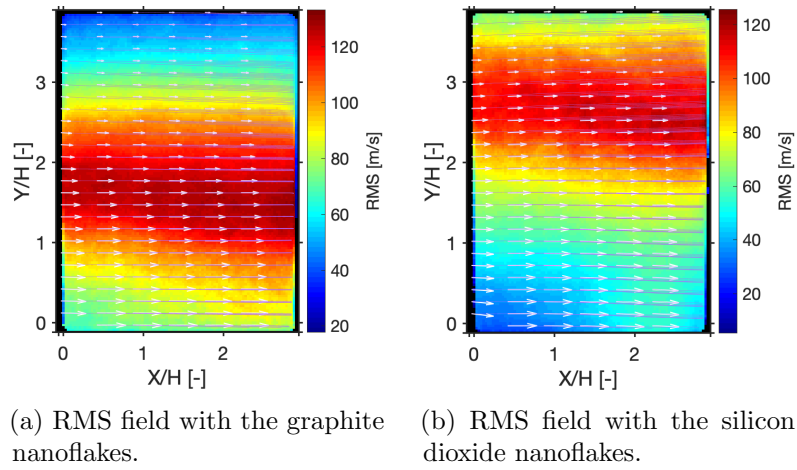
Figure 3.12: Comparison of the average velocities between the graphite nanoflakes and the silicon dioxide nanospheres.  $H$  is a reference dimension corresponding to the cavity height of 3 mm.

silicon dioxide nanospheres exhibit a relatively greater gradient, indicating that the particles do not adjust to the strong changes in velocity through the shear layer as quickly as the graphite nanoflakes. This trend is confirmed with the following analysis on the RMS values. Figure 3.13 displays the comparison of the axial RMS values between the two tracers. Similar trends are observed for the transverse RMS. The two datasets had to be acquired on separate days due to safety restrictions. The location of the tunnel exhaust shifted by about 2.5 mm along the  $y$  axis as seen in the RMS fields of figure 3.13a and 3.13b. Hence the plots of  $\text{SiO}_2$  in figure 3.13c are shifted by 2.5 mm for ease of comparison. It is possible that the tunnel exhaust position shifted in other dimensions, however the following conclusions are demonstrated to be independent of potential shifts. Figure 3.13c displays the axial RMS profiles taken at two axial locations separated by 7.5 mm and plotted along the tunnel  $y$ -axis. Both the graphite and silicon dioxide tracers exhibit the expected trends of a jet shear layer: a bell-shaped gradient in the RMS velocities is observed across the shear layer. Along the shear layer, the RMS velocities are spreading and their peak value diminishing. The

RMS velocities of the silicon dioxide are consistently lower than the graphite nanoflakes. Higher values are indicative of better tracking of local fluctuations and support the hypothesis that graphite nanoflakes have higher drag than the silicon nanospheres. While lower RMS values could be due to a streamwise shift of the tunnel exhaust relative to the PIV camera, the greater broadening of the graphite particles RMS profile relative to the silicon dioxide between the same two measurement points is indicative of better flow tracking capabilities for the graphite nanoflakes. Greater RMS velocities at the edges of the shear layer indeed indicate a shorter response time of this particle to the local increase in flow fluctuations. This is consistent with the 35% higher Stokes number of  $\text{SiO}_2$  relative to graphite nanoflakes, which, given the identical flow timescales, corresponds to a 35% shorter particle response time to a step change in velocity for the graphite nanoflakes.

### 3.6.3 Conclusion

In conclusion, experimental tests confirm the theoretical analysis of the tracers flow tracking accuracy. While the particle response time of spheres has been extensively studied, the approximations used for flakes raised concerns about their actual flow tracking capability. However, the measurements in the exhaust shear layer of the UVaSCF confirm that the graphite nanoflakes used in this study exceed the flow tracking capabilities of the proven spherical silicon dioxide tracer. This conclusion, combined with the demonstration with synthetic PIV in section 2.5.1 that the LCS filter significantly decreases velocimetry bias errors, adds confidence in the adequacy of the uncertainty model used to assess measurement quality. The latter uncertainty model assumes a RMS bias error of 1% based on the study of Samimy and Lele (1991) for particles with a Stokes number less than 0.1.



(c) Profile plots of the RMS axial component taken at two different axial locations separated by 7.5 mm. The cyan and blue curves share the bottom x-axis. US refers to upstream and DS to downstream. Contours indicate the 95% confidence level. H is a reference dimension corresponding to the cavity height of 3 mm.

Figure 3.13: Comparison of RMS velocities between the graphite nanoflakes and the silicon dioxide nanospheres.

### 3.7 Conclusion

The inflow to a cavity flameholder in a high-speed continuous flow facility has been characterized using the highest resolution velocimetry available yet for high-speed thermally convective flows, achieving  $355 \mu\text{m}$ . The dataset captures a broad range of the spatio-temporal turbulence spectra to constitute a more comprehensive reference for high-resolution numerical simulations. Different inflow planes, shock train locations, and heat release rates are considered and form a dataset to prescribe boundary-conditions to DNS models of cavity flameholders. In addition, the present work represents the first characterization of the inflow to an immersed model in a direct-connect facility converted to a semi-free jet rig and validates critical design constraints. The inflow to the immersed model is characterized by the two facility boundary layers extending to mid-duct. Smooth divergence of the flow around the thin leading-edge was verified with no flow separation detected, validating the immersed model design. Key values at this inflow plane include the turbulent intensity increasing from 10% mid-duct to 14% three cavity heights above the insert. Past the model leading edge and at the boundary location of the companion DNS work, the flow is unaffected by the heat release occurring in the cavity validating DNS initialization with a channel simulation (Rauch et al., 2018). Turbulent statistics are shown constant along the streamwise axis up to two cavity heights upstream of the cavity leading edge. The boundary-layer at the insert remains thin at half a cavity height in thickness, allowing for the formation of a thin shear layer over the cavity promoting combustion radicals mixing and flame wrinkling. Variations of the heat release rate showed no significant difference in the velocities at the model inflow plane. However, a further downstream shock train location leads to an increase  $\mathcal{O}(10)\%$  in RMS values across the entire FOV. Hence, in reproducing experiments in numerical simulations, matching the Mach number and shock train location is important to accurately mirror the turbulent statistics and combustion physics while slight variations in fuel equivalence ratio may not significantly influence turbulence characteristics at the boundaries.

In the following chapter, velocimetry at the cavity is presented along with simultaneous OH PLIF in an effort to better understand cavity flow and combustion dynamics.

## Chapter 4

# Combined PIV-PLIF of High-Speed Cavity-Stabilized Combustion

## 4.1 Introduction

As high-speed air-breathing propulsion and pollutant emission reduction in aircraft gas turbines generate growing interest, understanding of fundamental physics governing cavity flameholders becomes ever more critical. In particular, cavity flameholders are a commonly-considered solution for hydrocarbon-fueled dual-mode scramjets. Hydrocarbon fuels are easier to store and handle than hydrogen and therefore considered more practical. In the absence of a flameholder in the engine, the longer reaction times of these fuels inhibit the complete release of their chemical energy before exiting the scramjet. Cavities solve this problem by locally increasing the residence time, creating a shear layer and flow recirculation (Ben-Yakar and Hanson, 2001). Combustion radicals are produced in the cavity before being diffused through turbulent fluctuations across the shear layer and intermittently ejected into the main flow (Kirik, 2017). In addition to applications in scramjet combustors, cavity flameholders are valuable means for the fundamental research on high-speed combustion by establishing in a premixed free stream a flame with a relatively large normal velocity. The intricate interactions between the flow unsteadiness and chemical reactions are however not fully understood and warrant further investigation. In particular, combustion instabilities in pre-mixed dual-mode scramjet flowpaths with a cavity flameholder have been a phenomenon not yet fully understood (Wang et al., 2014). The problem is critical to enable operational engines and reliable CFD simulations.

The present work is part of a larger collaborative effort to deepen the fundamental understanding of cavity-stabilized combustion including its relation with flow compressibility and heat release rates. To that end, simultaneous Particle Image Velocimetry (PIV) and hydroxyl (OH) Planar Laser-Induced Fluorescence (PLIF), hereafter PIV-PLIF, are conducted on a high-speed reacting cavity flow. The benefits are threefold relative to separate PIV and PLIF acquisitions: flow-chemistry coupling is investigated with instantaneous measurements, bias towards reactants in regions of intermittent presence with products are alleviated, and complementary validation metrics are provided to companion CFD work. In particular, direct numerical simulations (DNS, discussed in Rauch et al. (2018)) are being conducted parallel to the present experimental work to gain insights at the finest spatio-temporal scales. The results presented below therefore constitute the first published reference dataset on a DNS-friendly high-speed reacting cavity flow.

Scramjet combustors with flush or ramp injectors have been extensively studied (Chen and Liu, 2018; Laurence et al., 2015; Le Pichon and Laverdant, 2016; Rockwell et al., 2014). High-speed cavity flameholders have constituted a more recent topic of interest. Tuttle et al. (2014) published the first study of these flameholders operating in scram-mode by implementing PIV and comparing results to a separate PLIF study to study the dependence of velocity behavior on the heat release in the cavity and shear layer. These authors found a strong coupling between various velocimetry statistics and heat release rates, noting the value simultaneous PIV-PLIF would hold in order to clarify coupling between heat release and velocity. Research on premixed and dual-mode scramjet combustors with a cavity flameholder is particularly recent, with the only study known to the author by Kirik et al. (2017) conducted on the same facility as the present work but with a larger cavity and flowpath. The investigators characterized premixed cavity aerodynamics and its relation to both the shock train upstream location and the fuel equivalence ratio by conducting PIV and PLIF as separate experiments. In particular, their comparison of the peak fluctuations in velocities and relative OH levels suggest an unsteady combustion process whereby pockets of combustion products produced near the ramp are intermittently ejected into the main duct flow. Allison et al. (2017) performed CH\* chemiluminescence imaging on a similar cavity flameholder flowpath in the UVaSCF. These authors found a characteristic frequency of 340 Hz in the CH\* signal and flame brush, which is likely due to acoustic waves between the shock train and flame front. Stable combustion is desired for operational application on aircrafts, hence the mechanisms driving combustion oscillations warrant further investigation. Wang et al. (2014) reviews recent progress on combustion oscillations in dual-mode scramjets and highlights their variety and complexity. Thermoacoustic oscillations  $\sim$ 100 Hz occur from shock train and flame front interactions while the cavity shear layer is expected to oscillate at high frequencies, particularly for low heat release rates. Lin et al. (2010) used a high-frequency pressure sensor and theoretical/numerical analysis to study oscillations in a dual-mode, non-premixed scramjet flowpath. For the conditions closest to the present work with a single-sided injection from the cavity wall, a dominant frequency of 368 Hz is measured. The oscillation is attributed to acoustic-convective wave interactions in an injector-flame loop with a theoretical prediction. In this case, the oscillation in local heat release rate send upstream an acoustic wave which modifies fuel penetration and mixing and thus subsequently the combustion. Hybrid LES/RANS by Ramesh et al. (2018) on a dual-mode premixed flowpath with a cavity flameholder observed a 357 Hz cyclic

combustion pattern. While the oscillation may be physical, the non-satisfaction of the Rayleigh criterion and its large amplitudes hint at a computational aberration. Their work nonetheless gives valuable insights into interactions between the shock train and the cavity-stabilized flame. These authors report a heat release oscillation, with reduced rates occurring with mass accumulation in the facility combustor, a cavity pressure maximum, and an upstream-propagating normal shock wave; maximum heat release is associated with a positive mass flow rate due to ejection events, and higher duct flow velocities. Non-simultaneous PIV and PLIF measurements on single- and dual-mode scramjet combustors also observed hints at an oscillatory combustion pattern. Tuttle et al. (2014) suggest an intermittently-stable shear layer flame driving cavity combustion dynamics in a supersonic flow, whereby heat release influences the shear layer impingement location and the formation of the re-circulation-zone eddy structures. Kirik (2017) observed the adjacent locations of the strongest turbulent fluctuations to high OH concentration fluctuations, hinting at the intermittent release of high-temperature products and radical species from the cavity. Both Tuttle et al. (2014) and Kirik (2017) noted that simultaneous PIV-PLIF would help understanding the instantaneous mechanism behind the unsteady combustion process. Cavities without combustion have been extensively studied and provide additional material to interpret the mechanisms behind reacting cavity instabilities. Gharib and Roshko (1987) report on a locked vortex configuration within the cavity corresponding to stable flow. This configuration is however established at the cost of low mass exchange between the cavity and the duct flow. (Ben-Yakar and Hanson, 2001), in a comprehensive review about cavity flows, described the phenomenon of longitudinal oscillations in non-combusting rectangular cavity flow. These oscillations are driven by shear layer unsteadiness adding and removing mass at the cavity closeout. When the freestream flow enters the cavity at the impingement point, a compression wave propagates upstream, impacts the front wall, and generates small vortices at the leading edge. These eddies are in turn convected downstream, being amplified along the way. The cycle ends with vortex shedding, ejecting the mass initially added. Suppression of these cavity oscillations may be achieved with an oblique closeout wall to prevent the reflection of acoustic waves, as implemented in the present flowpath geometry. Low speed reacting flows in closed cavities were studied by Xavier et al. (2016), who resolved a full instability cycle with combined kHz PIV-PLIF. These authors highlighted the complex coupling between shear layer instabilities and the observed pulsed combustion regime. These investigators observed a strong product ejection event as the

pressure and equivalence ratio fluctuations become nil. A stable combustion mode was reached for an increased free stream momentum, which contains the cavity flow and constrain combustion to within the shear layer. They advanced the hypothesis that large velocity fluctuations between the cavity and the main flow cause full shear layer modifications.

While separate PIV and PLIF measurements can give important insights by relating key turbulence characteristics with combustion-related statistics, they are limited by their temporally-uncorrelated nature. As a result, the analysis is constrained to relating independent statistical quantities. In addition, small variations within or between runs in total pressure, total temperature, or equivalence ratio further add to the limitations of this approach. In contrast, PIV-PLIF enable highly-correlated measurements in time and space, providing deeper insight into the critical coupling between combustion physics and fluid mechanics (Chen and Liu, 2018; Gamba et al., 2013; Tanahashi et al., 2005; Xavier et al., 2016). The fundamental added value of PIV-PLIF is the knowledge of the distribution of products and reactants relative to the velocity fields for each instantaneous measurement, which is exploited in several ways. First, the velocity field can be divided into products and reactants domains — i.e. conditional velocities — from which stem conditional statistics, e.g. conditional means. Second, the instantaneous OH region boundaries from the PLIF signal approximate the local flame curvature and angle, which can then be related to the flow swirl, turbulence intensity, and direction. Third, knowledge of both the instantaneous flow dynamics and flame location provides complementary knowledge to characterize the flame anchoring process in terms of temporal dynamics. By leveraging the unique capabilities of simultaneous PIV-PLIF listed above, the present work aims to quantify the key characteristics of the chemically-reacting flow field of dual-mode cavity flameholders.

This work provides the first dataset of correlated velocimetry and OH distributions including conditional velocimetry statistics for numerical studies, to better understand flameholding mechanisms at play in cavities. In particular, the mass transfer across the cavity boundary, the conditional velocimetry, and flame angle are investigated through mean and RMS velocity fields, the turbulent kinetic energy, and the turbulence intensity for both the full velocity field and conditional velocities; as well as the characterization of the cavity in terms of the recirculation regions, shear layer impingement location, flame anchoring location and temporal dynamics. The mean flame angle will be computed based on the mean velocities and the the flame front probability density

distribution. In addition, the mass transfer of products and reactants at the cavity interface will be estimated based on the average transverse conditional velocities.

The chapter is structured as follows. First, the combined setup and post-processing are summarized. Second, the DNS-friendly, scaled-down, and immersed cavity flow is characterized with statistics and key values provided as references for CFD work. Finally, combustion dynamics are investigated with instantaneous measurements and a hypothetical cyclical combustion cycle is suggested for dual-mode scramjet cavity flameholder instabilities.

## 4.2 Method and Setup

### 4.2.1 Flow configuration and experimental setup

The present measurements will be conducted on the flowpath detailed in section 1.2 and depicted in figure 1.1 . Measurements are acquired in the field of view (FOV) spanning the cavity (B in figure 4.1).

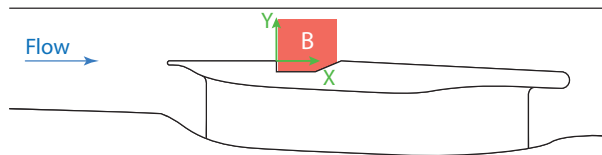


Figure 4.1: Field of view of the present work up to scale relative to the model insert.

The hardware and software system for the PIV-PLIF measurements is summarized next and illustrated in figure 4.2. The PLIF setup and measurements were conducted by Clayton Geipel and Andrew Cutler. Details may be found in Geipel et al. (2017) and Geipel et al. (2019). The qualitative OH concentration measurement is used in this work as an indicator for combustion product presence. Both the PIV and OH-PLIF measurements are two-dimensional, relying on the assumption of nominally two-dimensional flow in the cavity as concluded in a previous CFD study by Ramesh et al. (2018). The PIV and PLIF systems are run from a common external signal generator. PIV is effectively measuring the average displacement between the two laser pulses, thus the signal generator is set for the PLIF laser pulse to occur half-way between the two PIV laser pulses as measured by a photodiode. The PIV laser is a double-cavity, 10 Hz Spectra Physics PIV-400 Nd:YAG laser delivering two 532 nm-pulses of 500 mJ each, with inter-pulse delays of  $\Delta t = 300$  or 600 ns. In order to maintain the fluence at the mirrors and model below damage thresholds, 95% of the energy is dumped using beam splitters. The PIV and PLIF laser beams are merged using a dichroic filter before the sheet-forming optics for consistency. The laser sheet is formed with telescoping optics to a constant height  $\sim 25$  mm. The PIV laser sheet waists are  $\sim 140 \mu\text{m}$ , while the PLIF laser sheet is  $75 \mu\text{m}$  (see figure 4.3), both constant across the FOV. The laser sheets are co-planar with the tunnel center plane.

The PIV and PLIF cameras are mounted on the same set of translational stages to measure multiple fields of view per run. The PIV camera is a 14-bits,  $1600 \times 1200$  px LaVision Imager

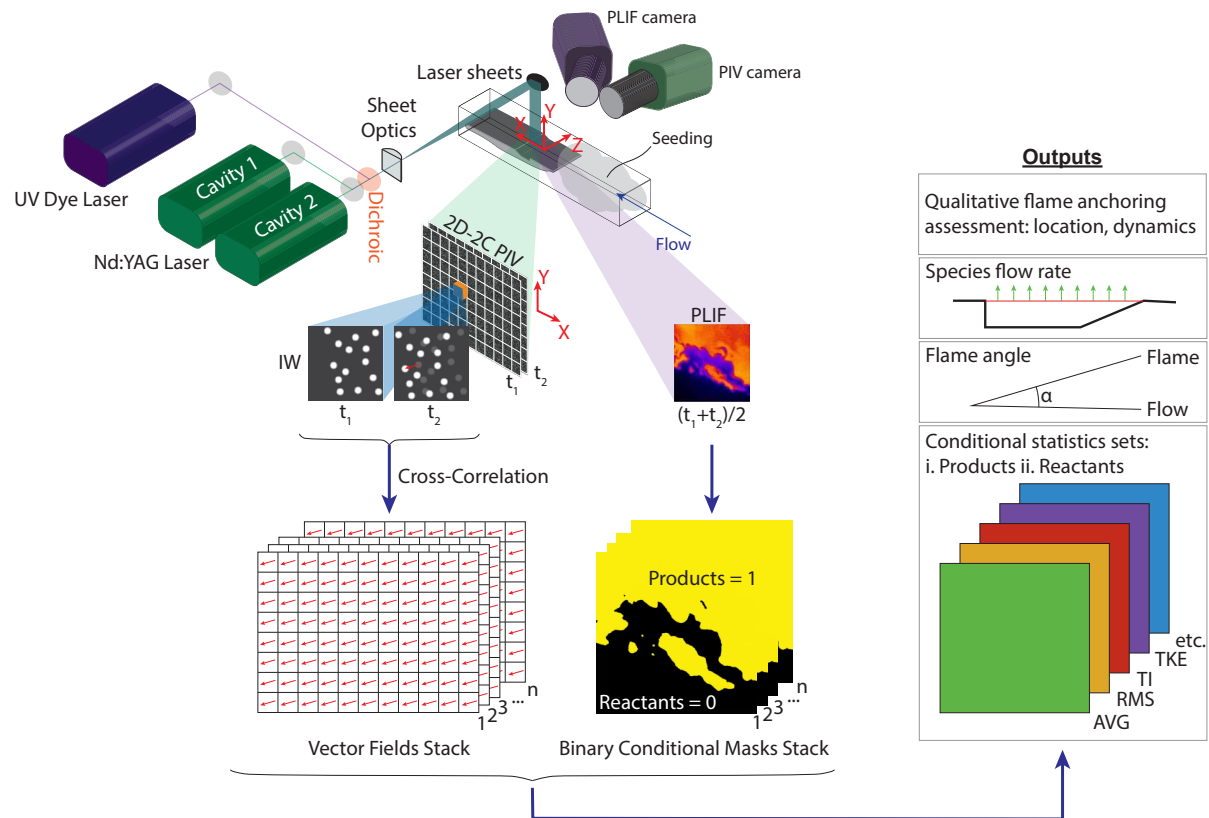


Figure 4.2: Principle of the combined PIV-PLIF technique as described in section 4.2. AVG: average; RMS: Root-Mean-Square; TI: Turbulence Intensity; TKE: Turbulent Kinetic Energy.

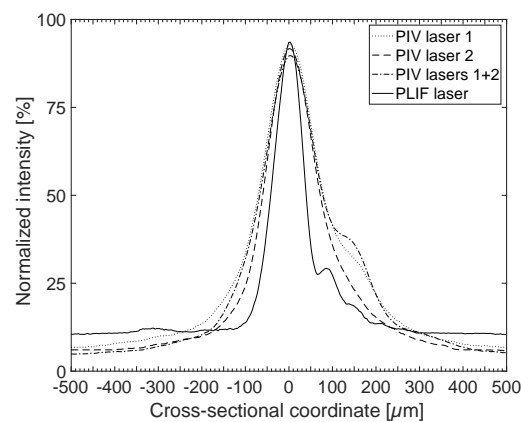


Figure 4.3: Laser sheets cross-sectional intensity profiles.

Pro X 2M. Angled by 4 degrees about the tunnel x axis to mask laser reflections off the wall, a Scheimpflug lens adapter adjusts the focal plane back onto the laser sheet. The camera is mounted with a Micro-Nikkor 105mm f/2.8 lens at a magnification  $m = 1 : 1.8$  and an f-number of 11, and a

$532 \pm 10$  nm-wide bandpass filter. The lens magnification corresponded to the maximum allowed by the setup constraints: the PIV and PLIF cameras must image the same FOV with 105 and 100 mm lenses and the maximum angle allowed by the PLIF camera Scheimpflug angle adapter. The PLIF camera is angled by approximately 30 degrees about the tunnel y axis to match the PIV field of view. Due to the viewing angle, the region near the cavity ramp is shadowed to the PLIF camera. In addition, the FOV is shifted slightly downstream of the cavity leading edge to avoid imaging laser reflections with the PIV camera, causing clipping of the region immediately behind the cavity backward-facing step. The imaging systems are calibrated simultaneously using a grid with  $250 \mu\text{m}$  dot spacing. FOV overlap is performed by dewarping and scaling the grid images from both systems before overlapping a spatial marker and all dots across the images. The overlap accuracy is estimated on the order of  $10 \mu\text{m}$ .

Experimentally diagnosing combusting flows is associated with key challenges, including temperatures greater than 2000 K, wide-spectrum radiation from the flame, and strong gradients in thermo-fluid dynamic variables (Stella et al., 2001). This is compounded with the facility high-enthalpy flow, causing the commonly-used PIV tracer materials (e.g. oxides of aluminum, titanium, and silicon ( $\text{Al}_2\text{O}_3$ ,  $\text{TiO}_2$ ,  $\text{SiO}_2$ , (Chen and Liu, 2018; Melling, 1997)) to stick onto the facility windows. This optical obscuring occurs quickly to the extent of preventing flow visualization. Kirik et al. (2017) introduced the use of graphite nano-flakes as tracer particles for the PIV of a cavity flameholder. These  $1.1 \mu\text{m}$ -long and 16 nm-thick flakes have an estimated Stokes number of  $St \sim 0.05$  Kirik et al. (2015) corresponding to RMS velocity errors of less than 1% (Samimy and Lele, 1991). Graphite particles prevent window fouling through a combination of lower adhesion rates and combustion on the windows. Seeding of the graphite nanoflake tracer particles for PIV (Kirik et al., 2015) is performed with a fluidized bed seeder (Howison and Goyne, 2010). The particles are injected upstream in the isolator, before the fuel injectors and on the centerline. The tracer particles are diffused across the cavity-side half-streamtube.

### 4.2.2 Data processing

The PIV processing methodology is presented first, then the PLIF. The graphite nanoflakes used as PIV tracers have a low, angle-dependent reflectance causing poor signal-to-noise ratios. A novel approach solves this problem by pre-processing the images with a Logarithm Contrast-Stretch (LCS)

transform, described in section 2.3 , in order to compress the upper dynamic range relative to the lower dynamic range. The LCS pre-processing filter increases cross-correlation signal-to-noise ratio in the presence of strong particle image intensity changes between frames. The cross-correlation signal-to-noise ratio is also significantly affected by the flame luminosity. Chemiluminescence from the ethylene flame passes through the camera bandpass filter to reach values of 800-8,000 pxcounts depending on the seeding density. This disturbance is particularly severe in the second frame which is constrained by design to an exposure time of up to tens of milliseconds depending on the first frame read-out time. A moving average filter across 20 images is thus applied and each frame normalized by the corresponding average before the LCS filter. Lens flares from strong laser reflections off the facility walls are masked. The data set is then processed with the LaVision DaVis 8.4 cross-correlation algorithm. Instantaneous velocities are computed using multi-pass deformed interrogation windows down to 48x48 px, corresponding to a velocimetry resolution of 643  $\mu\text{m}$ . Median filters, correlation value thresholds, and outliers detection from temporal distributions remove spurious vectors. Adequate convergence in the velocity mean and RMS is ensured with sample sizes of 1,000 vectors or more. The turbulent kinetic energy (TKE) is estimated by taking the third RMS component as the average of the streamwise and transverse components. The actual three-components turbulent intensity (TI) would increase  $\text{o}(1)$  % while the TKE would decrease  $\text{o}(100)$   $\text{m}^2/\text{s}^2$  according to a parallel LES study by Nielsen (2019)). Uncertainties are computed for each instantaneous velocity vector using the measurement signal with the correlation statistics method by Wieneke (2015), and hardware specifications as detailed in section 2.4 . The RMS velocity is corrected by subtracting the random error fluctuations to isolate the flow fluctuations only (Sciacchitano and Wieneke, 2016).

Processing of the PLIF data is addressed next. The PLIF images are scaled down to 161  $\mu\text{m}/\text{px}$  and cropped to match the PIV vector spacing and PIV coordinates. The measurements spatial and temporal resolutions are respectively one and five orders of magnitude lower than the estimated Kolmogorov length and time scales. While turbulence spectrum clipping in high  $Re$  flows remains inevitable with the current technological capabilities, this effect is however mitigated for the investigation of turbulence-chemistry interactions: Poinso et al. (1991) noted that eddies smaller than on the order of the flame front thickness do not quench the flame due to viscous dissipation prior to the flame front. Previous work also demonstrated the dominance of large scale structures in

governing the cavity-stabilized combustion process (Xavier et al., 2016). The current PLIF technique can only provide qualitative measurements indicative of relative OH concentrations. It is however valuable to separate flow regions into reactants- and products-preponderant domains (Cantu et al., 2016b). An image processing algorithm has been developed to accurately contour the reactants domain; details may be found in Geipel et al. (2019). The image is binarized with ones mapping the product domains. The pair is multiplied with the corresponding instantaneous velocities field to output conditional velocities for both combustion products and reactants (figure 4.2). Statistics are finally extracted from the two stacks of velocity fields. The mean transverse velocities across a straight line at  $Y/H=0$  between the cavity leading and trailing edges, i.e.  $X/H=0$  and  $X/H=6$ , is taken as a representation of the species flux out of the cavity. Mean transverse velocities are similarly estimates at the flame front. The mean local flame angle relative to the local flow angle is estimated using the flame front angle relative to the tunnel cartesian coordinate system of figure 4.1, from which the local velocity vector angle is subtracted to output the mean relative flame angle.

In the following figures, CLE refers to Cavity Leading Edge. The tunnel wall opposite to the flameholder is represented with the continuous line at  $Y/H = 4.8$ . A sub-sample of average velocity vectors are displayed with white arrows to show flow directionality. Streamlines in purple originate from each vector. The flame intermittency obtained from PLIF indicates the fraction of instantaneous measurements in which a significant amount of OH is present and is shown as overlaid white contours. On line plots, error bars indicate 95% confidence intervals; the dotted line indicates the flame intermittency.

## 4.3 Statistical results

Statistical results are presented first in order to identify the key flow features, flame topology, and fluctuations over an ensemble of measurements. The mean and fluctuating statistics on the velocimetry presented below are first correlated with the mean PLIF signal. Conditional velocity means compute the means for reactants or products independently based on the instantaneous absence or presence of OH. As will be discussed below, independent PIV and PLIF statistics agree well with previous studies with separate acquisitions (Kirik, 2017; Tuttle et al., 2014) while new insights about cavity dynamics are gained from the combined nature of the measurements.

### 4.3.1 Mean velocities

The axial mean velocity component is displayed in figure 4.4a. Uncertainties for a 95% interval are provided in the captions. The duct flow velocimetry above the cavity ( $Y/H > 0$ ) is very similar in trends and values to the inflow to the cavity, (see section 3.4), characterized by the opposite wall boundary-layer spanning most of the duct height. This boundary-layer merges with the thin shear-layer created at the cavity leading edge; the peak axial mean velocity of 360 m/s is located at  $Y/H \sim 0.75$  and drops to 100-200 m/s at  $Y/H=0$ . Figure 4.4b displays the transverse mean velocities map. Transverse means are negative in the main duct flow on the order of 1 m/s and become nil or positive in the vicinity of the cavity between  $Y/H \sim 1.5 - 0.5$ . They sharply drop into negative values in the shear layer. Along the shear layer, transverse velocities remain negative and further decrease with increasing distance from the CLE, with the exception of the region nearest to the CLE where transverse velocities are slightly positive. The nil transverse velocity point is raised above the cavity interface as the flow goes further downstream in a trend similar to the maximum gradient in axial velocities, indicating a broadened or lifted shear layer starting at about  $X/H=3$ . The shear layer impinges on average onto the cavity ramp, forming a closed cavity flow as observed on larger geometries (Kirik, 2017).

The cavity mean velocities are characterized by flow re-circulation, permitting the generation of a chemical radical pool for flameholding. The cavity axial velocities are in the range  $\pm 50$  m/s (figure 4.4a) and the transverse velocities  $\pm 30$  m/s (figure 4.4b). Streamlines in figure 4.4c highlight an elliptical recirculation region with a major axis intersecting with the CLE and a point on the ramp

located at  $Y/H=-0.75$  and  $X/H=4.25$ . This axis coincides with the directionality of PLIF contours in this region. In addition, the center of the ellipse, located at  $Y/H=-0.5$  and  $X/H=2.5$ , coincides with the half-ellipse of the flame intermittency where the 100% flame presence probability indicates the region of constant flameholding. Thus mixing and combustion occurs in the first half of the elliptical recirculation zone, from the CLE side to the ramp side, and the second half re-circulates a constantly-present pool of combustion products and radicals. As will be discussed later in this chapter, in instantaneous measurements, two large re-circulation eddies are actually present in the cavity; the combination of two translating clockwise-rotating eddies lead to the observed elliptical streamlines when averaged over time.

The temporal sample size distribution of the velocimetry (see the contours in figure 4.4d) displays a strong correlation with the flame intermittency. This correlation may indicate bias towards reactants velocimetry in regions of mixed products and reactants. This bias would be due to relatively frequent loss of signal in the challenging conditions of product regions as observed in instantaneous measurements. Conditional velocities demonstrate the absence of bias by plotting the proportion of the product velocimetry sample size relative to the total sample size (figure 4.4e). The latter is found to closely follow the flame intermittency field. In conclusion, the bias in the velocimetry of the products relative to the reactants is not present. This observation further stresses the need for combined PIV-PLIF to assess each species statistics independently.

### 4.3.2 Fluctuations

Figure 4.5 display the field of the velocity RMS, representative of flow fluctuations. RMS values remain unaffected in the flow above the shear layer relative to the inflow values measured at  $X/H=-1.6$  presented in section 3.4. The main duct flow shows turbulent anisotropy with  $U_{y, RMS} \in [30 - 35]$  m/s and  $U_{x, RMS} \in [50 - 55]$  m/s at  $Y/H=2.5$ . The axial RMS, indicative of mixing with the main flow, are highest in the shear layer and lowest in the upstream cavity corner. Peak values are found past  $X/H=3$  above the cavity regions, hinting at disrupting product ejection events as observed in instantaneous PLIF measurements. A large region of heightened transverse RMS velocities coincides with the upper half of elliptical recirculation region previously described. Shear layer impingement locations are put in evidence with the peak transverse RMS velocity in the impingement area on the ramp, in agreement with previous observations (Kirik, 2017). Similarly to the axial RMS, the

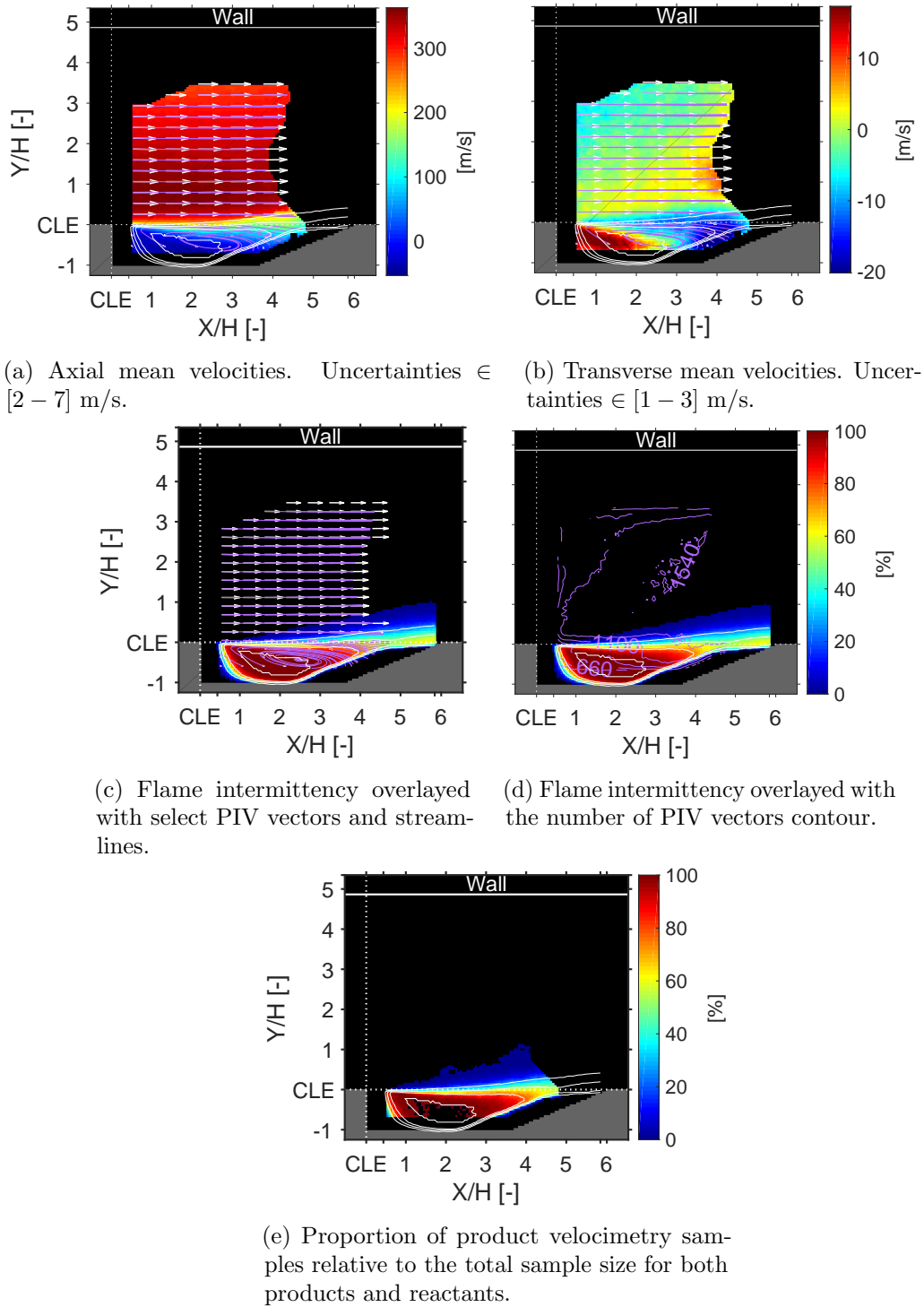


Figure 4.4: Mean velocities and flame intermittency for a flow Mach number of  $M = 0.66$  and a global ethylene equivalence ratio of  $\Phi_g = 0.47$ .

transverse RMS drops in the cavity upstream corner where a small low-speed re-circulation region was identified in a larger cavity (Kirik, 2017). Based on observations from Kirik (2017), this portion

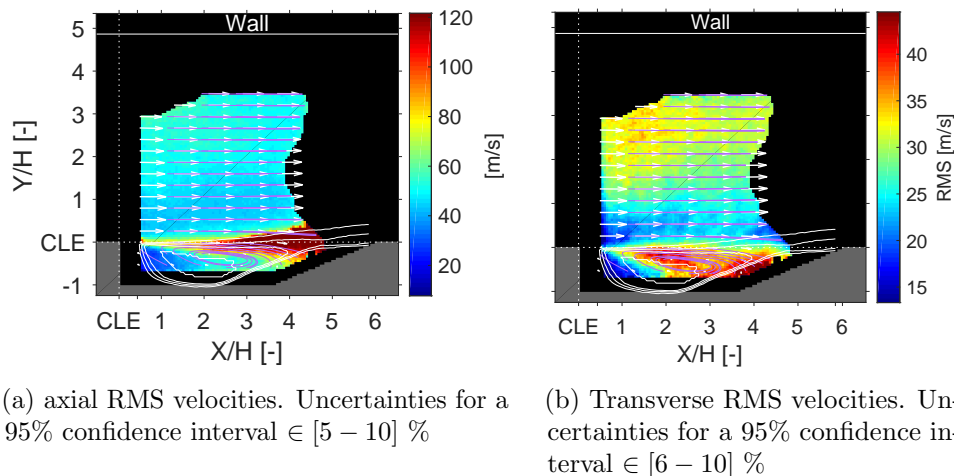
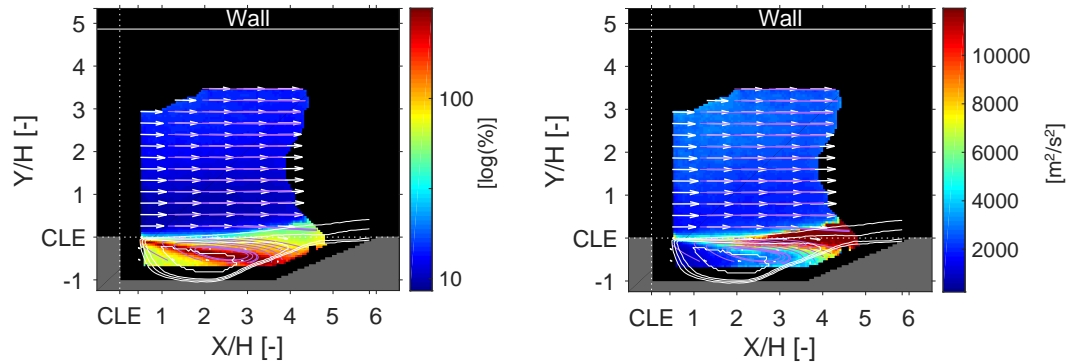


Figure 4.5: RMS velocity components for a flow Mach number of  $M = 0.66$  and a global ethylene equivalence ratio of  $\Phi_g = 0.47$ .

of the cavity is expected to be filled by hot, burned gases that are forced toward the front of the cavity by the re-circulation process. These gases provide an ignition source as for the fresh fuel-air mixture as they are entrained by the main recirculation zone into the cavity shear layer.

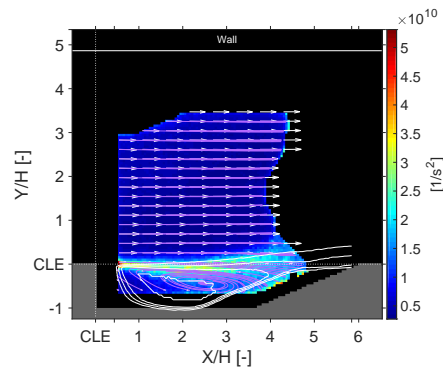
The turbulence intensity (figure 4.6a) displays a strong increase along the elliptical recirculation region axis, corresponding to the regions of highest flow curvature. Values exceeding 200% are detected in those areas, versus the main duct flow values of 10-15%. In contrast, the turbulent kinetic energy follows the trends of the axial fluctuations, i.e. with high values in the shear layer and a peak in the regions of product ejection. Uncertainties for the turbulence intensity are  $\sim 4\%$  in duct flow and  $< 10\%$  in cavity (except on the elliptical re-circulation zone axis).

The swirling strength of vortices allows the localization of the strongest eddies independently of the reference frame (Adrian et al., 2000). Its spatial distribution reveals concentrated high values at the cavity leading edge where the shear layer forms. As the axial distance from the leading edge increases, the swirling strength decreases and spreads into the cavity due to a combination of shear layer flapping and broadening, as well as increased viscosity. Despite the clearly observed re-circulation region located in the cavity, the swirling strength map gives no indication of such structure. This is indicative of unsteady large eddies in the cavity shifting within a range of locations. Overall, the cavity flow dynamics are evidenced as unsteady and will be further investigated in section 4.4.



(a) Turbulent intensities. Uncertainties  $\sim$  4% in duct flow.

(b) Turbulent Kinetic Energy. Uncertainties for a 95% confidence interval  $\in [6.5 - 10]$  %



(c) Swirling strength averaged over time.

Figure 4.6: Fluctuation energy indicators for a flow Mach number of  $M = 0.66$  and a global ethylene equivalence ratio of  $\Phi_g = 0.47$ .

### 4.3.3 Conditional velocities

Conditional velocities are a core benefit of combined PIV-PLIF. By separating the velocity field into product and reactant velocities, deeper insights into the combustion dynamics may be gained. Figure 4.7 shows the mean absolute and relative conditional velocities with overlaid flame intermittency contours in white and mean unconditional streamlines in purple.

In general, the flow topologies between products and reactants are very similar. Both the axial and transverse values and trends are comparable (see figures 4.7a-4.7d), with the notable exception of the product transverse velocities above the cavity interface: products escaping the cavity and shear layer are entrained into the duct flow with a significant transverse component relative to the main flow. Transverse velocities are negative for both the products and reactants in regions of flame presence (figures 4.7c and 4.7d). The similarities between the products and reactants flow topologies prompted the calculation of relative mean velocities of figures 4.7e and 4.7f, i.e. the mean product

velocities relative to the reactants. Both the axial and transverse mean relative velocities indicate a counter-flow on the order of 1-10 m/s driving the combustion kinetics, whereby reactants flow into products regions to ignite, transform into products, and expand against incoming premixed flow.

Mass transfer rates in and out of cavity are a quantity of interest. The mass flux requires knowledge of the area (vector spacing multiplied by the laser sheet thickness) and the density, unavailable from the present measurements. Nonetheless, the direction of mass transfer may be suggested by means of the average transverse velocity at the cavity interface at  $Y/H=0$ , shown in figure 4.8a. Both the products and reactants are on average flowing into the cavity with the exception of the region closest to the CLE, where velocities are nil. The hidden region past  $X/H=5$  is expected to follow the increasing trend seen between  $X/H=4-5$  in figure 4.8a such that the mean transverse flux along the entire cavity interface equals zero according to the mass conservation principle. This demonstrates that while mass transfer into the cavity and combustion does occur in the shear layer, mass transfer out of the cavity likely occurs further downstream, near the ramp. It should however be noted that the measurement is two-dimensional and would not take into account any spanwise flow. Relating this to the 60% flame intermittency at the downstream end of the cavity interface (see figure 4.4c) hints at disrupting ejection events that compensate for the mass and heat accumulated over the remaining 40% of the time. This is further supported by the wide amplitude between the minimum and maximum transverse velocities detected at the cavity interface. The cavity mass exchange is therefore unbalanced: steady inflow of reactants and re-circulation of products occurs most of the time. This build-up would lead to a large ejection from the downstream end of the ramp over a short time. A first estimate on the product transverse velocities at the shear-layer flame front is computed by extracting the transverse velocities at each axial location along the flame front and averaging them across time. The mean flame front velocities presented in figure 4.8b are also systematically negative except at the most upstream locations, where the flame is fully contained within the cavity. The flame is therefore on average trapped inside the cavity. Ensemble-statistics however do not allow further investigation into the disrupting ejection events suggested by the above results. In the following section, the problem is further studied using instantaneous measurements.

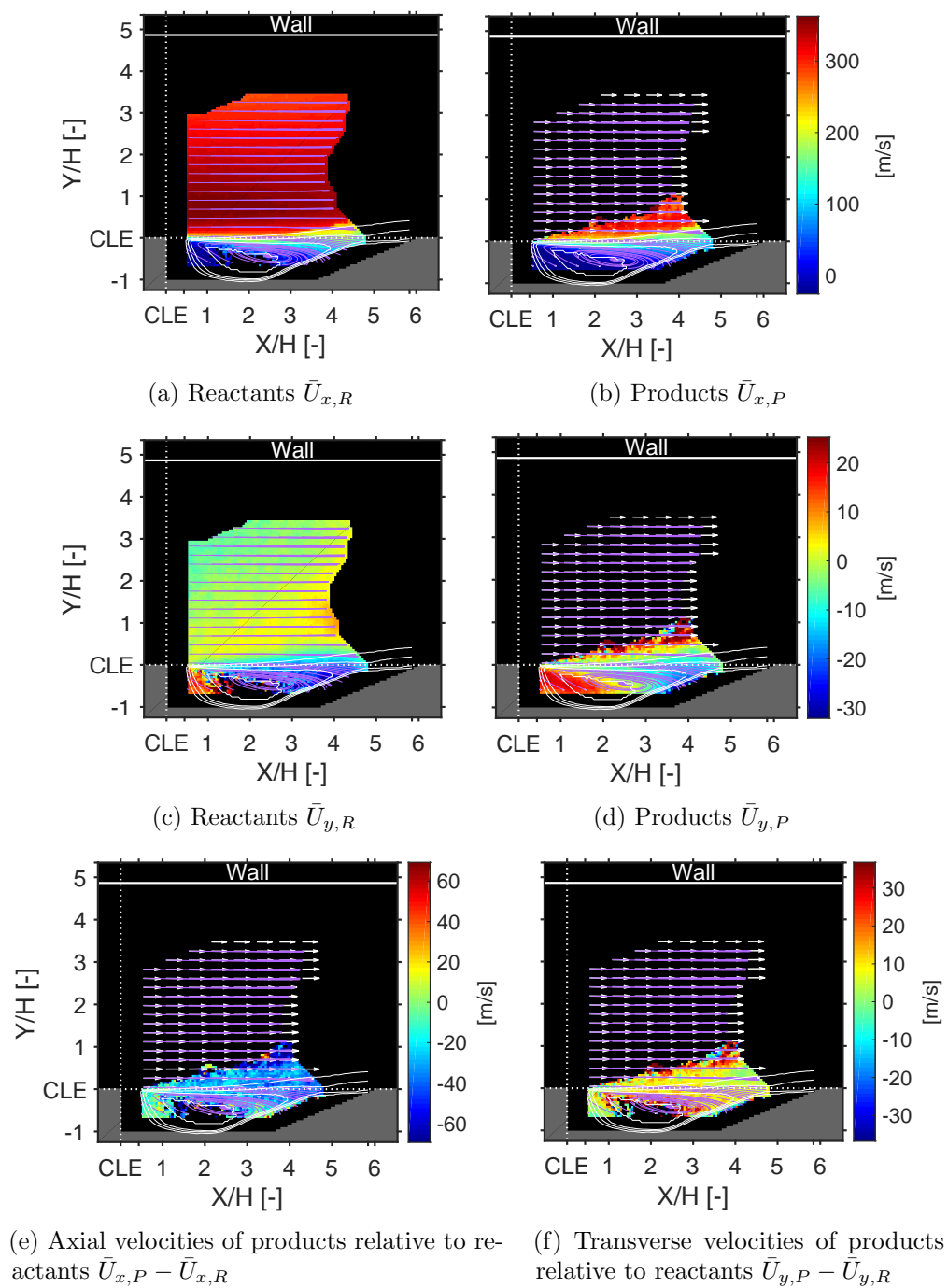


Figure 4.7: Mean conditional velocity fields.

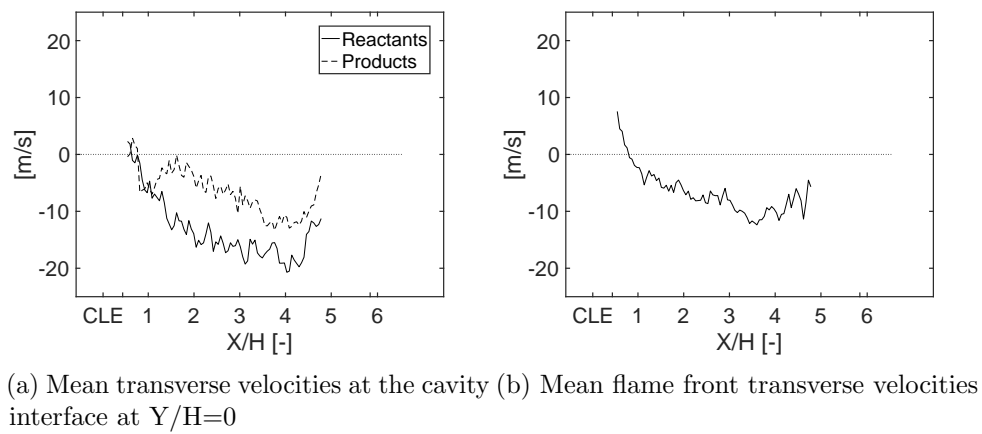


Figure 4.8: Mean transverse velocities through select boundaries (cavity interface or flamefront), indicative of mass flux.

## 4.4 Combustion dynamics

Indications of an unsteady process in the velocimetry statistics and flame intermittency motivated a closer investigation of the instantaneous measurements. The combined PIV and PLIF fields may be used as complementary inputs to each other to gain insights into the turbulence-chemistry interactions. Randomly-sampled periodic patterns of the OH structures are observed throughout the dataset, which may be sorted into three main states: (i) the flame is contained within the cavity before the ramp ( $Y/H < 0$  and  $X/H < 4$ ); (ii) the flame continuously extends past the cavity interface and ramp; (iii) the extended flame is discontinuous. The three states support the previously-stated hypothesis of a combustion oscillation possibly coupled with the shock-train and thermal throat (Allison et al., 2017; Kirik, 2017; Tuttle et al., 2014; Wang et al., 2014). The combustion cycle suggested in the following would consist of intermittent combustion product ejection by means of shear-layer detachment from the cavity ramp. A selection of instantaneous measurements illustrating the above three categories and transitions between them is displayed in figure 4.9. For all three states, the cavity flame closely abides by the shear layer, wrinkles around the shear-layer eddies (identified by high swirling strength values in figure 4.11), and is either continuous or split in two. The shear-layer eddies serve to exchange combustion radicals generated in the cavity with the fresh premixed flow from the duct. These eddies are of similar size to eddies found in the free stream (figure 4.11). In addition, large scale free stream fluctuations are observed in the streamlines and vectors of figures 4.9 and 4.11. Measurements with the shear layer impinging on the cavity ramp are correlated with a negative transverse momentum of the free stream flow in the cavity vicinity. The above observations suggest that spatial scales in the cavity flame are coupled with the free stream scales.

Allison et al. (2017) demonstrated the presence of a combustion oscillation at 340 Hz in a similar dual-mode scramjet flowpath with a cavity flameholder using 50 kHz CH\* chemiluminescence. These authors attributed the oscillation to thermo-acoustic waves between the shock train and flame front. They also located the greatest variations in heat release in the region of the upper flame brush surface. The measured 340 Hz frequency is close to the 357 Hz oscillation frequency detected in the companion LES (Ramesh et al., 2018). Evidence of a similar oscillation is observed in LES applied to the present flowpath (Nielsen, 2019), where periodic flame structures ejected from the cavity can

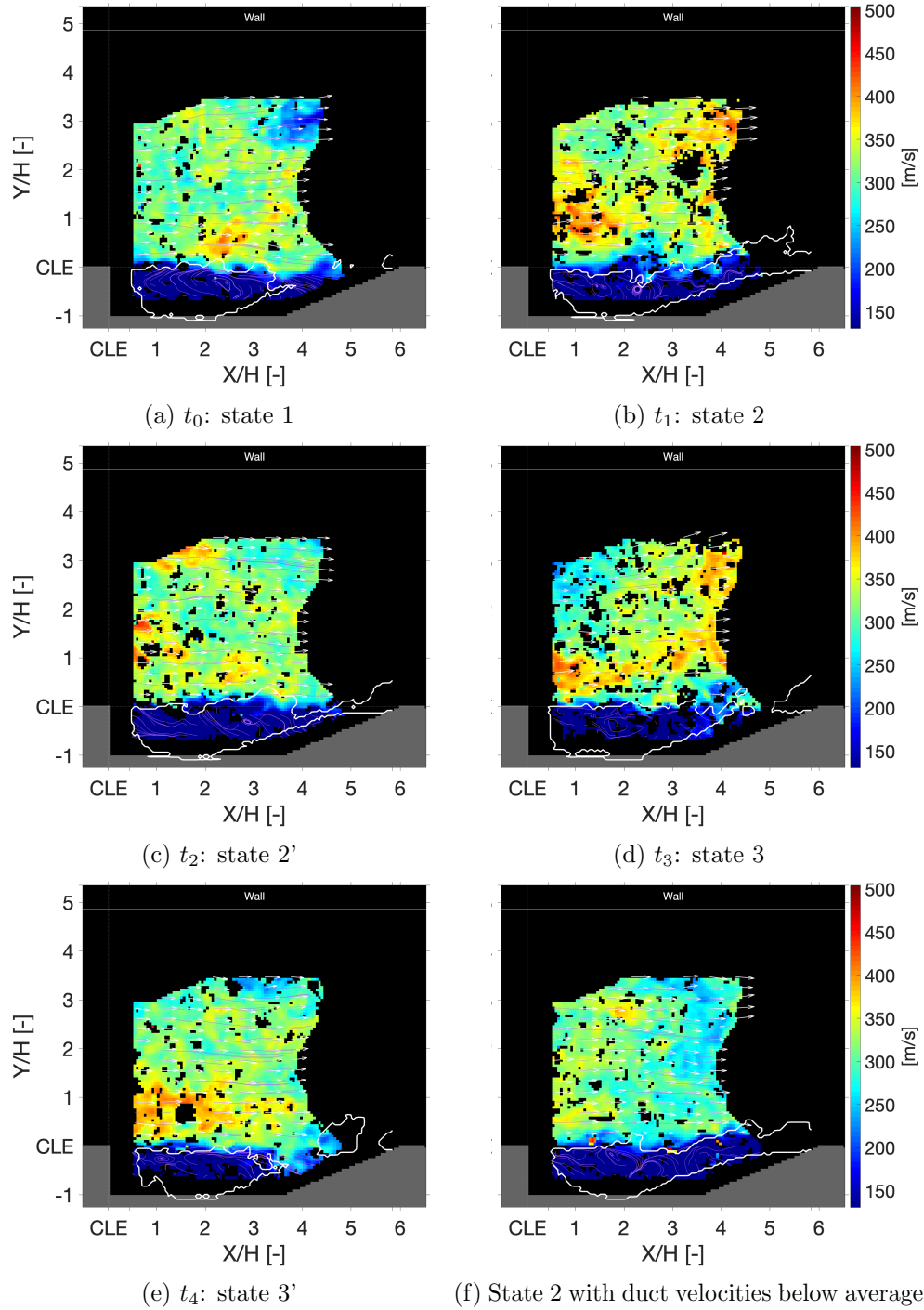


Figure 4.9: Select instantaneous PIV-PLIF frames.

also be observed. It is therefore expected that the present flow is subject to at least one dominant thermo-acoustic oscillation between the shock train and flamefront, or more (e.g. pseudo-shock oscillations and self-sustained cavity oscillations, see Matsuo et al. (1999) and Wang et al. (2014)).

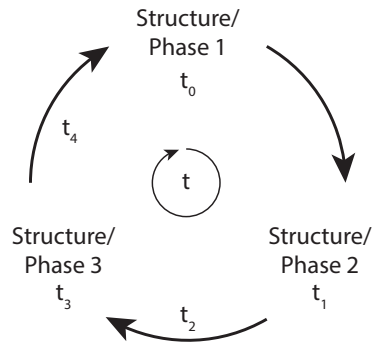


Figure 4.10: Diagram of the hypothetical combustion cycle. Time indices correspond to those of figures 4.9a-4.9e.

The present PIV-PLIF acquisition frequency of 10 Hz does not permit the re-construction of cyclical combustion patterns on the order of 100-1000 Hz. However, a hypothesis on the cyclical process may be made based on the identification of categories of instantaneous PIV-PLIF measurements. Given that the combustion oscillation frequency is most likely not a harmonic of the PIV-PLIF acquisition frequency, one may assume that most of the combustion cycle is randomly captured over the available 1,000 measurements. With the additional input of the flow directionality, theoretical physics, and the previous investigations on cavity flows listed in the introduction, the categories of instantaneous measurements may be sorted in a most likely order to suggest a hypothetical cycle as presented in the following. Additional investigations would be required to confirm the cycle and the sequence of phases described below as will be suggested in the conclusion.

The hypothetical cycle consists of three typical flow states: a cavity-enclosed flame (phase/state 1), a stretched flame extending past the cavity ramp and interface (phase/state 2), which subsequently leads to the ejection of products (phase/state 3). This order is illustrated in figure 4.10 corresponding to the sequence of figures 4.9a to 4.9e. Permutations into alternative orders would be in contradiction with fundamental combustion principles and previous conclusions on hydrocarbon-fueled cavity flows. The phase series 2-1-3 would imply that the extended part of the flame extinguishes before a separated flame self-ignites in the main duct flow. The phase series 3-2-1 would have the separated flame self-ignite in the duct flow and propagate against the high-speed flow to connect with the upstream cavity flame. Thus the phase order 1-2-3 is retained for the following analysis.

In phase 1 (figure 4.9a), the cavity gases are contained within the cavity by the duct flow high

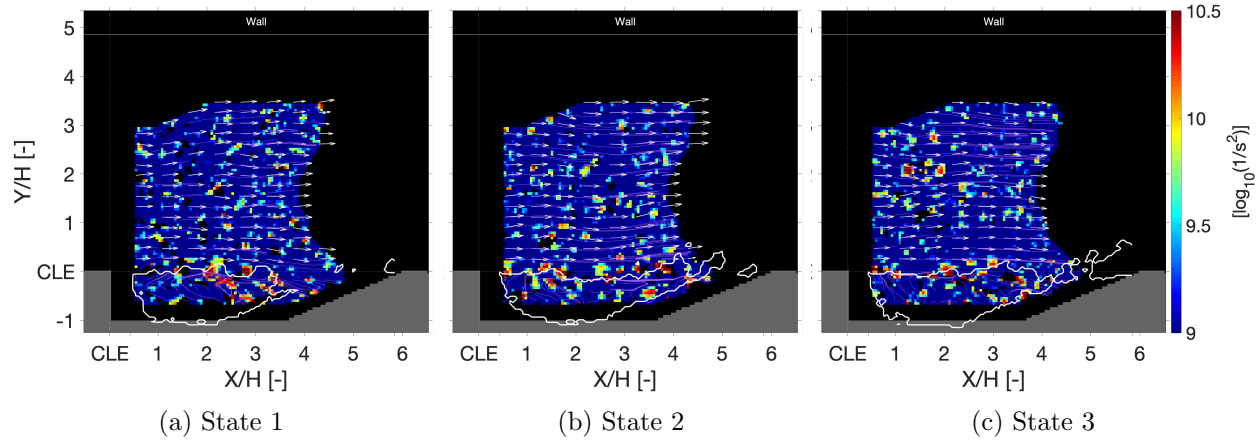


Figure 4.11: Select instantaneous swirling strength.

momentum, leading to shear layer impingement on the cavity ramp. The cavity re-circulation zone consists of two large clockwise vortices, expected to grow from the merging of smaller eddies formed at the impingement location (Kirik, 2017; Tuttle et al., 2014). Mass exchange between the duct flow and the cavity flow is lower as it occurs mostly through the shear layer rather than along the ramp, as discussed in section 4.3.3. Generated heat is thus mostly stored in the cavity by the trapped re-circulation zone. During this flow state, some heat may escape at the shear layer impingement zone along the ramp (hidden to the PIV-PLIF cameras due to setup constraints) but low flame intermittency near the trailing edge and instantaneous PLIF signals suggest this heat transfer to be a secondary flame-holding process.

Phase 1 is unsustainable due to the mass and heat accumulation into the cavity. The shear layer is subsequently lifted (figure 4.9b) and detaches from the cavity ramp. An open question is whether this event may be triggered by reaching a threshold in the cavity pressure and gas expansion, or by large-scale flow fluctuations from e.g. shock train fluctuations. The lifted shear layer provides an escape route for the trapped gases in the form of a sudden event (phase 2). During this event, combustion radicals and products are ejected through a narrow streamtube between the ramp and the lifted shear layer. The ejection event leads to a sudden transfer of heat and mass from the cavity to the duct while stretching the reaction front. The flamefront is stretched thinnest between the two large recirculation eddies, leading to local extinction (figure 4.9d). The above events constitute phase 3. Transition back to phase 1 occurs as the downstream eddy is convected away into the main flow (figure 4.9e). The shear layer attaches itself back to the ramp, trapping combustion products

and radicals back into the cavity. Time-resolved measurements would provide additional insights into the behavior of the remaining eddy. The pressure rise at the reattachment point may shift the upstream eddy towards the cavity leading edge, and a new eddy is formed from the merging of eddies created at the impingement as suggested by Tuttle et al. (2014). Alternatively, a new eddy may be formed at the near cavity leading edge and the eddy from the previous cycle will be ejected next.

The above process may be directly related to thermoacoustics between the shock train and the flame or independent. The presence of both positive and negative velocity fluctuations  $U' = U - U_{AVG}$  for a same phase, e.g. phase 2 in figure 4.9f versus 4.9b, suggests a repetition of the cavity combustion cycle within one shock train cycle. Thorough investigations with high-frequency pressure measurements and LES are warranted to explore the driver of the observed cavity combustion oscillation. While hypothetical, the combustion oscillation cycle proposed above may lead to answers about the unsteady flow and combustion dynamics observed experimentally and in CFD simulations. The presence of one or more oscillations in a complex system such as a scramjet combustor makes it prone to chaotic behavior in the case of a trigger event. In particular, the cause for rare events during experiments such as sudden flame-outs remain unidentified. Other phenomena may be related to combustion oscillations, such as difficulties in igniting the cavity flame or sustaining it at low equivalence ratios. A critical implication concerns scramjet propulsion systems. With a better understanding of the mechanisms behind combustion unsteadiness, new geometries or active/passive dampeners may be designed for reliable and efficient combustion and operation.

## 4.5 Conclusion

The first combined PIV-PLIF measurements in a dual-mode scramjet combustor are presented, giving unprecedented insight into the turbulence-chemistry interactions and providing the first experimental database on a DNS-friendly dual-mode cavity flameholder. The cavity flow is characterized by an unsteady shear layer and a re-circulation zone hosting two large eddies. Combustion intermittency above and downstream of the cavity interface is evidenced by low flame presence probability as well as negative transverse velocities for products and reactants at the cavity interface. A cyclical combustion behavior in single- and dual-mode premixed scramjet open-cavity flows has been suggested in previous experimental and numerical work. PIV-PLIF images are thus categorized by common flamefront traits and sorted based on the companion velocimetry and fundamental combustion principles. A cycle is suggested, starting with a trapped vortex accumulating mass and heat into the cavity. This unsustainable flow state triggers the sudden detachment of the shear layer from the cavity ramp followed by the ejection of combustion products. As the cavity-contained mass and heat decrease and the flame is stretched thin, the flame is split in two and the downstream re-circulation eddy is shed into the duct flow. The shear layer re-attaches and resets the cavity to a trapped vortex configuration. These observations are consistent with previous work on different cavity flows and trends in non-simultaneous PIV-PLIF statistics. Complementary investigations are needed to better understand the combustion dynamics and their potential to grow into instabilities. Experimental work on the order of 10-100 kHz would potentially resolve the oscillations and may include pressure, PLIF, and laser Doppler anemometry (LDA) measurements. Large eddy simulations would also deliver valuable insights into the oscillations across wide temporal and spatial scales. Gaining understanding of dual-mode scramjet combustion dynamics may lead to innovative flameholder geometries and active/passive dampeners for operational scramjet propulsion systems.



# Conclusion

## Summary

New experimental and diagnostic capabilities for hypersonic air-breathing propulsion ground testing were developed in this dissertation. A new flow configuration was created and analyzed with advanced measurement techniques, giving insights into the fundamental physics governing high-speed cavity-stabilized combustion and enabling future high-accuracy numerical studies.

The ground testing capabilities for high-enthalpy flows are first extended by the use of additive manufacturing. The latter allows for the transformation of the original direct-connect flowpath of the UVaSCF into a flowpath enabling semi-freejet testing. In essence, a host flowpath is developed for an immersed model with a miniature cavity flameholder. The mid-duct immersed model creates new boundary-conditions and includes a small-scale cavity to enable high-accuracy DNS computations. The resulting tunnel blockage and thermal loads are addressed with the use of contoured wall geometries and active convective cooling. Several design iterations stemmed from an inter-disciplinary collaboration including computational fluid dynamics, finite elements analysis, and in-situ testing. Trade studies were conducted until the new parts could sustain an ethylene flame for repeated extended cycles on the order of hours. Residual stresses and geometric distortion are highlighted as notable concerns. The final design consists of an Inconel 718 shell of 0.05 in. (1.27 mm) thickness with internal cooling loops throughout the flameholder. Repeated tests in the tunnel demonstrated that the concept met, or exceeded, design requirements: low tunnel blockage, resistance to cycles of thermal loads and structural stresses, ignition and flameholding, as well as access for optical and sensors-based diagnostics. The design is modular for operational flexibility and efficient fabrication. This work represents the first published methodology for the design

and fabrication of additively manufactured scramjet combustor components and opens up new opportunities e.g. advanced flameholder geometries. It also constitutes, to the author's knowledge, the longest test duration for an additively manufactured cavity flameholder under a flame in a Mach 5 enthalpy flow.

The adequate initialization of the direct numerical simulation requires the velocity field at the computational domain boundary to be measured at the highest resolutions achievable. The objective is to resolve the finer scales of turbulent flows at high subsonic Mach numbers for accurate boundary-conditions in DNS. The selected technique is Particle Image Velocimetry, which was recently successfully applied to scramjet cavity flows in other studies. A methodology is developed by anticipating, compensating, and characterizing the velocimetry. Measurements are enabled by a new processing scheme to bypass the elevated noise associated with higher PIV resolutions: a Logarithm-Contrast-Stretch filter is developed to compress the dynamic range in the higher intensities range, resulting in a very significant reduction in systematic cross-correlation errors. Uncertainties are quantified *a posteriori* based on the input images and resulting velocimetry; they are propagated into statistical quantities and fluctuations due to noise are removed from the total signal fluctuations. The methodology effectiveness is demonstrated with synthetic PIV and experiments conducted in a dual-mode scramjet combustor for which a velocimetry resolution of  $355 \mu\text{m}$  is first achieved. This also represents the first velocimetry for free stream seeded dual-mode scramjet flows thereby alleviating bias towards the seeded flow sub-domains.

The velocimetry of the inflow to a DNS-friendly cavity flameholder is subsequently accurately characterized and analyzed for its sensitivity to the shock train location and heat release rate to support the accurate numerical simulation of high-speed cavity-stabilized flames. While varying heat release does not affect the velocimetry statistics, varying the shock train location increases the RMS values between 10 and 35%. Key flow structures are identified, including stagnation points, boundary-layers, and pre-heat zones. The flowpath design is validated by the absence of flow spillage or separation at the cavity inflow plane. The present study represents the first velocimetry on an immersed model in a direct-connect facility and constitutes a reference for Direct Numerical Simulations on premixed turbulent flames in high-speed compressible flows with a large flow-normal flame velocity component.

The diagnostic capabilities are further developed with a combined PIV and hydroxyl (OH) planar

laser induced fluorescence technique, giving the first insights into the interactions between the flow and flame in a dual-mode scramjet combustor. The cavity flow is characterized by an unsteady shear layer and a re-circulation zone hosting two large eddies. Combustion intermittency past the cavity interface is evidenced by low flame presence probability in those regions as well as negative transverse velocities for products and reactants at the cavity interface. Pulsed combustion in single- and dual-mode pre-mixed scramjet open cavity flows has been demonstrated in previous experimental and numerical work. PIV-PLIF images are thus categorized by common flamefront traits. The three resulting flow states are ordered using the corresponding velocimetry and fundamental combustion principles. A hypothetical combustion cycle is thus suggested, starting with a trapped vortex accumulating mass and heat into the cavity. This unsustainable flow configuration triggers the sudden detachment of the shear layer from the cavity ramp followed by the ejection of combustion products. As the cavity-contained mass and heat decrease and the flame is stretched thin, the flame is split in two and the downstream re-circulation eddies is shed into the duct flow. The shear layer re-attaches and resets the cavity to a trapped vortex configuration. These observations are consistent with previous work and trends in non-simultaneous PIV-PLIF statistics. Pulsed combustion is of critical relevance for operational scramjet propulsion systems, which require stable combustion. Gaining understanding of combustion unsteadiness may lead to innovative flameholder geometries and active/passive dampeners. Subsequent work may draw from this study to further investigate the flow and combustion unsteadiness, design solutions to control them, and use the additive manufacturing methodology to manufacture complex designs.

## Recommendations for Future Research

The extraordinary complexity of the combustor flow in the UVaSCF warrants the investigation of many unanswered questions. First, a key question is the significance of spanwise flow in the cavity dynamics. Tomographic PIV and chemiluminescence may provide insights on the validity of the primarily two-dimensional flow hypothesis used in experiments so far. Other benefits of tomographic PIV include high resolution measurements in the third dimension, alleviation of errors from out-of-plane velocity gradients, and 3D spatial correlations of turbulence and vortex identification based on Q-criterion. The method is however associated with high experimental complexity and

computational cost. Second, the unsteadiness cycle suggested above requires additional investigations to confirm its pattern. A proposed next step is to repeat the experiment with synchronized high-speed chemiluminescence at 50 kHz or more to resolve the cycle while having the knowledge of the instantaneous flame structure and flow velocities. Alternatives include chemiluminescence, OH-PLIF, and pressure measurements at 10-100 kHz to fully resolve the unsteady process. kHz PIV is particularly difficult to attain and typically incurs spatial resolution trade-offs. 10 Hz PIV can nonetheless be used by comparing kHz PLIF outputs to the present PLIF dataset. The present combined PIV-PLIF data could then be robustly sorted into the same order to confirm the above hypotheses. Higher resolutions could also be achieved with the use of longer focal length lenses on both the PIV and PLIF camera. Higher resolutions in the velocimetry would refine the correlation between the instantaneous flame structure and the velocity field, in particular the swirling strength. Third, with the pulsed combustion characterized, new solutions for stable combustion may be designed. For example, new geometries for the stable establishment of flow states 1 or 2 (see figure 4.9) may be tested, e.g. a backward-facing step of angle lower than 90 degrees to force the lifted shear-layer configuration, a trapped-vortex configuration with continuous bleeding of the pool of radicals and downstream injection, or a variable geometries in the spanwise dimensions transitioning from a trapped vortex configuration to a lifted shear layer configuration.

Moreover, neglected sources of measurement error require additional attention as the accuracy requirements become more critical, e.g. due to parallel DNS studies. Velocity errors from density gradients have been reasonably neglected in the present work. Increasing the imaging lens magnification further would however amplify optical distortions caused by density gradients in the flow. Elsinga et al. (2005a) noted that "since both the velocity error and particle image blur are related to the second derivative of the refractive index field, it is expected that the analysis of particle image blur can be used to provide quantitative information on the velocity error related to aero-optical distortion. In that case background oriented Schlieren measurements and 2D flow assumption will not be necessary, which deserves further attention and research." This approach would enable further increases in velocimetry spatial resolution to capture finer turbulent scales.

Finally, the present work on improving diagnostics capabilities could be further developed. In particular, a hybrid method using the LCS pre-processing filter to identify the correct peak and the conventional cross-correlation without pre-filtering would alleviate systematic errors from

brightness variations and decrease sensitivity to low seeding densities, while retaining the low uncertainties of the un-filtered image pair cross-correlation map. Another idea leverages flake tumbling for a new concept of “pulsed” streak velocimetry. Assuming measurement conditions similar to those required for Particle Tracking Velocimetry (PTV, Schanz et al. (2016)) but with longer illumination/exposure times, the oscillating particle brightness would draw a streak of oscillating pixel intensities onto the camera sensor. With prior knowledge about the temporal oscillation function, e.g. a sinusoidal function of known frequency, the two-dimensional streak and its spatial oscillation may be transformed into a high-frequency temporal displacement function and subsequently a temporal velocity function. Initial computations estimate the potential temporal sampling frequency with the hardware used in this dissertation at 25 MHz, versus 10 Hz in this work and up to 10 kHz in the literature.



# Bibliography

- Adrian, R. J., K. T. Christensen, and Z.-C. Liu  
2000. Analysis and interpretation of instantaneous turbulent velocity fields. *Experiments in Fluids*, 29(3):275–290.
- Allison, P. M., K. Frederickson, J. W. Kirik, R. D. Rockwell, W. R. Lempert, and J. A. Sutton  
2017. Investigation of supersonic combustion dynamics via 50 kHz CH chemiluminescence imaging. *Proceedings of the Combustion Institute*, 36(2):2849–2856.
- Anderton, J.  
2017. 3D metal printing enables hypersonic propulsion breakthrough. [retrieved 4 July 2018].
- Ben-Yakar, A. and R. K. Hanson  
2001. Cavity flame-holders for ignition and flame stabilization in scramjets: An overview. *Journal of Propulsion and Power*, 17(4):869–877.
- Berridge, D. C., G. McKiernan, T. P. Wadhams, M. Holden, B. M. Wheaton, T. D. Wolf, and S. P. Schneider  
2018. Hypersonic ground tests in support of the boundary layer transition (bolt) flight experiment. AIAA 2018-2893.
- Cantu, L. M. L., E. C. A. Gallo, A. D. Cutler, B. F. Bathel, P. M. Danehy, R. D. Rockwell, C. P. Goyne, and J. C. McDaniel  
2016a. Visualization of simulated fuel-air mixing in a dual-mode scramjet. *Journal of Propulsion and Power*, 32(2):373–382.
- Cantu, L. M. L., E. C. A. Gallo, A. D. Cutler, P. M. Danehy, R. D. Rockwell, C. T. Johansen, C. P. Goyne, and J. C. McDaniel  
2016b. OH PLIF visualization of a premixed ethylene-fueled dual-mode scramjet combustor. AIAA 2015-0355.
- Chen, F. and H. Liu  
2018. Particle image velocimetry for combustion measurements: Applications and developments. *Chinese Journal of Aeronautics*, 31(7):1407–1427.
- Conner, B. P., G. P. Manogharan, A. N. Martof, L. M. Rodomsky, C. M. Rodomsky, D. C. Jordan, and J. W. Limperos  
2014. Making sense of 3D printing: Creating a map of additive manufacturing products and services. *Additive Manufacturing*, 1–4:64–76.
- Cooper, M.  
2018. Air force looking to additive manufacturing to expand hypersonic flight capabilities. [retrieved 4 July 2018].

- Cutler, A. D., E. C. Gallo, L. M. Cantu, R. D. Rockwell, and C. P. Goynes  
2018. Coherent anti-stokes raman spectroscopy of a premixed ethylene-air flame in a dual-mode scramjet. *Combustion and Flame*, 189(Supplement C):92–105.
- Cutler, A. D., G. Magnotti, L. Cantu, E. Gallo, R. Rockwell, and C. Goynes  
2014. Dual-pump coherent anti-stokes raman spectroscopy measurements in a dual-mode scramjet. *Journal of Propulsion and Power*, 30(3):539–549.
- Dellenback, P. A., J. Macharivilakathu, and S. R. Pierce  
2000. Contrast-enhancement techniques for particle-image velocimetry. *Applied Optics*, 39(32):5978.
- Dominik, E. and C. Noel  
2016. Simultaneous high-speed 3D flame front detection and tomographic PIV. *Measurement Science and Technology*, 27(3):035303.
- Elsinga, G. E., B. W. van Oudheusden, and F. Scarano  
2005a. The effect of particle image blur on the correlation map and velocity measurement in PIV. In *Optical Diagnostics*, L. M. Hanssen and P. V. Farrell, eds. SPIE.
- Elsinga, G. E., B. W. van Oudheusden, and F. Scarano  
2005b. Evaluation of aero-optical distortion effects in PIV. *Experiments in Fluids*, 39(2):246–256.
- Fischer, A.  
2017. Imaging flow velocimetry with laser mie scattering. *Applied Sciences*, 7(12):1298.
- Foley, C. W., I. Chterev, J. Seitzman, and T. Lieuwen  
2015. High resolution particle image velocimetry and CH-PLIF measurements and analysis of a shear layer stabilized flame. *Journal of Engineering for Gas Turbines and Power*, 138(3):031603–031603–13.
- Frazier, W. E.  
2014. Metal additive manufacturing: A review. *Journal of Materials Engineering and Performance*, 23(6):1917–1928.
- Gamba, M., N. T. Clemens, and O. A. Ezekoye  
2013. Volumetric PIV and 2D OH PLIF imaging in the far-field of a low Reynolds number nonpremixed jet flame. *Measurement Science and Technology*, 24(2):024003.
- Geipel, C. M., D. A. Lieber, V. G. Awate, R. D. Rockwell, H. K. Chelliah, and A. D. Cutler  
2019. Characterization of flame front shape in a dual-mode scramjet. AIAA.
- Geipel, C. M., R. Rockwell, H. Chelliah, A. D. Cutler, C. Spelker, Z. Hashem, and P. M. Danehy  
2017. High-spatial-resolution OH PLIF visualization in a cavity-stabilized ethylene-air turbulent flame. AIAA 2017-3901.
- Gendrich, C. P., M. M. Koochesfahani, and D. G. Nocera  
1997. Molecular tagging velocimetry and other novel applications of a new phosphorescent supramolecule. *Experiments in Fluids*, 23(5):361–372.
- Gharib, M. and A. Roshko  
1987. The effect of flow oscillations on cavity drag. *Journal of Fluid Mechanics*, 177(-1):501.

- Goyne, C., J. McDaniel, R. Krauss, and S. Day  
2001. Velocity measurement in a dual-mode supersonic combustor using particle image velocimetry. In *International Space Planes and Hypersonic Systems and Technologies Conferences*. American Institute of Aeronautics and Astronautics.
- Gradl, P. R.  
2016. Rapid fabrication techniques for liquid rocket channel wall nozzles. AIAA 2016-4771.
- Gradl, P. R., S. E. Greene, C. Protz, B. Bullard, J. Buzzell, C. Garcia, J. Wood, R. Osborne, J. Hulka, and K. G. Cooper  
2018. Additive manufacturing of liquid rocket engine combustion devices: A summary of process developments and hot-fire testing results. AIAA 2018-4625.
- Gruber, M. R., R. A. Baurle, T. Mathur, and K.-Y. Hsu  
2018. Fundamental studies of cavity-based flameholder concepts for supersonic combustors. *Journal of Propulsion and Power*, 17(1):146–153.
- Harbaugh, J.  
2017. Nasa tests 3-d printed rocket part to reduce future sls engine costs. [retrieved 2 July 2018].
- Heiser, W., D. Pratt, D. Daley, and U. Mehta  
1994. *Hypersonic Airbreathing Propulsion*. American Institute of Aeronautics and Astronautics, Inc.
- Horn, B. K. and B. G. Schunck  
1981. Determining optical flow. *Artificial Intelligence*, 17(1-3):185–203.
- Howison, J. C. and C. P. Goyne  
2010. Assessment of seeder performance for particle velocimetry in a scramjet combustor. *Journal of Propulsion and Power*, 26(3):514–523.
- Judson, J.  
2018. Orbital atk tests partially 3D printed warhead for hypersonic weapons. [retrieved 4 July 2018].
- Keane, R. D. and R. J. Adrian  
1990. Optimization of particle image velocimeters. part i. double pulsed systems. *Measurement Science and Technology*, 1(11):1202–1215.
- Kellner, T.  
2018. The blade runners: This factory is 3D printing turbine parts for the world’s largest jet engine. [retrieved 2 July 2018].
- Kidder, B.  
2018. 3D printed unit demonstrates one of longest duration propulsion wind tunnel tests on record. [retrieved May 10 2018].
- Kirik, J.  
2017. *Aerodynamics of a Scramjet Cavity Flameholder at On- and Off-Design Conditions*. PhD thesis, Department of Mechanical and Aerospace Engineering, University of Virginia.

- Kirik, J. W., C. P. Goyne, J. C. McDaniel, R. D. Rockwell, L. M. L. Cantu, E. C. A. Gallo, and A. D. Cutler  
2017. Aerodynamic characterization of a cavity flameholder in a premixed dual-mode scramjet. *Journal of Propulsion and Power*, 34(3):739–749.
- Kirik, J. W., C. P. Goyne, J. C. McDaniel, R. D. Rockwell, R. F. Johnson, and H. K. Chelliah  
2015. Velocimetry using graphite tracer particles in a scramjet flowpath (invited). AIAA 2015-0355.
- Kirik, J. W., C. P. Goyne, S. J. Peltier, C. D. Carter, and M. A. Hagenmaier  
2014. Velocimetry measurements of a scramjet cavity flameholder with inlet distortion. *Journal of Propulsion and Power*, 30(6):1568–1576.
- Krauss, R. and J. McDaniel  
1992. A clean air continuous flow propulsion facility. In *28th Joint Propulsion Conference and Exhibit*. AIAA 1992-3912.
- Laurence, S., D. Lieber, J. M. Schramm, K. Hannemann, and J. Larsson  
2015. Incipient thermal choking and stable shock-train formation in the heat-release region of a scramjet combustor. part i: Shock-tunnel experiments. *Combustion and Flame*, 162(4):921–931.
- Le Pichon, T. and A. Laverdant  
2016. Numerical simulation of reactive flows in ramjet type combustor and associated validation experiments. *AerospaceLab Journal*.
- Lieber, D. A., C. P. Goyne, R. D. Rockwell, C. M. Geipel, and H. K. Chelliah  
2018a. Design and testing of an additively manufactured flame-holder for scramjets flows. In *AIAA Propulsion and Energy Forum*. American Institute of Aeronautics and Astronautics.
- Lieber, D. A., C. P. Goyne, R. D. Rockwell, C. M. Geipel, and H. K. Chelliah  
2018b. Design and testing of an additively manufactured flameholder for scramjet flows.
- Lin, K.-C., K. Jackson, R. Behdadnia, T. A. Jackson, F. Ma, and V. Yang  
2010. Acoustic characterization of an ethylene-fueled scramjet combustor with a cavity flameholder. *Journal of Propulsion and Power*, 26(6):1161–1170.
- Liu, K., D. Stelzer, A. Williamson, D. Liu, and A. L. Jennings  
2016. Topology optimization and CFD analysis of a hypersonic vehicle nose cone. AIAA 2016-1247.
- Liu, K., D. J. Stelzer, D. Liu, C. Hartsfield, and A. J. Williamson  
2017. Continued improvements on the internal convective cooling system of a notional hypersonic vehicle. Number AIAA 2017-1144. AIAA 2017-1144.
- Loth, E.  
2008. Drag of non-spherical solid particles of regular and irregular shape. *Powder Technology*, 182(3):342–353.
- Madara, S. R. and C. P. Selvan  
2017. Review of recent developments in 3-d printing of turbine blades. *European Journal of Advances in Engineering and Technology*, 4(7):497–509.

- Masullo, A. and R. Theunissen  
2017. Automated mask generation for PIV image analysis based on pixel intensity statistics. *Experiments in Fluids*, 58(6).
- Masullo, A. and R. Theunissen  
2018. On dealing with multiple correlation peaks in PIV. *Experiments in Fluids*, 59(5):89.
- Matsuo, K., Y. Miyazato, and H.-D. Kim  
1999. Shock train and pseudo-shock phenomena in internal gas flows. *Progress in Aerospace Sciences*, 35(1):33–100.
- McDaniel, J. C., C. P. Goyne, E. B. Bryner, D. B. Le, C. T. Smith, and R. H. Krauss  
June 2005. Dual-mode scramjet operation at a mach 5 flight enthalpy in a clean air test facility. Number 1. American Institute of Physics 762, 1277.
- Melling, A.  
1997. Tracer particles and seeding for particle image velocimetry. *Measurement Science and Technology*, 8(12):1406.
- Meyers, J. F.  
1995. Development of doppler global velocimetry as a flow diagnostics tool. *Measurement Science and Technology*, 6(6):769–783.
- Naka, Y., K. Tomita, M. Shimura, N. Fukushima, M. Tanahashi, and T. Miyauchi  
2016. Quad-plane stereoscopic PIV for fine-scale structure measurements in turbulence. *Experiments in Fluids*, 57(5):1–20.
- Nielsen, T.  
2019. Hybrid les/rans simulation of a premixed ethylene-fueled dual-mode scramjet combustor: Small cavity configuration. AIAA.
- Nielsen, T., J. R. Edwards, H. K. Chelliah, D. Lieber, C. P. Goyne, R. D. Rockwell, and A. D. Cutler  
2018. Hybrid les/rans simulation of supersonic premixed ethylene combustion. In *AIAA SciTech Forum*. American Institute of Aeronautics and Astronautics.
- Nobach, H. and E. Bodenschatz  
2009. Limitations of accuracy in PIV due to individual variations of particle image intensities. *Experiments in Fluids*, 47(1):27–38.
- Peltier, S. and C. D. Carter  
2015. Response of a mach 3 cavity flameholder to a shock-induced distortion. In *53rd AIAA Aerospace Sciences Meeting*. American Institute of Aeronautics and Astronautics.
- Petrie, H., . SAMIMY, and A. Addy  
1986. Compressible separated flows. *AIAA journal*, 24(12):1971–1978.
- Poinsot, T., D. Veynante, and S. Candel  
1991. Quenching processes and premixed turbulent combustion diagrams. *Journal of Fluid Mechanics*, 228:561–606.

- Raffel, M., C. Willert, S. Wereley, and J. Kompenhans  
2007. *Particle Image Velocimetry: A Practical Guide*, Experimental Fluid Mechanics. Springer Berlin Heidelberg.
- Ramesh, K. K., J. R. Edwards, C. P. Goyne, and J. C. McDaniel  
2018. Large eddy simulation of high-speed, premixed ethylene combustion. AIAA SciTech Forum. AIAA 2015-0356.
- Rauch, A. H., A. Konduri, J. Chen, H. Kolla, and H. K. Chelliah  
January 2018. Dns investigation of cavity stabilized premixed turbulent ethylene-air flame. AIAA 2018-1674.
- Rêgo, I., T. Marcos, D. R. Pinto, R. Vilela, V. Galvão, A. Pivetta, G. Camilo, J. Silva, B. Lima, A. Carvalhal, R. Cardoso, J. Martos, A. Santos, A. Oliveira, and P. Toro  
2016. Ground experimentation with 3D printed scramjet inlet models at hypervelocities. *Aerospace Science and Technology*, 55:307–313.
- Rice, B.  
2014. *Characterization of a Dual-Mode Scramjet Via Stereoscopic Particle Image Velocimetry*. PhD thesis, University of Virginia, Department of Mechanical and Aerospace Engineering, PHD, 2014, Charlottesville, VA.
- Rice, B. E., C. P. Goyne, and J. C. McDaniel  
2015. Seeding bias in particle image velocimetry applied to dual-mode scramjet. *Journal of Propulsion and Power*, 31(5):1393–1403.
- Rocketdyne, A.  
2017. Aerojet rocketdyne achieves 3-d printing milestone with successful testing of full-scale r110 copper thrust chamber assembly. [retrieved on September 6, 2018].
- Rockwell, R. D., C. P. Goyne, H. Chelliah, J. C. McDaniel, B. E. Rice, J. R. Edwards, L. M. L. Cantu, E. C. A. Gallo, A. D. Cutler, and P. M. Danehy  
2017. Development of a premixed combustion capability for dual-mode scramjet experiments. *Journal of Propulsion and Power*, 34(2):438–448.
- Rockwell, R. D., C. P. Goyne, B. E. Rice, T. Kouchi, J. C. McDaniel, and J. R. Edwards  
2014. Collaborative experimental and computational study of a dual-mode scramjet combustor. *Journal of Propulsion and Power*, 30(3):530–538.
- Samimy, M. and S. K. Lele  
1991. Motion of particles with inertia in a compressible free shear layer. *Physics of Fluids A*, 3(8):1915–1923.
- Saunders, M.  
2015. Additive impact part 1 - how am could disrupt your market. LinkedIn. [retrieved 4 January 2018].
- Scarano, F.  
2002. Iterative image deformation methods in PIV. *Measurement Science and Technology*, 13(1):R1.

- Scarano, F.  
2013. Tomographic PIV: principles and practice. *Measurement Science and Technology*, 24(1):012001.
- Scarano, F. and B. W. Oudheusden  
2003. Planar velocity measurements of a two-dimensional compressible wake. *Experiments in Fluids*, 34(3):430–441.
- Schanz, D., S. Gesemann, and A. Schröder  
2016. Shake-the-box: Lagrangian particle tracking at high particle image densities. *Experiments in Fluids*, 57(5):1–27.
- Scheel, F.  
2004. PIV measurement of a 3-dimensional reacting flow in a scramjet combustion chamber. In *42nd AIAA Aerospace Sciences Meeting and Exhibit*. American Institute of Aeronautics and Astronautics.
- Schlichting, H. and K. Gersten  
2017. *Boundary-Layer Theory*. Springer Berlin Heidelberg.
- Schlüßler, R., J. Czarske, and A. Fischer  
2014. Uncertainty of flow velocity measurements due to refractive index fluctuations. *Optics and Lasers in Engineering*, 54:93–104.
- Schmidt, B. E. and J. A. Sutton  
2018. High-resolution velocimetry from tracer particle fields using wavelet-based optical flow. In *2018 AIAA Aerospace Sciences Meeting*. American Institute of Aeronautics and Astronautics.
- Sciacchitano, A., D. R. Neal, B. L. Smith, S. O. Warner, P. P. Vlachos, B. Wieneke, and F. Scarano  
2015. Collaborative framework for PIV uncertainty quantification: comparative assessment of methods. *Measurement Science and Technology*, 26(7):074004.
- Sciacchitano, A. and B. Wieneke  
2016. PIV uncertainty propagation. *Measurement Science and Technology*, 27(8):084006.
- Siebert, M.  
2017. Breakthrough with 3D printed gas turbine blades. [retrieved 2 July 2018].
- Smith, C. T.  
2011. Application of stereoscopic particle image velocimetry to a dual-mode scramjet. *Journal of Propulsion and Power*, 27(6):1178–1185.
- Stella, A., G. Guj, J. Kompenhans, M. Raffel, and H. Richard  
2001. Application of particle image velocimetry to combusting flows: design considerations and uncertainty assessment. *Experiments in Fluids*, 30(2):167–180.
- Sutton, J. A.  
2013. Highly turbulent combustion: Scientific challenges, measurement requirements, and diagnostic needs. In *AFOSR-ARO Basic Combustion Review*, Dayton, OH.

- Tanahashi, M., S.-J. Kang, T. Miyamoto, S. Shiokawa, and T. Miyauchi  
2004. Scaling law of fine scale eddies in turbulent channel flows up to  $re=800$ . *International Journal of Heat and Fluid Flow*, 25(3):331 – 340.
- Tanahashi, M., K. Matsuoka, and T. Miyauchi  
1997. Coherent fine scale structure in temporally developing turbulent mixing layers. *Turbulence, Heat and Mass Transfer 2*.
- Tanahashi, M., S. Murakami, G.-M. Choi, Y. Fukuchi, and T. Miyauchi  
2005. Simultaneous CH-OH PLIF and stereoscopic PIV measurements of turbulent premixed flames. *Proceedings of the Combustion Institute*, 30(1):1665 – 1672.
- Theunissen, R., F. Schrijer, F. Scarano, and M. Riethmuller  
2006. Application of adaptive PIV interrogation in a hypersonic flow. In *Proceedings of the 13th international symposium on applications of laser techniques to fluid mechanics*, Pp. 26–29.
- Tropea, C., A. Yarin, and J. Foss  
2007. *Springer Handbook of Experimental Fluid Mechanics*, volume 1 of *Springer Handbook of Experimental Fluid Mechanics*. Springer.
- Tuttle, S. G., C. D. Carter, and K.-Y. Hsu  
2014. Particle image velocimetry in a nonreacting and reacting high-speed cavity. *Journal of Propulsion and Power*, 30(3):576–591.
- Urban, W. D. and M. G. Mungal  
2001. Planar velocity measurements in compressible mixing layers. *Journal of Fluid Mechanics*, 431:189–222.
- Wagner, J., K. Yuceil, and N. Clemens  
2010. Velocimetry measurements of unstart in an inlet-isolator model in mach 5 flow. *AIAA journal*, 48(9):1875–1888.
- Wang, Z., H. Wang, and M. Sun  
2014. Review of cavity-stabilized combustion for scramjet applications. *Proceedings of the Institution of Mechanical Engineers, Part G: Journal of Aerospace Engineering*, 228(14):2718–2735.
- Weinkauff, J., D. Michaelis, A. Dreizler, and B. Böhm  
2013. Tomographic PIV measurements in a turbulent lifted jet flame. *Experiments in Fluids*, 54(12):1–5.
- Weisgerber, H., R. Martinuzzi, U. Brummund, and P. Magre  
2001. PIV measurements in a mach 2 hydrogen-air supersonic combustion. In *10th AIAA/NAL-NASDA-ISAS International Space Planes and Hypersonic Systems and Technologies Conference*. American Institute of Aeronautics and Astronautics.
- Westerweel, J.  
1997. Fundamentals of digital particle image velocimetry. *Measurement Science and Technology*, 8(12):1379.
- Westerweel, J.  
2000. Theoretical analysis of the measurement precision in particle image velocimetry. *Experiments in Fluids*, 29(7):S003–S012.

- Westerweel, J., G. E. Elsinga, and R. J. Adrian  
2013. Particle image velocimetry for complex and turbulent flows. *Annual Review of Fluid Mechanics*, 45(1):409–436.
- Wieneke, B.  
2015. PIV uncertainty quantification from correlation statistics. *Measurement Science and Technology*, 26(7):074002.
- Williams, O. J. and A. J. Smits  
2012. Application of PIV to the measurement of hypersonic turbulence. In *16th International symposium of laser techniques to fluid mechanics*, Pp. 9–12.
- Xavier, P., A. Vandael, G. Godard, B. Renou, F. Grisch, G. Cabot, M. A. Boukhalfa, and M. Cazalens  
2016. Investigation of combustion dynamics in a cavity-based combustor with high-speed laser diagnostics. *Experiments in Fluids*, 57(4).